

REPORT DOCUMENTATION PAGE			Form Approved OMB No. 0704-0188	
Public reporting burden for this collection of information is estimated to average 1 hour per response, including the time for reviewing instructions, searching existing data sources, gathering and maintaining the data needed, and completing and reviewing the collection of information. Send comments regarding this burden estimate or any other aspect of this collection of information, including suggestions for reducing this burden, to Washington Headquarters Services, Directorate for Information Operations and Reports, 1215 Jefferson Davis Highway, Suite 1204, Arlington, VA 22202-4302, and to the Office of Management and Budget, Paperwork Reduction Project (0704-0188) Washington, DC 20503.				
1. AGENCY USE ONLY (Leave Blank)		2. REPORT DATE 1994	3. REPORT TYPE AND DATES COVERED Final	
4. TITLE AND SUBTITLE Microstructure and Modeling of Edge Dislocations and Grain Boundaries in Polydiacetylenes			5. FUNDING NUMBERS  AFRL-SR-BL-TR-98- 0013	
6. AUTHORS Patricia Michelle Wilson				
7. PERFORMING ORGANIZATION NAME(S) AND ADDRESS(ES) The University of Michigan				
9. SPONSORING/MONITORING AGENCY NAME(S) AND ADDRESS(ES) AFOSR/NI 110 Duncan Avenue, Room B-115 Bolling Air Force Base, DC 20332-8080			10. SPONSORING/MONITORING AGENCY REPORT NUMBER	
11. SUPPLEMENTARY NOTES				
12a. DISTRIBUTION AVAILABILITY STATEMENT Approved for Public Release			12b. DISTRIBUTION CODE	
13. ABSTRACT (Maximum 200 words) See attached.				
DTIC QUALITY INSPECTED 2				
14. SUBJECT TERMS			15. NUMBER OF PAGES	
			16. PRICE CODE	
17. SECURITY CLASSIFICATION OF REPORT Unclassified		18. SECURITY CLASSIFICATION OF THIS PAGE Unclassified	19. SECURITY CLASSIFICATION OF ABSTRACT Unclassified	20. LIMITATION OF ABSTRACT UL

19980116 092

**MICROSTRUCTURE AND MODELING OF EDGE DISLOCATIONS AND  
GRAIN BOUNDARIES IN POLYDIACETYLENES**

**by**

**Patricia Michelle Wilson**

A dissertation submitted in partial fulfillment  
of the requirements for the degree of  
Doctor of Philosophy  
(Materials Science and Engineering)  
in The University of Michigan  
1994

Doctoral Committee:

Assistant Professor David C. Martin, Chair  
Professor Ronald Gibala  
Professor Samuel Krimm  
Assistant Professor Nair Rodríguez-Hornedo

© Patricia Michelle Wilson 1994  
All Rights Reserved

For all those who try to take the less traveled path in life.  
It makes all the difference!



## ACKNOWLEDGMENTS

First of all I would like to thank my advisor for his guidance both academically and philosophically. It would have been impossible for me to finish this without his boundless enthusiasm for our work, thought provoking questions, and seemingly unending patience. I would also like to thank him for constantly trying to push me to the limit of my abilities, although at the time I might not have appreciated it so much. But I will be proud of my achievements since he made it challenging.

My parents have been solidly behind me since the first day I went to school, encouraging me and guiding me. They taught me the value of an education but most importantly, that family and faith come first in life. The most valuable lessons I have ever learned.

I would like to thank my husband for patiently waiting for me to finish my education here in Ann Arbor although it kept us apart for so many years. It was difficult, but his love and encouragement was always there when I needed it.

Here, I learned the true meaning of friendship from Ed and Cyndi Hernandez over the last four years (and our four at MIT). They were there for the good times and the bad, the laughter and tears, and the life changes we went through together. Their friendship has been one of giving without expecting in return and I consider them as a part of my family now.

Finally, I would like to thank the Martin Research Group and my committee for their help, suggestions, and their challenging questions. The

rarefied atmosphere in the lab often led to exciting times, but I wouldn't have chosen anywhere else

The US Air Force Materials Laboratory and NASA each provided me with fellowships to that allowed me to pursue my degree. Had they not been there for me, I might not have started graduate school at all.

This work was sponsored by NSF grant DMR 9024876 and the Michigan Memorial Phoenix project.

## TABLE OF CONTENTS

DEDICATION.....	ii
ACKNOWLEDGMENTS.....	iii
TABLE OF CONTENTS.....	v
LIST OF FIGURES.....	viii
LIST OF TABLES.....	xvii

## CHAPTER

I. INTRODUCTION AND OVERVIEW.....	1
Introduction.....	1
Solid State Polymerization .....	3
Morphology.....	8
Defects.....	8
Goals and Overview of Dissertation.....	10
Formation of Defects.....	10
Structure of Defects.....	11
Grain Boundaries.....	12
HREM Theory.....	13
II. DROPLETS ON SURFACES.....	14
Introduction.....	14
Experimental.....	17
DCHD monomer synthesis.....	17
Sample Preparation.....	18
TEM Operation.....	18
Results and Discussion.....	20
Conclusions.....	38

<b>III. EFFECT OF THREE DIMENSIONAL FREE BOUNDARY CONDITIONS ON THE CRYSTALLIZATION OF DIACETYLENES.....</b>	<b>40</b>
Introduction.....	40
Experimental.....	44
Results.....	45
Discussion.....	54
Conclusions.....	72
<b>IV. DIRECT IMAGING OF RELAXATIONS NEAR DISLOCATIONS IN POLYDIACETYLENE.....</b>	<b>73</b>
Introduction.....	73
Experimental.....	77
Analysis of Dislocation Images.....	77
Modulus Calculations.....	78
Theories of Distortions Around Dislocations .....	79
Isotropic Linear Elastic Dislocation Theory.....	79
Anisotropic Linear Elastic Dislocation Theory.....	85
Liquid Crystal Dislocation Theory.....	85
Results and Discussion.....	89
Conclusion .....	104
<b>APPENDIX 4.1.....</b>	<b>106</b>
Procedure to calculate the strain field for a chain end dislocation in an anisotropic media .....	106
<b>V. PREDICTION OF GRAIN BOUNDARY STRUCTURE AND PROPERTIES USING O-LATTICE THEORY.....</b>	<b>111</b>
Introduction.....	111
O-lattice Theory.....	119
Prediction of Grain Boundary Properties .....	123
Results and Discussion.....	129
Conclusions.....	134
<b>VI. HIGH RESOLUTION ELECTRON MICROSCOPY AS A FUNCTION OF THICKNESS ON WEDGE SHAPED POLYMER SAMPLES.....</b>	<b>136</b>
Introduction.....	136
Experimental.....	145
Sample Preparation.....	145
TEM Operation and Calibration .....	145
SPM Operation.....	147
Digital Image Analysis.....	147

Simulation of HREM Images.....	148
Results and Discussion.....	150
Conclusions.....	169
<b>VII. CONCLUSIONS AND FUTURE WORK.....</b>	<b>175</b>
Chapter II: Droplets on Surfaces .....	175
Chapter III: Spheres .....	176
Chapter IV: Dislocations.....	177
Chapter V: Grain Boundaries.....	178
Chapter VI: HREM of Polymers.....	180
<b>BIBLIOGRAPHY.....</b>	<b>184</b>

## LIST OF FIGURES

### Figure

1.1	Schematic of the general transition from monomer to polymer for diacetylenes. Two mesomeric forms of the polymer chain are possible, a) the enyne form and b) the butatriene form. Baughmann's (1974) geometric parameters $d_1$ , $d_2$ , and $\gamma$ are shown.....	4
1.2	The monomer 1,6-di(N-carboxolyl)-2,4 hexadiyne (DCHD) .....	6
1.3	Projections down the c-axis for the a) monomer (Enkelmann et al., 1977) and b) polymer (Apgar and Yee, 1978) crystal structures of DCHD.....	7
2.1	TEM micrograph of a droplet of poly(DCHD) shadowed with gold from an incident angle of $12^\circ$ . The chain axis is in the plane of the substrate and runs parallel to the observed cracks.....	21
2.2	(a) SAED of poly(DCHD) droplet. The reflections indicated are from different zone axes suggesting a fiber texture. (b) A simulation of the SAED pattern (CERIUS) using a fiber texture geometry for the reported polymer crystal structure (Apgar and Yee, 1978).....	22
2.3	Schematic of droplet showing domains where the a- and b-axes are in differing orientations with respect to the substrate .....	23
2.4	HREM image of the DCHD droplet edge where the chain axis is parallel to the edge. The lattice fringes from the (010) planes can be seen to bend to conform to the droplet surface. Several edge dislocations with a Burger's vector in the [010] direction can be seen .....	26

2.5	Schematic of a bent crystal with edge dislocations of the type $\mathbf{b} = [001]$ to incorporate the bending .....	27
2.6	HREM image of a low-angle tilt subgrain boundary in a DCHD droplet. The lattice fringes being imaged are the (200) planes with a spacing of 0.8 nm and correspond to the spacing between chains. The Burger's vector is $[200]$ with a magnitude of 0.8 nm. Around the dislocations there is a region of crystal where the contrast does not give rise to lattice fringes; these areas measure approximately 6 nm to 36 nm. The distance between the imaged dislocations is approximately 7.0 to 12.0 nm.....	30
2.7	A schematic showing lattice fringes as lines to highlight the position of chain end dislocations in Figure 2.6 .....	31
2.8	Schematic showing the general orientation of the chains with respect to the edge of the droplet. With the incorporation of bent chains, several subgrain boundaries are created near the edge of the droplet. The rectangle shows the region imaged in Figure 2.6 .....	32
2.9	TEM micrograph of a polymerized DCHD droplet that was etched with a chloroform solution. The micrograph was taken in diffraction mode as a defocused (000) spot in order to increase the contrast. Arrows point out lines of possible etch pits that have polygonalized as a result of bending of the lattice at the edges .....	34
2.10	(a) STEM image of etched poly(DCHD) droplet showing regions of low light contrast that correspond to voids (A) or surface holes (B). (b) SEM image of the same are of droplet that shows corresponding holes (B) in the surface versus areas that have no surface holes.....	35
2.11	A schematic showing an edge dislocation in the monomer lattice of type $\mathbf{b} = [001]$ and the resulting transition to polymer with a region of unreacted monomer near the dislocation as a result of misorientation of the monomer units outside of the necessary polymerization parameters.....	37
3.1	Schematic of glass column apparatus used to form spheres for study. The column is 4.5 cm in diameter and 70 cm high with four ports spaced 20 cm from each other. The spheres in this study were produced by atomizing solution at heights of 65 or 45 cm and allowing them to evaporate and	

	settle under normal atmospheric conditions onto a collection media.....	46
3.2	Size distribution of spheres collected for 49 hours after atomization at a height of 65 cm under normal atmospheric conditions.....	47
3.3	A composite of fifteen spheres imaged with TEM from a grid. The calibration bar is 0.2 $\mu\text{m}$ . Many of the spheres show both smooth and irregular outlines and areas of light contrast. The regions of light contrast indicate less dense regions.....	48
3.4	TEM image of a single sphere highlighting the region of light contrast believed to be a hole in the sphere. In general the perimeter of the sphere is smooth and sharp with few cracks emanating from it.....	49
3.5	(a) SEM image of a large sphere showing two holes in the surface parallel to the beam. (b) STEM image of the same sphere with light regions of contrast that correspond the holes in (b).....	50
3.6	(a) SEM and STEM pair for a sphere with two holes, looking down the hole axis. (b) SEM and STEM pair of the same sphere tilted 11° confirming the existence of the holes.....	51
3.7	Tilt series of a one micron sphere. (a) SEM and STEM images of the sphere on the substrate. Two regions of light contrast are seen in the STEM image, which are believed to be holes. (b) SEM and STEM pair of the same sphere tilted 47° in the x-direction and 30° in the y-direction to bring a hole into view. The SEM image shows rough edges tilted into view and the corresponding STEM image shows a greater area of light contrast. (c) SEM and STEM pair tilted in the opposite direction by a 30° tilt along the y-axis from the original orientation. A second crack or hole is brought into view as noted by the rough area in the SEM image and light contrast in the STEM image.....	52
3.8	TEM image of a sphere with the shell thickness apparent. The shell is approximately 70 nm in width.....	55
3.9	TEM image of a sphere oriented so the axis of the two holes is in the plane of the substrate. The perimeter of both holes appears rough whereas the sides of the sphere are smooth and sharp .....	56



3.10	A representative TEM image of sphere oriented with the hole axis in the plane of the substrate and its corresponding SAED. The SAED shows sets of arcs with an absence of spots corresponding to the hole axis. The arcs correspond to spacings which are 0.83, 0.62, and $0.41 \pm 0.02$ nm. Similar TEM images also have shown HREM fringes along the side edges corresponding to both 0.8 nm and 1.2 nm fringes. This observation along with the SAED patterns suggest that the spheres are textured with a general orientation of the polymer chain parallel to the hole axis.....	57
3.11	TEM image of a sphere with the hole axis in the plane. The hole perimeter is rough in contrast to the sides of the sphere which are sharp. Insets are magnified images of the boxed regions showing 1.2 nm fringes corresponding to the (010) planes. The region between the boxes shows these fringes bending with the same radius of curvature as the surface.....	59
3.12	Schematic of proposed sphere formation which produces the observed holes and texturing. The solution which is atomized is at the solubility limit of DCHD in chloroform (0.434 wt% at room temperature). As the chloroform begins to evaporate at the surface, swollen DCHD precipitates and nucleates in the region at the surface which is depleted of solvent. Continued evaporation and growth forms a shell with possible holes .....	62
3.13	Phase diagram for the DCHD-Chloroform system. Solubility data of DCHD in solution was experimentally determined (Liao et al., 1994) and used to calculate the amount of chloroform able to swell DCHD from Flory-Huggins theory (Flory, 1953) .....	63
3.14	a) Characteristics of spheres undergoing drying at gas temperatures above the boiling point. b) the same scheme except at gas temperatures below the boiling point. Both Figures taken from Masters (1991) .....	66
3.15	Some possible crystallographic texturing options for the spheres. Options are shown in projection parallel and perpendicular to the hole axis.....	67
3.16	Schematic showing proposed idealized structure and texturing of spheres formed via the mechanism and processes outlined in the text based on the experimental data.....	70

4.1	Shear of a unit cell in the xy plane results in a tilt distortion equal to the shear.....	83
4.2	(a) is the shear strain around a isotropic edge dislocation where the extra half plane is oriented along the positive y axis. If the tilt is plotted by making a trace around the dislocation core as shown, (b) is produced. The large lobes with maximums at 0° and 180° are produced by the tilt of the layers incorporating the extra planes. The smaller lobes are the effect of shear in the x direction between individual repeat units along the y direction.....	84
4.3	Orientations of the two types of chain end edge dislocations in poly(DCHD). The a, b, c, axis refer to the unit cell axis system, where as the $x_1, x_2, x_3$ are the orthogonal dislocation coordinate system required for strain field calculations using anisotropic dislocation theory (Steeds, 1973). The diad axis of the space group ( $P2_1/c$ ) is along the c-axis and perpendicular to the dislocation lines. (a) shows the orientation for the experimental three chain end edge dislocation analyzed in the text .....	86
4.4	Transverse edge dislocation in a columnar liquid crystal. A Burger's circuit is shown which results in a strength of +1.....	88
4.5	a) is the shear strain around a columnar liquid crystal edge dislocation where the extra half plane is oriented along the positive y axis. If the tilt is plotted by making a trace around the dislocation core as shown, (b) is produced. The large lobes with maximums at 0° and 180° are produced by the tilt of the layers incorporating the extra planes. Notice the lack of small lobes as seen in the isotropic elasticity case. Because there are no correlations along the column in a liquid crystal the effect of shear is suppressed. The discontinuities at $\pm \pi/2$ are due to the mathematical expression since the vector $M_x$ will go to infinity.....	90
4.6	A HREM image of a poly(DCHD) three chain end edge dislocation with Burger's vector $3a/2[100]$ . The lattice fringes correspond to the chain axis .....	91
4.7	A map of the molecular director to the chains in Figure 4.6. The bending of the normal is indicative of the splay character of the deformation of the polymer chains.....	92
4.8	The experimental tilt measured from HREM images of a three chain end edge dislocation. The tilt was measured	

- with an error of  $\pm 0.5^\circ$ . (a) shows the data overlapped with the solution from liquid crystal columnar theory. A value of  $\lambda=0.8 \pm 0.1$  nm was used to fit the data. (b) The experimental data matched by the best fit from the anisotropic linear elastic solution. A polymer anisotropy parameter of  $W=3.5$  was needed to fit the data .....93
- 4.9 Behavior of the tilt around a three chain end edge dislocation as predicted by (a-e) anisotropic linear elasticity for values of  $W=0.35-3.5$ . (f) shows the corresponding solution provided by columnar liquid crystal theory with  $\lambda=0.8$  nm. As the polymer anisotropy parameter,  $W$ , increases the magnitude of the tilt at  $0^\circ$  and  $180^\circ$  decreases. The width of the major tilt distortion increases also. The small lobes are suppressed as the anisotropy is more pronounced until they take a value close to zero and approach the liquid crystal solution .....97.
- 4.10 Plots of the local tilt for the three solutions: (a) the monomer elastic solution ( $W=0.35$ ), (b) the polymer elastic solution ( $W=3.5$ ), and (c) the columnar liquid crystal solution ( $\lambda=0.8$ nm). The monomer solution behaves non-linearly inside a core radius drawn of  $5b$ . The polymer elastic solution is uniform close to the origin of the dislocation. Dashed lines define the parabola inside of which the tilt is non-zero. The polymer and columnar solutions both closely resemble the HREM image of a dislocation in Figure 4.6 .....99
- 5.1 Definition of grain boundaries where the interface disrupts the chain axis. A twist boundary of this type may be called an axial chain invariant (ACI) boundary and a tilt boundary as an axial chain rotation (ACR) after Martin and Thomas (1991).....113
- 5.2 A schematic showing equivalent classes in four unit cells. Each numbered point in a unit cell is equivalent to the same numbered point in another unit cell (Adapted from Bollman, 1970).....121
- 5.3 (a) Projection of the DCHD monomer down the c-axis which will eventually become the chain axis after polymerization. (b) The c-axis projection of a  $3^\circ$  twist misorientation between two crystals showing overlap of few molecules. (c) A  $10^\circ$  twist misorientation projection which increases the number of overlap sites. These sites of

	overlap are called O-lattice points. These points are the nucleation for relaxation at the interface .....	125
5.4	(a) C-axis projection of a 5° twist misorientation between two monomer DCHD crystals. Relaxation of the interface begins at the O-lattice sites. (b) The relaxed boundary in (a). The interface relaxes into regions of perfect overlap and a network of screw dislocations.....	126
5.5	Two relaxed twist grain boundaries illustrating that the density of screw dislocations increases as the angle of misorientation of the crystals increases.....	127
5.6	A schematic defining the parameters used in deriving the fraction of area relaxed. The vectors $u_1$ and $u_2$ define the O-lattice. Shaded areas are regions that have relaxed, and in between them are screw dislocations, $S$ , of width $b_1$ and $b_2$ .....	128
5.7	Mechanical strength data for polymer twist bicrystals (Liao, 1994) fitted using $n=1.0$ .....	130
5.8	Data from the bicrystal experiments by Dimos, et al. (1990) showing the decrease of the critical current for onset of superconductivity through a grain boundary (normalized to the bulk crystal) as a function of grain boundary misorientation. Overlapped is the prediction by an extension of O-lattice theory to describe the expected behavior. The results are bracketed by curves predicting that the width of disorder that influences this property at the screw dislocation is 0.5 to one Burger's vector.....	131
5.9	Experimental photocurrent as a function of grain boundary misorientation for DCHD polymer bicrystals (Liao, 1994). The data follows the trend predicted by polymerization retardation on the basis of O-lattice theory. The width of the lines of unpolymerized screw dislocations is fitted to be half the Burger's vector.....	133
6.1	Schematic of the general processes in an electron microscope to form a high resolution image. $F$ and $F^{-1}$ are the Fourier transform and inverse Fourier transform operations.....	138
6.2	The multislice process .....	142
6.3	Pendellosüing plots for 100-800 kV for the (000) and (010) beams. The Pendellosüing effect is maximum at 400 kV.....	151

6.4	Pendellosing plot for 400 kV. Several distinct thicknesses are noted where images independent of microscope parameters are located .....	152
6.5	Projected potential of poly(DCHD) looking down the [100] zone axis. Light regions are areas of high electron potential (the atoms) denoted by B, while A represents an area of no electron potential. When the intensity is equal at both A and B, half spacing fringes (0.6 nm) appear.....	154
6.6	Schematic of the scattered electron beams as a function of thickness. When the transmitted beam and two diffracted beams are present, 1.2 nm fringes are produced. If the transmitted beam is not present, the interaction of the two diffracted beams produce half spacing fringes.....	156
6.7	Contrast in the multislice simulated images as a function of thickness for Gaussian focus. Unique thickness images are indicated.....	159
6.8	HREM image of a poly(DCHD) droplet edge where the 1.2 nm fringes correspond to the (010) chain axis. The thickness of the droplet increases from top to bottom. An extinction of the fringes and 0.6 nm periodicity is seen in the micrograph. Between these images the contrast of the fringes reverses.....	161
6.9	A plot of the amplitude of the periodicities in the HREM image as determined by FFT as a function of distance along the wedge. Unique images are indicated .....	163
6.10	A schematic comparing the appearance of the experimental image, the multislice prediction, and the case for a sinusoidal variation of Pendellosing images for small unit cell materials.....	166
6.11	Height profiles for DCHD droplets examined with SPM.....	167
6.12	A representative SPM image of a poly(DCHD) droplet on a amorphous carbon coated mica substrate imaged using tapping mode.....	168
6.13	A diagram illustrating the geometry used to derive the relation between the radius of the sphere, the diameter of the droplet, and the angle of contact.....	170

6.14	Height profile data measured by SPM for ten droplets. The depth was normalized by the radius of the reference sphere for each droplet.....	171
6.15	The average normalized height profile used to determine the profile of the droplets imaged by HREM .....	172
6.16	A plot of the SPM predicted droplet profiles overlaid by the prediction from dynamical theory .....	173
7.1	Schematic diagram of a polymer bicrystal to create ACR boundaries. It is possible to create an array of [010] edge dislocations at the interface by tilting about the [100] direction. Likewise, tilting about [010] generates [100] edge dislocations. The spacing between the dislocations decreases as the angle between the grains increase .....	182

## LIST OF TABLES

### Table

3.1	Spacings from SAED of spheres including their orientation and what possible planes the data may correspond to along with proposed crystallographic texturing.....	60
3.2	Experimental and calculated volume fractions from Flory-Huggins theory (Flory, 1953).....	65
4.1	Elastic modulus determination by molecular mechanics simulations .....	81
4.2	Elastic modulus of diacetylenes.....	96
6.1	Microscope parameters used for multislice calculations .....	149
6.2	Unique thicknesses predicted from Pendellosüing plot.....	157
6.3	Contrast type as a function of thickness from computer simulated images.....	158
6.4	Experimental contrast type as a function of depth into the droplet. Multislice heights are based on Pendellosüing plot and theoretical image contrast calculations.....	164

## CHAPTER I

### INTRODUCTION AND OVERVIEW

#### Introduction

The organization of polymers near defects is a general question of both scientific and technological interest. The relationship between microstructure and properties must involve a discussion of defects. But defects in macromolecular materials are not as clearly defined as in more ordered systems. Schemes to classify defects must rely on the symmetry of the phase, the dimensionality of the defect and the nature of the deformation induced. Several researchers such as Kléman (1983) and Wunderlich (1973) have classified macromolecular defects using these constraints. Defects in polymer systems have not been thoroughly studied because of difficulties in imaging the local regions around defects in organic materials with high energy electron beams. Also, defects are difficult to isolate and study in detail because most polymer systems have a intermediate amount of disorder present in the bulk structure.

In contrast to atomic solids, the properties and structure of polymers are greatly affected by the presence of covalent bonds along the chain. This extra condition complicates the description of structural defects. Advances in molecular chemistry have provided ordered polymers, such as the extended chain conjugated polydiacetylenes, that are better defined in structure and have superior properties. Also recent advances in structural characterization



techniques for organic materials make possible extensive defect structure studies.

The optical and electromagnetic transport properties of polymers should be limited by the structure and density of defects that serve as sinks for photons and charge carriers. Mechanisms of deformation may also be affected by the presence of chain ends or other defects in the crystal, much as they are in metallic and ceramic materials. Upon the understanding of the structure of defects in conjugated polymers, the possibility is opened for an expansion of our control over polymer properties. As an analogy, the control of defects in semiconductor materials has led to a wealth of possibilities in device fabrication. Similarly, polymer materials are being investigated for their strong nonlinear response to modulated light for use in optical devices. If an ability to control defects in polymer crystals is established, then there is the possibility for a similar materials revolution to occur. One possibility might be to use the extra volume around a dislocation for dopants to enhance the nonlinear optical properties or photoconductivity.

Polydiacetylenes are a relatively new class of polymers of general scientific and engineering interest. They first appeared in 1969 in a communication by Wegner (1969) describing the solid state polymerization of crystals of diacetylene. Solid state polymerization is a topochemical process by which crystals of monomer react under the constraints of the lattice to yield nearly perfect polymer crystals. Orientation of chains that allows conjugation to become continuous makes it possible for polymers to be used for electromagnetic and optical applications that were formerly limited to semiconductors and metals.

Since large, extended chain crystals can be formed from diacetylenes they give an unique opportunity to isolate and investigate features of

crystalline polymers. The fiber texturing of crystallites in rigid-rod polymer fibers coupled with regions of less ordered material between crystallites makes morphology-property relationships difficult to determine. Polydiacetylenes have a single crystal structure making them a suitable system to isolate and measure morphology-property relationships that are problematic to study in other extended chain systems.

The extended chain orientation and high thermal stability give polydiacetylenes excellent radiation resistance compared to other macromolecules. This allows them to be investigated using high resolution electron microscopy to obtain atomic scale information to study the chemistry and physics of polyconjugated systems.

### **Solid State Polymerization**

Hirshfeld and Schmidt (1964) introduced the concept of solid state reactions such as photodimerization. They postulated that the course of a solid state reaction could be predicted on the basis of the configuration and nearest-neighbor geometry of the closest monomer molecules in the crystal lattice. Wegner (1969) described a topochemical polymerization reaction in diacetylenes. A topochemical reaction occurs as a diffusionless transformation where the centers of mass of the monomeric units retain their original crystallographic positions and the symmetry of the monomeric units in the monomer and polymer single crystals remains the same.

The polymerization reaction of diacetylenes is a 1,4-trans-addition reaction. This is achieved from the rotation of the monomeric units about their center of mass. The polymerization is thus a stereospecific reaction, giving a stereoregular polymer with a distinct orientation. Figure 1.1 shows schematically the general transition from monomer to polymer. The

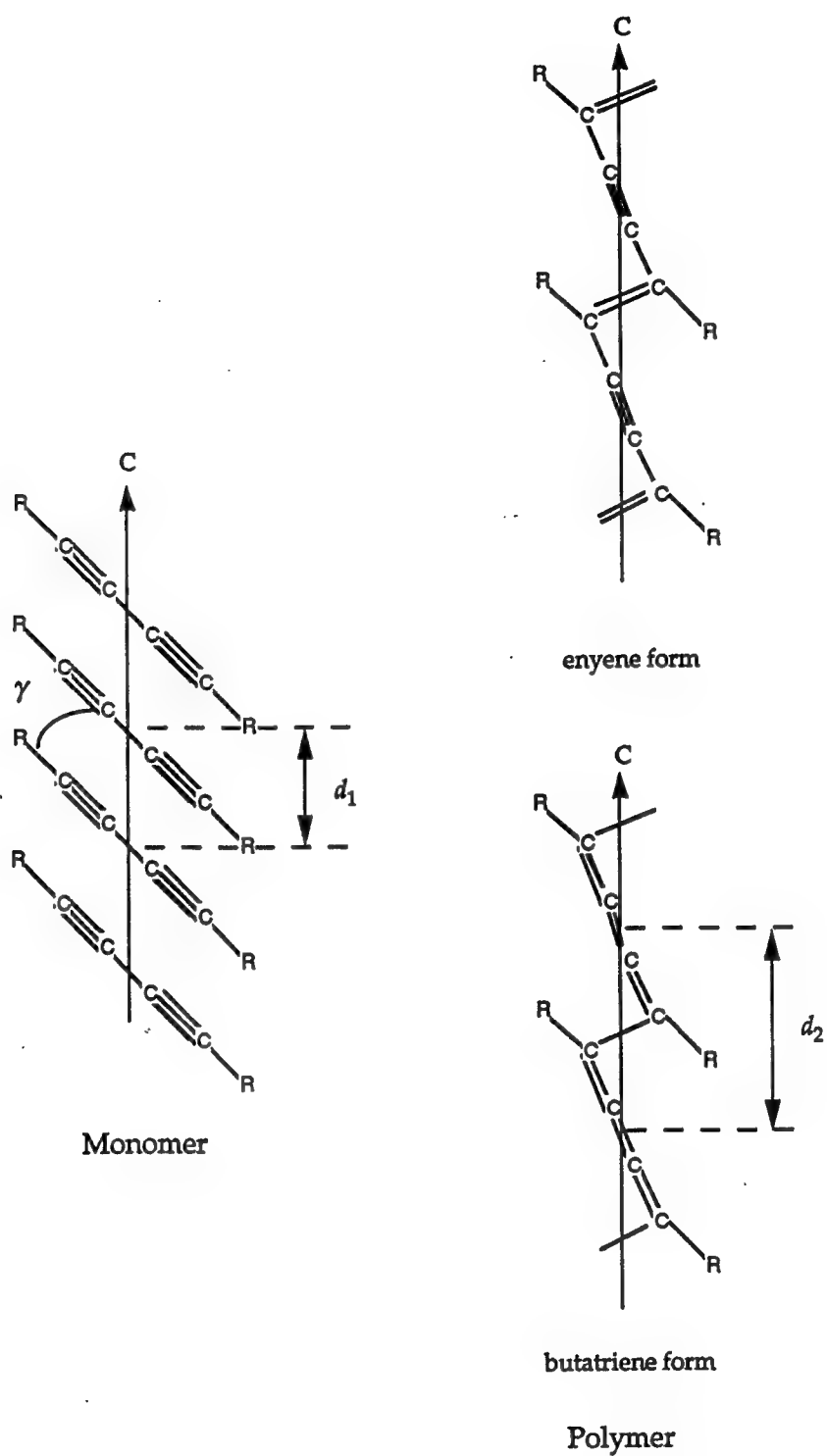


Figure 1.1: Schematic of the general transition from monomer to polymer for diacetylenes. Two mesomeric forms of the polymer chain are possible, a) the enyne form and b) the butatriene form. Baughmann's (1974) geometric parameters  $d_1$ ,  $d_2$ , and  $\gamma$  are shown.

polydiacetylene backbone can exist in two different mesomeric forms, enyene or butatriene, but in general the enyene form predominates (Vinogradov, 1984). This results in an extended, conjugated backbone. The particular diacetylene used in this study was 1,6-di(N-carboxyl)-2,4 hexadiyne (DCHD) (Figure 1.2). The monomer and polymer crystal structure are both monoclinic with space group  $P2_1/c$ . A projection down the  $c$  axis of both structures is shown in Figure 1.3.

The reaction is initiated via several different methods: thermal and gamma radiation, photoinduction, and by electron beam (Liao and Martin, 1993). Thermal polymerization initiates at defects in the monomer crystal and gamma radiation is seen to occur homogeneously. The polymerization of diacetylenes is often an autocatalytic process yielding a S-shaped curve of conversion vs. time (Baughmann, 1978).

Since the polymerization of the monomer is dependent on the positions of the monomer units in its crystal structure, Baughmann (1974) proposed a scheme to predict if new diacetylene molecules would polymerize in the solid state. His study used the principle of least motion of the molecules as the requirement for the units to pack unhindered by steric interactions. The principle of least motion states that the reaction pathway must be one in which the smallest mean square displacement of the atoms would take place. His study concluded that the optimum conditions for reaction were when the packing of the monomer unit allowed for the angle  $\gamma$  between the diacetylene chain with the center of mass was  $45^\circ$  and the relative lattice contraction  $(d_1-d_2)/d_2$  during polymerization should not exceed 0.1. The value of  $d_2$  for all polymerized chains is approximately 0.491 nm, which is dependent on the bond lengths and angles of the polydiacetylene backbone.

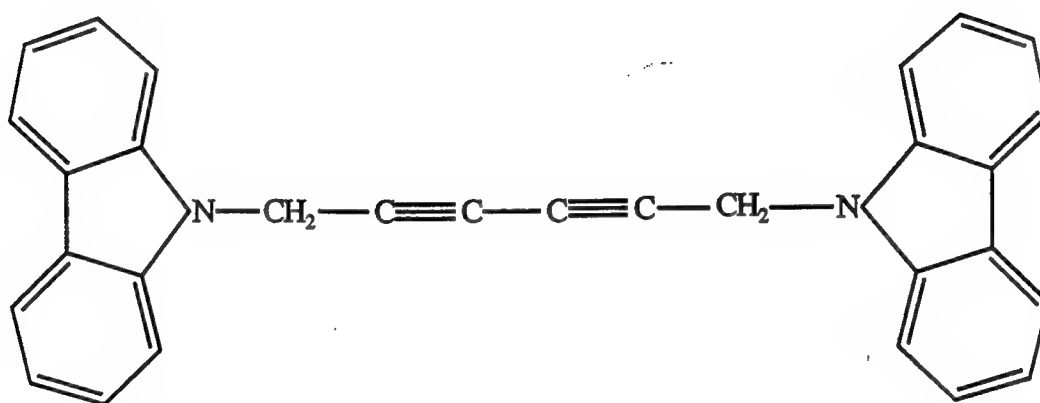
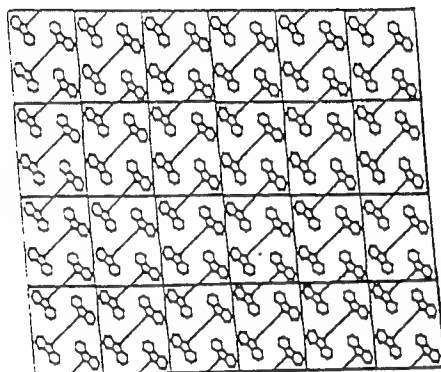
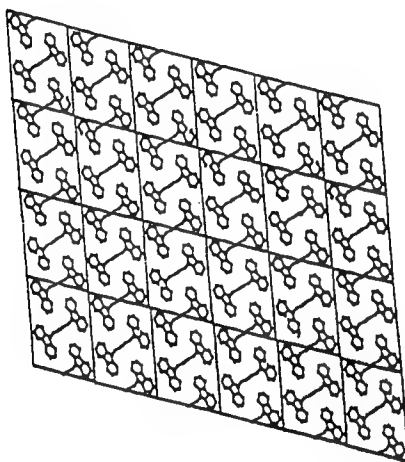


Figure 1.2: The monomer 1,6-di(N-carboxolyl)-2,4 hexadiyne (DCHD)



A



B

Figure 1.3: Projections down the c-axis for the a) monomer (Enkelmann et al., 1977) and b) polymer (Apgar and Yee, 1978) crystal structures of DCHD.

## Morphology

The morphology of polydiacetylenes can be varied through monomer crystallization conditions. Usually the formation of crystals is from the solution growth of monomer and subsequent polymerization using thermal, electron, gamma, or ultraviolet radiation. Since the polymerization is in the solid state, if the monomer crystal is nearly perfect, then the resulting polymer crystals will have an extended chain morphology. Most crystals have a preferred habit and aspect ratio. DCHD prefers to grow with an aspect ratio of length to diameter of 20, forming long needle-like crystals during slow evaporation of the solvent. In order to grow crystals of reasonable length and thickness (1 cm x 2 mm) the solution needs to be confined to a dark, vibration free environment. There is a danger of photo-induced polymerization which turns the normally translucent monomer crystals into opaque crystals with a gold luster.

## Defects

Defects in poly(diacetylenes) have been previously studied in depth by Young's group using transmission electron microscopy. They showed dislocations in poly(toluene sulphonate) (p(TS)) diacetylene crystals using dark field imaging (Young and Petermann, 1982). Later work (Read and Young, 1984) using HREM provided the first direct image of a chain end dislocation in diacetylenes.

Dislocations imaged using dark field were determined to have mainly edge character with a Burger's vector parallel to the chain axis. These dislocations may be energetically unfavorable in the polymer. Dislocation

energies for polyethylene crystals calculated by Shadrake and Guiu (1976) showed that edge dislocations with Burger's vectors of  $[001]$  were an order of magnitude higher than those for screw dislocations with the same Burger's vector. Young and Petermann (1982) explained the presence of polymer edge dislocations in p(TS) with  $\mathbf{b}=[001]$  on the basis that dislocations were formed first in the monomer crystal and were preserved in the structure upon polymerization. An edge dislocation with  $\mathbf{b}=[001]$  in the monomer would be a low energy dislocation because it has a small Burger's vector ( $\sim 0.515$  nm) and the line direction would be short in the thin crystals they were observing. Schermann, et al. (1976) also suggested the presence of dislocations of this type in the monomer from examination of etch pits in p(TS) monomer crystals. Dudley, et al. (1985) later confirmed that the dislocation structure in p(TS) was the same in both monomer and polymer by X-ray topography.

Young postulated that the presence of dislocations may affect the polymerization, acting as a nucleation site, but did not extend his experimental work to examine this effect in any detail. A discussion of the strain fields around the dislocations using an analysis of black-white dislocation images was made. They predicted that the strain fields were more extended than for dislocations of the same type in isotropic materials. The strain fields being extended over 30 monomer units in the chain direction for a edge dislocation with Burger's vector  $[001]$ .

Young and Petermann also discussed grain boundaries observed in p(TS). They imaged arrays of edge dislocations with  $\mathbf{b}=[001]$  that were arranged perpendicular to the chain axis. The spacing between the dislocations suggested low angle tilt grain boundaries of approximately  $5-6^\circ$ .

Recent work by Hankin and Sandman (1991) using Raman spectroscopy on a THD diacetylene has showed evidence for a disordered



phase near the surface. This disordered phase may represent unreacted monomer at the surface.

### **Goals and Overview of Dissertation**

The broad goal of the research described in this dissertation was to provide a fundamental understanding of dislocations and grain boundary defects in conjugated polymers. In particular, we hoped to investigate the formation of defects, the strain fields surrounding the defects, and to provide models to predict the influence of arrays of these defects on macroscopic properties such as mechanical strength and photoconductivity.

### **Formation of Defects**

As the diacetylene monomer is deposited on a substrate or nucleated out of solution, defects such as edge dislocations, screw dislocations, grain boundaries and stacking faults are formed in the monomer crystal which may be preserved in the polymer crystal upon polymerization. The factors which govern their formation depend on how the monomer comes out of solution, the energetics of the defect, and the influence of the surface. In this dissertation we will consider the influence of the surface geometry on the formation of dislocations during crystallization from solution. In order to answer these questions, curved surfaces were created using droplets and spheres formed from solution. This information should prove to be useful for the manufacture of polymer devices which can have complex bending geometries (Prasad and Williams, 1991).

Several issues arise from the use of curved surfaces:

- What is the influence of the surface on the crystallization of the monomer?

- What types of defects are produced?
- How do these defects influence polymerization?

These questions will be addressed in Chapters II and III which deal with the formation of defects in droplets on surfaces and spheres in three dimensional free boundary conditions respectively.

### **Structure of Defects**

The structure of individual defects and arrays of those defects is a complex subject. It involves the topology of the defect, its energy, stress and strain fields, core size, core structure, and in the case of diacetylenes, the influence on the local polymerization. These topics will be explored for a few selected defects which are relevant to general questions of defect-property effects. The possible methods used to elucidate these questions are numerous. The approach taken here will be to use high resolution electron microscopy, molecular mechanics simulations and theoretical modeling to gain insight into these problems.

Edge dislocations created by chain ends will be investigated since their presence in an optoelectronic device could lead to traps for charge carriers. In diacetylenes, a defect present in the monomer structure may be preserved when polymerized. The monomer elasticity is nearly isotropic in most directions due to the van der Waals bonding between molecules. The polymer is highly anisotropic. The addition of covalent bonding in the c direction results in a severely anisotropic system. Because of the differences in elasticity, questions arise:

- How anisotropic are the polymers?
- What are the strain fields around a polymer chain end edge dislocation?

- Can isotropic or anisotropic dislocation theory be used to model the strain fields?
- What is the character of the polymerized dislocation, is it a mixture of a monomer and polymer dislocation? Or are there relaxations which occur during the polymerization process?
- Are there other theories which can be applied that may be more general in scope for ordered polymers?
- What are the energetics of these dislocations?

These questions will be explored in Chapter IV by analyzing HREM images of edge dislocations in polydiacetylenes.

### **Grain Boundaries**

The influence of grain boundaries is a large subject. The aim of our investigation was to use generalities which have been developed for polymer grain boundaries (Martin and Thomas, 1991) and geometrical theories to predict the influence of interfaces on polymer properties. A study of pure grain boundaries will be undertaken. Twist grain boundaries provide the simplest mathematical challenge to extend O-lattice theory (Bollman, 1970) to describe the geometry of the interface for diacetylenes. It is possible to use O-lattice theory to predict the structure of the interface. This theory will be used to compare with bicrystal data from experiments from our laboratory. The following questions are answered in Chapter V using this approach:

- How is O-lattice theory extended to non-cubic systems?
- Can a geometrical theory be successfully used to predict the mechanical strength and photoconductivity of grain boundaries in polymers?

## **HREM Theory**

Investigations into the structure of defects in solids often rely on the use of high resolution electron microscopy (HREM) as a tool to probe the local atomic configuration. Since there is a complex relationship between the sample structure and the resulting image, many studies rely on matching image simulations from defect models to the experimental image. Studies to understand the formation of images brings us closer to quantifying HREM images and gaining more information about defects. In the course of this thesis questions arose about image formation in crystalline polymer wedges and in depth analyses were necessary to understand the experimental data. Chapter VI is a summation of these analysis to understand the imaging process in polymer materials.

This thesis aims to provide answers to some of these questions while also pointing out further research which could help clarify questions which arise in a study of this type. Chapter VII is an overview of the general conclusions of this body of work and sets up a framework of suggestions for future work.

## CHAPTER II

### DROPLETS ON SURFACES

#### Introduction

The organization of polymers near defects is a general question of both scientific and technological interest. Defects in polymer systems have not been thoroughly studied because of the difficulties in imaging organic materials with high energy electron beams. Also, defects are difficult to isolate and study in detail because most polymer systems have small crystallites surrounded by regions of less ordered material. The optical and electromagnetic transport properties of polymers should be limited by the structure and density of defects that serve as sinks for photons and charge carriers. Mechanisms of deformation may also be affected by the presence of chain ends or other defects in the bulk of the crystal.

The reorganization of diacetylene molecules near surfaces and defects in general is explored in this chapter. 1,6-di(N-carbazolyl)-2,4 hexadiyne polydiacetylene (DCHD) was chosen for this experiment because it has been relatively well studied and exhibits electron radiation resistance that allows High Resolution Electron Microscopy (HREM) to be performed (Reed and Young, 1984). The high degree of crystallinity also allows the effect of amorphous regions or small crystallites to be reduced.

Droplet experiments using Transmission Electron Microscopy (TEM) have been shown by Henkee et al. (1988) and Martin et al. (1991) to be useful

in determining the organization of polymers as they approach a constraining surface. Martin et al. (1991) discerned that poly(imide) molecules preferentially oriented in the plane of the substrate and weakly parallel to the edge of the droplet. As the thickness of the droplet increased, the orientation effect decreased. Droplets are useful in that near the edge the sample thickness decreases such that HREM imaging becomes feasible, minimizing artifacts produced by other methods of sample preparation.

Defects in crystalline diacetylenes have been previously studied by Young's group (1979-1986) using TEM. Young and Petermann (1982) showed dislocations in poly(toluene sulfonate) polydiacetylene crystals with a line direction perpendicular to the chain axis using dark-field imaging. They determined that certain dislocations seen were due to grain boundaries. Applying the relation by Hirth and Lothe (1982) that the angle of a tilt grain boundary is related to the number of dislocations needed to incorporate the misfit,  $\theta = b/D$ , they calculated a dislocation density of approximately  $10^{13} \text{ m}^{-2}$  as a maximum observed in their crystals (Young and Petermann, 1982). Later studies of Read and Young (1984) showed that HREM of poly(DCHD) could be performed if imaging conditions were kept below the critical dose ( $J_c$ ) for the reflections of interest [ $J_c$  for equatorial reflections (010) in poly(DCHD) =  $20 \text{ C/cm}^2$ ]. This study provided the first direct imaging of a chain end dislocation in polydiacetylenes (Reed and Young, 1984).

Recent studies of THD (1,1,6,6-tetraphenylhexadienediamine) polydiacetylene by Hankin and Sandman (1991) using Raman spectroscopy were interpreted to be consistent with a disordered phase of an unknown thickness near the surface. These disordered regions could be associated with a failure of the topochemical reaction near the surface in contrast to the bulk.

The ability to produce uniformly textured or single crystal films of polydiacetylenes is important if these materials are to be fully exploited for their nonlinear optical properties. There has been some progress in epitaxial growth of DCHD on organic substrates by LeMoigne et al. (1991). They reported the ability to grow films with a single orientation of the chain axis by vapor deposition of DCHD onto potassium acid phthalate single crystals.

This study was initiated as part of a program of research designed to introduce specific defects into crystalline poly(diacetylenes) in order to study the relationship between microscopic defect structure and macroscopic materials properties in detail. Here, our intent was to understand the nature of structural defects in poly(diacetylenes) introduced by the presence of surface constraints. Droplets of DCHD were prepared and polymerized in order to perform HREM to investigate local structure. The droplet sample geometry allows us to produce a number of defects for study including dislocations, cracks and free surfaces.

The crystal structure of DCHD monomer is monoclinic (Enkelmann, et al., 1977), with  $a=1.76$  nm,  $b=1.36$  nm,  $c=0.455$  nm,  $\gamma=94^\circ$ , and space group  $P2_1/c$ . The polymer crystal belongs to the same space group (Apgar and Yee, 1978), but with unit cell parameters  $a=1.739$  nm,  $b=1.289$  nm,  $c=0.490$  nm, and  $\gamma=108.3^\circ$ . Here we prefer the unit cell notation employed by Reed and Young (1984), which places the chain axis parallel to the  $c$  direction, as is conventional for crystallizable polymers.

## Experimental

### DCHD monomer synthesis

The DCHD monomer was synthesized with the assistance of Prof. Jeffrey S. Moore of The University of Michigan Chemistry Department using oxidative coupling of substituted alkynes. Carbazole (75 grams) was first dissolved in 750 ml dry THF. A separate vessel was then charged with NaH suspended in 150 ml of THF in a dry box. The NaH suspension was cooled to 0°C and carbazole solution was added dropwise over 10 minutes. Hydrogen evolution began immediately. At the end of the addition, it was warmed slowly to 50°C and a clear brown solution resulted after an hour. A third vessel was charged with 80 ml of propargyl bromide as a 80% solution in toluene along with 200 ml of THF. The carbazole solution was cooled to 0°C and the propargyl bromide solution was added dropwise. After 12 hours, the reaction mixture was extracted with CH<sub>2</sub>Cl<sub>2</sub> and water, the organic layer dried with MgSO<sub>4</sub>, and concentrated. A solution of 200 ml of pyridine, 200 ml of MeOH, and 100 gms of Cu(OAc)<sub>2</sub> were mixed together until nearly homogeneous. A solution of the acetylene was added and heated to reflux. A green color developed. The mixture was allowed to stand at room temperature for 18 hours. The contents were poured into 10 liters of water resulting in a blue cloudy suspension. The solution was filtered and the solids were washed with excess water, air dried, and then dried under vacuum. The crude product was allowed to dry overnight in the dark. The impurities were removed by extraction with acetone and then Et<sub>2</sub>O. Five grams of product was recrystallized from 600 ml of toluene. NMR



characterization showed that there were less than 1% impurities in the final product. The monomer was stored at  $-5^{\circ}\text{C}$  to avoid polymerization.

### **Sample Preparation**

A 0.01% by weight solution was prepared with white crystals of DCHD monomer and chloroform as-received from Aldrich. Droplets were prepared by flooding amorphous carbon-coated mica substrates with the solution and allowing the chloroform to evaporate at  $21^{\circ}\text{C}$ . The carbon film was floated onto the surface of distilled water and collected with copper grids for examination using TEM. Some samples were shadowed with gold metal in a Denton vacuum evaporator at an angle of  $12^{\circ}$ . Samples were either polymerized in a vacuum oven at  $150^{\circ}\text{C}$  for approximately 24 hours (Yee and Chance, 1978) or in the electron beam (Liao and Martin, 1993). Etched droplets were prepared by polymerizing the monomer thermally and then flooding the surface of the copper TEM grids with 100% chloroform. The grids were supported by a wire mesh in a petri dish and kept in a saturated chloroform atmosphere overnight until the chloroform evaporated.

### **TEM Operation**

The DCHD droplets were examined in a JEOL 4000 EX transmission electron microscope operating at 400 kV using a minimum dose system (MDS) and a beam-blanking device. A low-dose procedure for taking micrographs was employed to reduce electron radiation damage of the samples as reported by Martin (1990). Focusing was aided by a Gatan TV monitor and was performed at 200 kX. The procedure used was to move to a fresh area of a grid, focus on the edge of a droplet, move to a different area in search mode to look for droplets which had not been exposed to the beam,

and quickly take a micrograph in photo mode. This procedure greatly reduced the amount of radiation each droplet experienced by only focusing once on an area within the grid square. Imaging was typically done at a screen current of 20 pA/cm<sup>2</sup> and an exposure time of one second. For a magnification of 100 kX, this gives a total dose at the sample of 0.2 C/cm<sup>2</sup>. The electron damage sensitivity of the droplets was determined by monitoring the reflections in diffraction mode and measuring the amount of time until these reflections faded. After images were taken, the integrity of the sample was checked by returning to diffraction mode to make sure the reflections of interest were still present.

Selected Area Electron Diffraction (SAED) patterns were calibrated using gold evaporated onto the surface of the grid. Lattice spacings were calibrated using a He/Ne laser optical bench setup. Negatives of turbostratic graphite with 0.34 nm lattice spacings were used to give accurate measurements of lattice spacings at the same magnification.

Scanning electron micrographs (SEM) and Scanning transmission electron micrographs (STEM) were taken using a JEOL 2000 EX at an operating voltage of 200 kV. The samples were prepared as above and gold coated with a thin layer (approximately 20 nm) to increase contrast and minimize beam damage. The microscope was aligned using normal TEM procedures, but a scanning beam was used to generate both a SEM and STEM image simultaneously on dual screens. Beam damage in the sample could be monitored by marks left on the surface in the SEM image. SEM and STEM images were recorded of each area of interest in order to be able to correlate projection and surface information.

## Results and Discussion

Several different morphologies were found when examining the samples with TEM including small platelets, long needles, single crystals and droplets. Figure 2.1 shows a single droplet, shadowed with gold at an angle of  $12^\circ$  to highlight topological features and determine the height of the droplet. The maximum height of this droplet was measured to be on the order of 100 nm. The polymer chain was determined to be perpendicular to the beam from the SAED pattern shown in Figure 2.2. Closer examination of the diffraction patterns in relation to the micrographs showed that the cracks present in the droplets are parallel to the [001] (chain) direction. Individual droplets were not aligned in relation to each other. Most of the droplets were found to have a single orientation of the polymer chain axis. Figure 2.2 (a) shows a SAED of the droplet in Figure 2.1 in relation to the droplet. The diffraction pattern exhibits extra reflections that are not found in the single crystal pattern. The extra reflections can be accounted for if the droplet was crystallographically fiber-textured. Figure 2.2 (b) shows a simulation of a fiber-textured diffraction pattern using CERIUS 3.1 (Molecular Simulations Inc., 1991) and the unit cell proposed by Apgar and Yee (1978). The intensities of the reflections on the first layer line in the simulated SAED compare well to the observed diffraction pattern intensities. HREM micrographs have shown regions with 1.2 nm (010) and 0.8 nm (200) spacings next to each other, as would be expected for a fiber texture. A schematic diagram of this texturing is shown in Figure 2.3. On closer inspection of the data from epitaxial growth of DCHD by LeMoigne et al. (1991), their electron diffraction patterns also show extra reflections that would suggest fiber-texturing similar to that seen in our droplet experiments.



**Figure 2.1:** TEM micrograph of a droplet of poly(DCHD) shadowed with gold from an incident angle of  $12^\circ$ . The chain axis is in the plane of the substrate and runs parallel to the observed cracks.

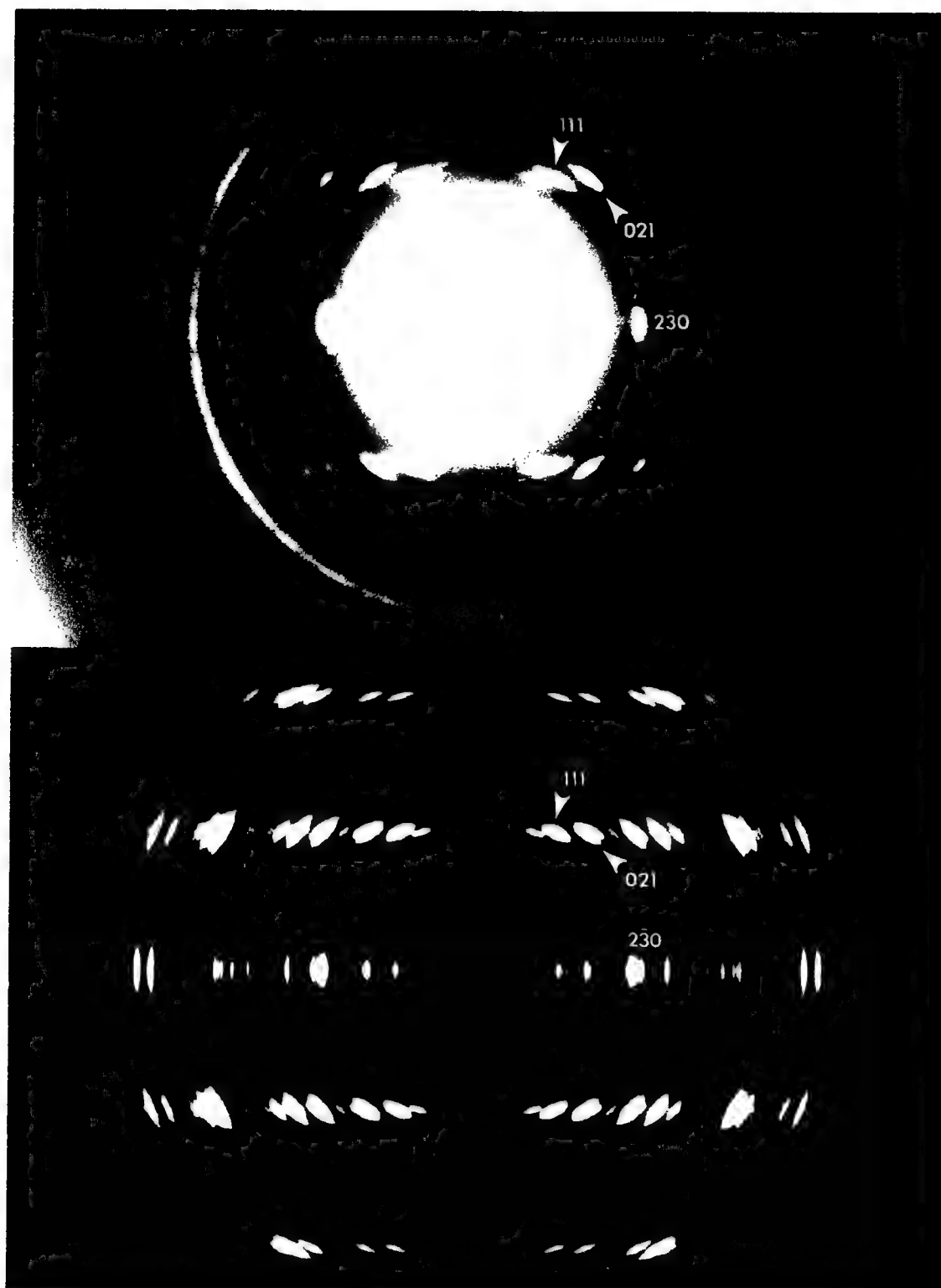


**Figure 2.2: (a) SAED of poly(DCHD) droplet. The reflections indicated are from different zone axes suggesting a fiber texture. (b) A simulation of the SAED pattern (CERIUS) using a fiber texture geometry for the reported polymer crystal structure (Apgar and Yee, 1978).**

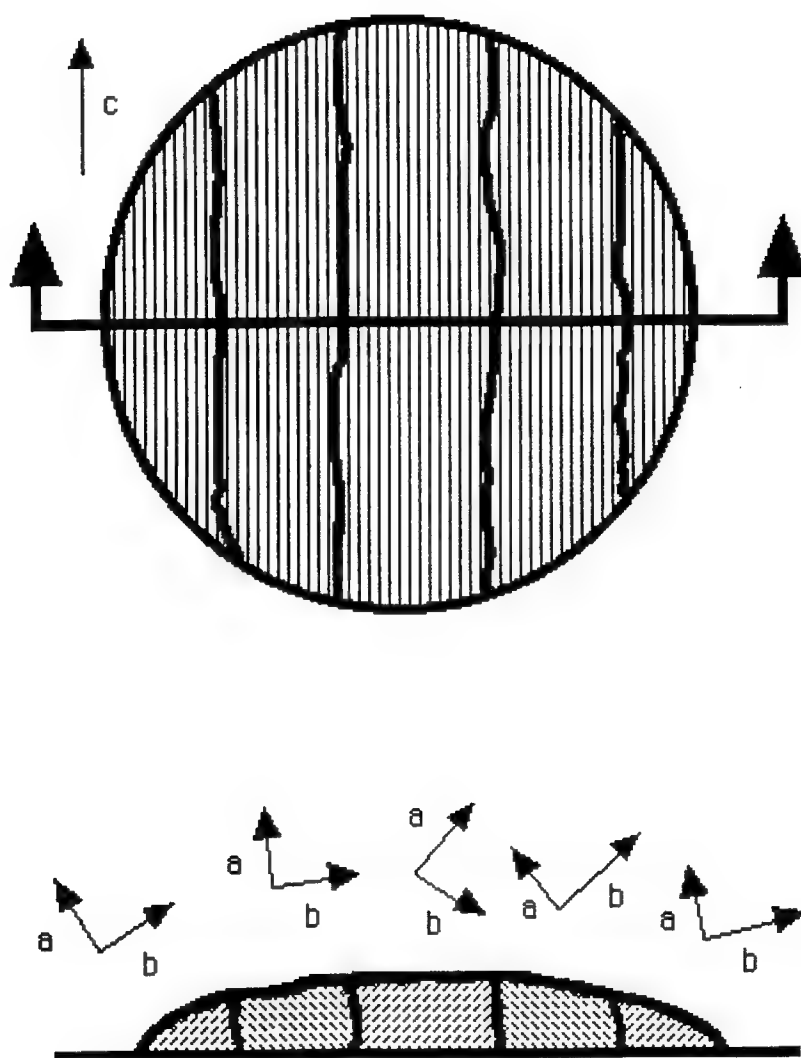


Figure 2.3: Schematic of droplet showing domains where the a- and b-axes are in differing orientations with respect to the substrate.

The ordering of the monomer during solvent evaporation should ultimately determine the defects induced in the final polymer state. Since the polymerization is a topochemical reaction (Enkelmann, et al., 1977), any defects present in the monomer structure after crystallization and drying should also be preserved in the polymer crystal.

The formation of the droplets apparently occurs via the breaking off of the chloroform solution into large droplets during the evaporation process. Since the solvent is more volatile than the monomer, the concentration of the solution rises as the solvent evaporates. As the critical solubility is approached (approximately 0.43% of DCHD by weight at room temperature), swollen monomer precipitates from solution. The droplet is then in a state where reorganization of the monomer units may be possible to conform to the locally curving droplet surfaces. As the last residual solvent from the swollen matrix is evaporated, the cracks form due to drying. The cracks may form at the boundaries between two different textures of the monomer crystal structure. It has been noted that the droplets are crystallographically textured with the chain axis in the plane of the substrate and the R groups rotated in differing directions in domains of single crystal orientation. This fiber texture could come about as a single nucleation event where all the monomer units lie in one predominant direction, but with the presence of solvent, choose to remain in one of several low energy habit planes as the solvent evaporates. As the swollen droplet with these different domains shrinks due to solvent evaporation, the domain boundaries might act as stress concentrators leading to cracking between them. Although most droplets have only one predominant orientation of the polymer chain, occasionally droplets can be seen with cracks running in two or more directions, cracks indicating the chain direction in those regions.

Lattice fringes were observed parallel to the cracks and over the entire droplet. We systematically observed bending of the polymer lattice fringes in regions near and parallel to the droplet edge. Figure 2.4 shows bending of the 1.2 nm (010) lattice fringes in the direction of the curvature of the droplet edge. The radius of curvature of the bending was determined to be 1.5 microns in this case. Several edge dislocations are also apparent in this micrograph with a Burger's vector of [010].

The area in question can be thought of as a perfect crystal that is bent as shown in Figure 2.5. In order to incorporate the strain in a bent lattice, dislocations will form to lower the total energy of the region (Nye, 1953). The geometrically necessary dislocation density can be calculated by determining the strain gradient over the bent crystal and dividing it by the Burger's vector of the dislocation needed to relieve the strain (geometrically necessary dislocations =  $1/rb$ ) (Courtney, 1990).

The dislocations needed to incorporate the bending can be envisioned as an extra monomer unit along the c direction or, after polymerization, as an extra repeat unit along the chain in relation to the chain on the compressive side. The Burger's vector in the polymer would be the (001) spacing along the chain axis, 0.491 nm. For this geometry there would be one dislocation needed every 735 nm<sup>2</sup> for the bending seen in Figure 2.4, corresponding to a dislocation density of approximately  $10^{15} \text{ m}^{-2}$ .

In metals, it is frequently found that dislocations will tend to polygonalize in a bent crystal forming a low angle tilt boundary (Nabarro, 1967). If Figure 2.4 is examined closely, the bending does occur between two regions which are tilted with respect to one another. The angle between the two areas is 5°. Using an analysis by Hirth and Lothe (1982), the spacing of dislocations along a symmetrical tilt boundary,  $D$ , is approximately equal to





Figure 2.4: HREM image of the DCHD droplet edge where the chain axis is parallel to the edge. The lattice fringes from the (010) planes can be seen to bend to conform to the droplet surface. Several edge dislocations with a Burger's vector in the [010] direction can be seen.

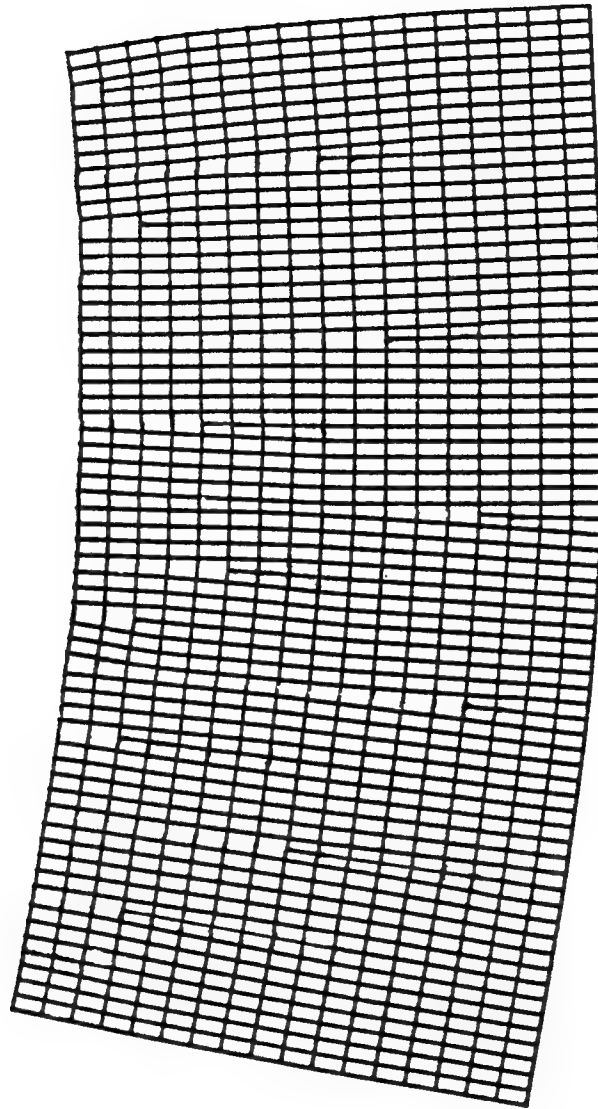


Figure 2.5: Schematic of a bent crystal with edge dislocations of the type  $b = [001]$  to incorporate the bending.

$b/\theta$ , where  $b$  is the Burger's vector and  $\theta$  is the tilt angle in radians. For edge dislocations with a Burger's vector along the [001] chain axis (0.49 nm), the spacing between dislocations would be 5.6 nm, which would correspond to a dislocation every five polymer chains in the [010] direction. Young and Petermann (1982) showed that similar tilt boundaries in toluene sulphonate poly(diacetylene) single crystals were formed when there was a large enough dislocation density.

Recent investigations of the morphology of nested fullerenes (Srolovitz, et al. 1994) have provided a theoretical framework to discuss bending energies for covalently bonded systems. Their calculations showed that a random distribution of edge dislocations incorporated to relieve bending strain was less favorable than low angle grain boundaries comprised of the same defect density. This is because the total bending energy is equal to the strain to curve the lattice (significant when the curvature is normal to the chain axis) plus the elastic strain energy of the geometrically necessary dislocations. Dislocations of the same sign and type are attracted to each other to form grain boundaries because their strain fields are diminished by canceling each other. This, along with a slight reduction of the lattice curvature between the grain boundaries, reduces the total bending energy. A further discussion of anisotropic bending energies will be discussed in Chapter III in reference to thin shelled DCHD spheres which are more appropriate to the analysis.

Dislocations with Burger's vectors along the c-axis have not been directly imaged to this date, due to the sensitivity of higher order planes to electron damage, although edge dislocations with a Burger's vector along the [010] direction have been imaged. This corresponds to an extra polymer plane

inserted parallel to the electron beam direction. Such edge dislocations can be seen in Figures 2.4 and 2.6.

Figure 2.6 shows a subgrain boundary near the edge of a droplet. Figure 2.7 is a tracing of this image which highlights the positions of the 0.8 nm (200) lattice fringes which are parallel to the polymer chains. Several edge dislocations of the type [200] can be located along the boundary. These dislocations represent the mutual segregation of a number of chain ends to a line parallel to the direction of the electron beam. The dislocations tend to aggregate together in groups of two or three to make one larger dislocation, as can be seen in Figure 2.7.

Close examination of the image reveals that certain chains terminate at the boundary, whereas others apparently remain continuous across the boundary. The curvature of the lattice near the droplet surface results in a local splay deformation (divergence) of the polymer chains. In order to preserve the density of the material, it is necessary to incorporate extra chains within the region where their orientation is diverging (Kléman, 1983). Figure 2.8 shows a schematic diagram illustrating the nature of this deformation in which the chains are represented as solid lines. The region roughly corresponding to Figure 2.6 is shown as a solid box.

The presence of these chain-end dislocations, due to the local bending of the lattice near curving surfaces, has implications for device fabrication. DCHD is of interest because of its high third-order nonlinear susceptibility [ $\chi^{(3)}$ ] (LeMoigne, et al., 1991). A recent analysis by Hone and Singh (1992) has considered the theoretical effect of bond-breaking defects on  $\chi^{(3)}$ . They found a decrease of the theoretical  $\chi^{(3)}$  with increasing defect concentration.

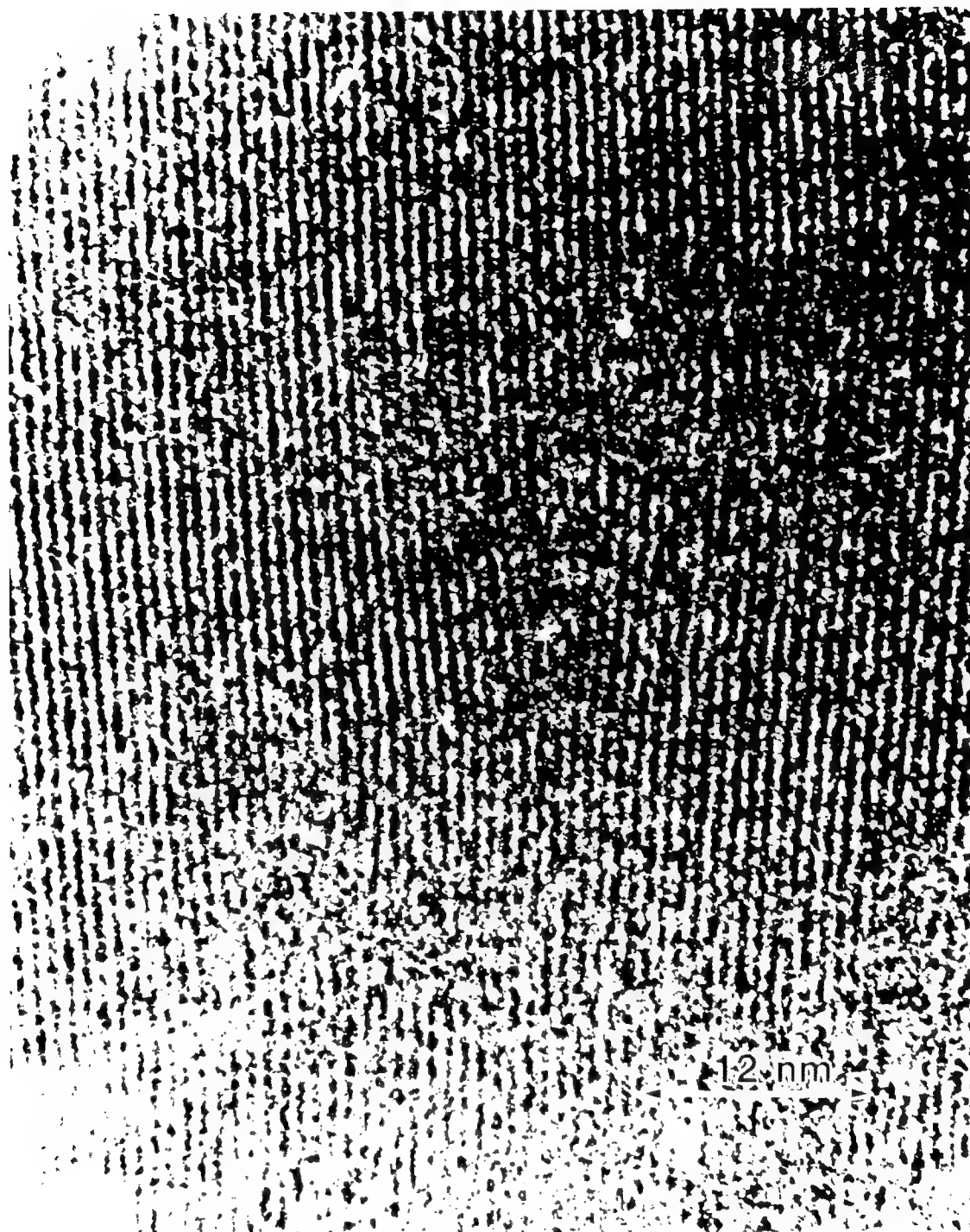


Figure 2.6: HREM image of a low-angle tilt subgrain boundary in a DCHD droplet. The lattice fringes being imaged are the (200) planes with a spacing of 0.8 nm and correspond to the spacing between chains. The Burger's vector is [200] with a magnitude of 0.8 nm. Around the dislocaitons there is a region of crystal where the contrast does not give rise to lattice fringes; these areas measure appoximately 6 nm to 36 nm. The distance between the imaged dislocations is approximately 7.0 to 12.0 nm.

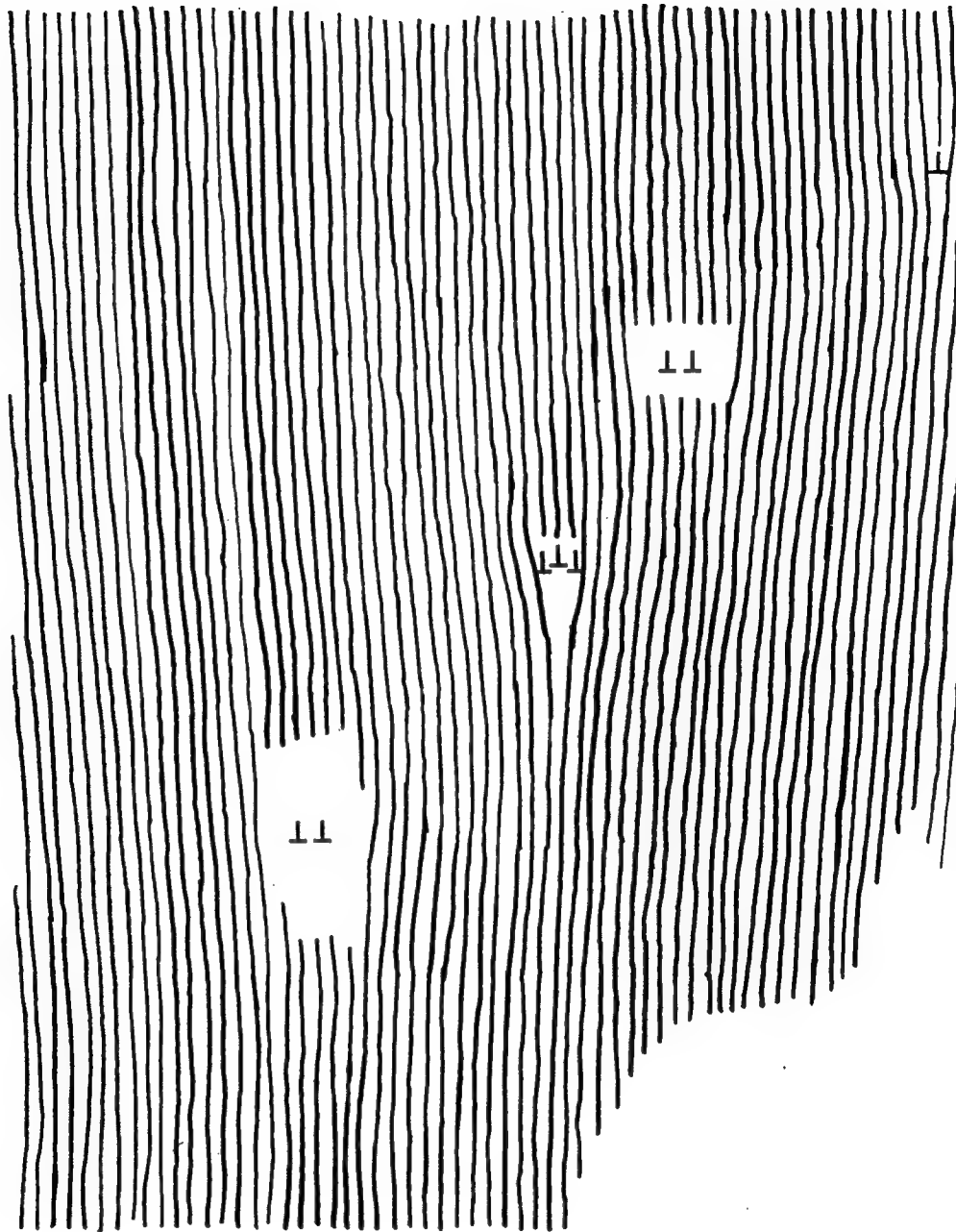


Figure 2.7: A schematic showing lattice fringes as lines to highlight the position of chain end dislocations in Figure 2.6.

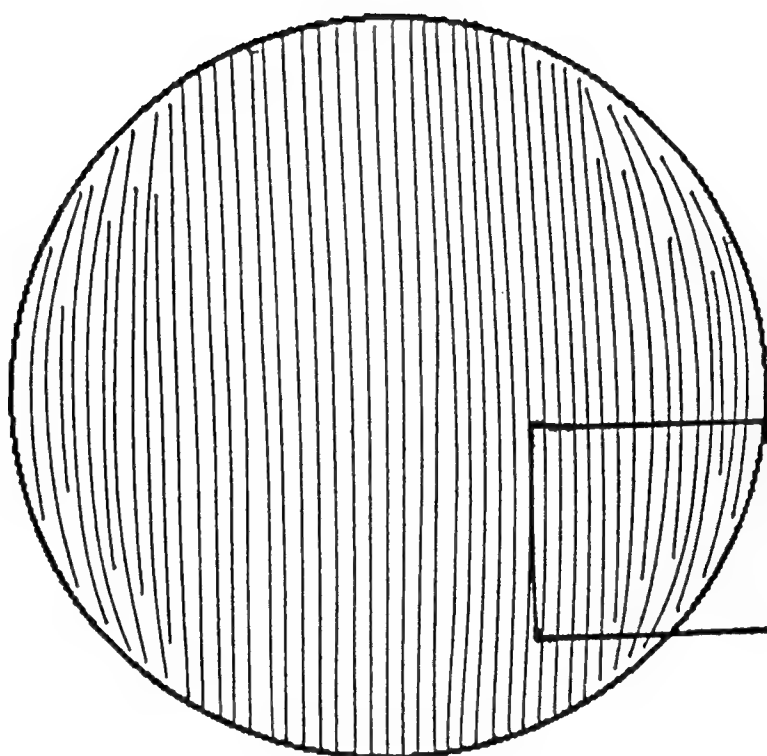


Figure 2.8: Schematic showing the general orientation of the chains with respect to the edge of the droplet. With the incorporation of bent chains, several subgrain boundaries are created near the edge of the droplet. The rectangle shows the region imaged in Figure 2.6.

The regions around the dislocations where contrast is lost are measured to be between 6 nm in the chain direction x 5 nm in the lateral direction and 36 nm (chain direction) x 30 nm (lateral direction), depending on the number of single dislocations that have aggregated together. The length between defects is 7.0 to 12.0 nm. This corresponds well to the calculated distance,  $D$ , for this type of tilt boundary, which is 11.5 nm.

Figure 2.9 also shows an etched droplet taken as a defocused (000) diffraction spot with holes in lines perpendicular to the chain direction. The holes appear to be grouped into lines with distances between lines of holes to be approximately 125 nm. Figure 2.10 is a SEM and STEM image taken of a poly(DCHD) droplet. A comparison of the light areas of contrast on the STEM picture to actual holes shown in the SEM of the same droplet show that there are both holes in the surface and holes in the bulk of the sample that do not continue to the surface. Regions of light contrast in the STEM image marked A are voids whereas the regions marked B are holes as seen in the SEM image. Many of the holes in the surface may be attributed to etched areas of unreacted monomer.

Gerasimov (1990) has found that the application of hydrostatic pressure during polymerization retards polymerization of DCHD because of the unfavorable overlap of the  $\pi$  orbitals, but increases polymerization in poly(TS). A greater than 50% decrease in polymerization yield in DCHD crystals when thermal polymerized at 150°C at 4 kbar for 40 min. The DCHD polymerization is retarded under hydrostatic pressure in both thermal and photoinduced polymerization. The applied pressure causes the monomer crystal to be compressed in the direction of the growing chain. The increase in deformation is thought to increase the bond angle deformations causing a





**Figure 2.9:** TEM micrograph of a polymerized DCHD droplet that was etched with a chloroform solution. The micrograph was taken in diffraction mode as a defocused (000) spot in order to increase the contrast. Arrows point out lines of possible etch pits that have polygonalized as a result of bending of the lattice at the edges.

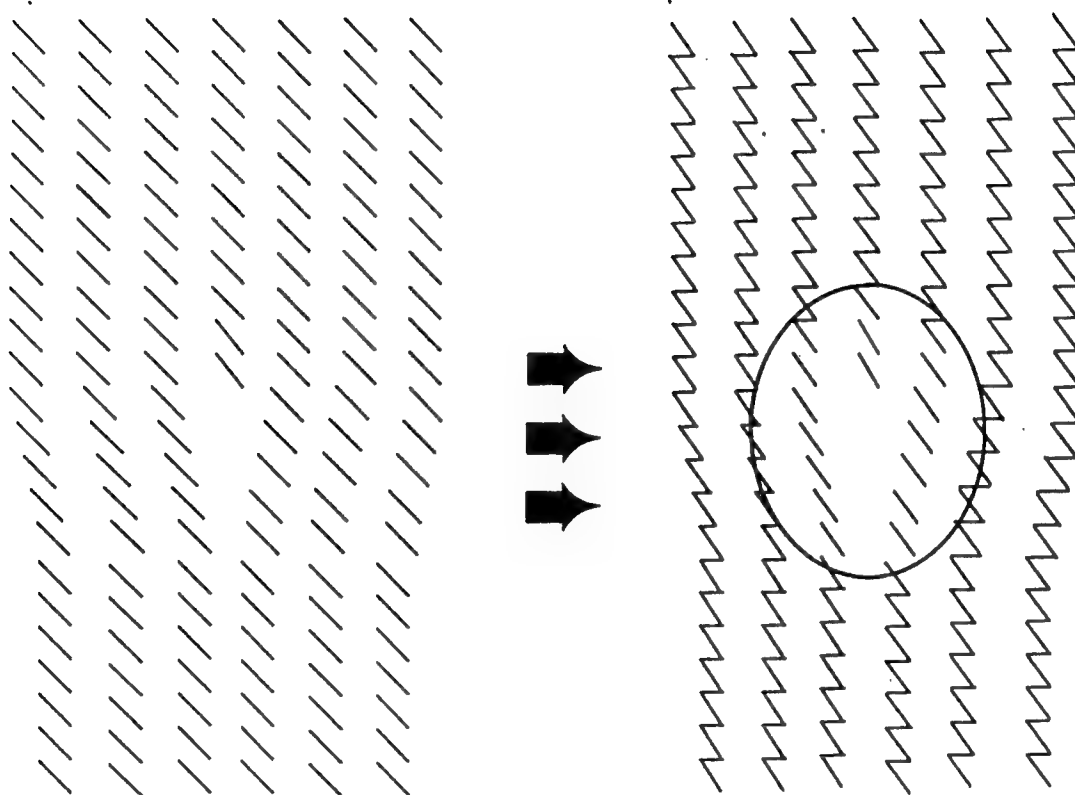


Figure 2.10: (a) STEM image of etched poly(DCHD) droplet showing regions of low light contrast that correspond to voids (A) or surface holes (B). (b) SEM image of the same area of droplet that shows corresponding holes (B) in the surface versus areas that have no surface holes.

twisted chain formation that hinders further chain growth. Defects in the monomer lattice may affect the polymerization by retarding the polymerization in the neighborhood of the defect in regions of heterogeneous hydrostatic pressure. The area of monomer units that would remain unpolymerized could be related to the size of the dislocation core by the area over which the misfit of the dislocation extends. Young and Petermann (1982) examined this question by using the model by Frenkel and Kontorova, which is applicable for isotropic solids, and applying it in one direction in the polymer using averaged data available for the poly(TS) system. They found that the misfit would extend over about 30 structural units for a dislocation with a Burger's vector along the chain axis. Given this, it could be expected that a reasonable amount of monomer would remain unreacted in the area of an edge dislocation with  $b$  along the  $[010]$  direction. A schematic of an edge dislocation in DCHD monomer and the resulting area after polymerization of the crystal is shown in Figure 2.11. There is a region around the defect where the monomer polymerization is retarded. These regions of unreacted monomer could be etched out using a solvent that does not affect the polymer.

Schermann et al. (1975) have reported etching dislocations at the surface of poly(TS) monomer crystals. Their observations were made via scanning electron microscopy and optical microscopy. The size of pits observed were of the order of 2-5  $\mu\text{m}$ .

Etching experiments in our laboratory have shown lines of holes perpendicular to cracks and the droplet edge (Figure 2.9), which would indicate that they were unreacted monomer around arrays of dislocations formed by the bending of the lattice. Further SEM/STEM experiments on



**Figure 2.11:** A schematic showing an edge dislocation in the monomer lattice of type  $b = [001]$  and the resulting transition to polymer with a region of unreacted monomer near the dislocation as a result of misorientation of the monomer units outside of the necessary polymerization parameters.

etched droplets showed that certain regions of light contrast found in TEM images correspond to holes in the surface which are consistent with the presence of etch pits from dislocations. These studies also revealed that there are also voids inside the crystals that are not from dislocations but give rise to contrast in TEM. This observation illustrates the importance of determining which of these holes continue to the surface. Measurement of the holes yield sizes that are consistent with regions of low contrast at the dislocation core in lattice images of grain boundaries shown in Figure 2.6. In both instances, the size of the disordered regions are approximately 6 nm square to 36 nm square, with a 1-6 nm elongation in the chain direction. This results in an average length to width ratio of 1.2. This range corresponds to regions produced by single dislocations up to dislocations that are actually several dislocations of the same sense.

### Conclusions

Droplet experiments with diacetylenes have been shown to be useful in determining local structure around individual defects. At droplet edges that are parallel to the chain axis, the polymer molecules exhibit a local curvature. The curvature of the polymer chains is thought to be the result of the conforming of the monomer precursor crystal structure to the curving droplet surface. Dislocations with the Burger's vector parallel to the chain axis are needed to incorporate the bending. Examples of polygonalization of the bending are the result of aggregation of these defects. The formation of low angle grain boundaries observed is predicted on energetic arguments. Dislocations in the monomer structure may affect the ability of monomer units to polymerize, leading to regions of unreacted monomer that can be

removed to gain information on the size and shape of dislocation cores. Etching of droplets has given rise to etch pits that are approximately 6 nm square to 36 nm square with a slight anisotropy in the chain direction. The size variation is attributed to the aggregation of defects such as in grain boundaries where three or more single dislocations were imaged.

This study shows the importance of surface constraints on the perfection and orientation of the polydiacetylene crystal lattice. Fabrication of electro-optical devices made of similar materials will need to be carefully controlled to avoid defects which may adversely affect performance.

# **CHAPTER III**

## **EFFECT OF THREE DIMENSIONAL FREE BOUNDARY CONDITIONS ON THE CRYSTALLIZATION OF DIACETYLENES**

### **Introduction**

In the previous chapter we investigated crystallization in two dimensions under the influence of both a free surface and a substrate. In this chapter the substrate surface will be removed to investigate three-dimensional free boundary conditions. As hemispherical droplets were formed in the latter, complete spheres of DCHD are expected to form under these constraints.

The crystallization of small organic molecules in spherical boundary conditions has not been as well explored as that of the crystallization of metals. Having a greater understanding of how small molecules are affected by the free surface in their organization may lead the way for the exploitation of properties dependent on defects. Our previous work using diacetylenes to crystallize while confined in a droplet of solution on a substrate showed that the curved surface induced bending of the crystal lattice. This bending was mediated by the formation of dislocations to alleviate the bending strain. Dislocations are known to be areas of higher energy and as such, regions around them should dissolve at a higher rate than the bulk material. A similar use of this mechanism was described by Fitzgerald and Corrigan (1993). The system was dilitiazem and poly-lactide-co-glycolide, and drug

release was hypothesized as attack at lines of strain in the polymer matrix by hydrolysis. This would break the polymer into smaller oligimers and those areas would show greater water permeability than the matrix. Further lines of strain in the matrix would be attacked to create a porous matrix from which the drug could escape. Exploitation of this effect by the control of defect density could have important implications for the pharmaceutical industry.

The formation of spheres from atomized material is a process of industrial importance spanning a variety of disciplines such as the food, herbicide, pharmaceutical, ceramic, and chemical industry. Particles are formed for different functions but most notable is the controlled delivery of drugs, flavors, nutrients, or pesticides. These functions require that the particle be designed to dissolve or release its contents in a known manner at a specified time.

Common schemes to control drug delivery are to encapsulate the material in a polymeric shell or matrix chosen for its properties. Principally research in this area has focused on describing the diffusion characteristics of the drug/herbicide/etc. through the shell or matrix and exploring different host systems. Qualitative work has been presented on the effects of the morphology of the host on the delivery, but little systematic quantitative work has been explored. In the case of drug delivery, a limited number of polymers are acceptable for use in-vivo, thus the ability to control the morphology of these materials may provide a greater number of options for delivery system design. As an example, the same host system may be used to deliver pharmaceuticals to different body sites by controlling the crystallinity of the host and thus the diffusion rate of the drug. In order to accomplish the goal of selective delivery, studies on the effect of surface constraints and processing on morphology development need to be explored.



The most common example of morphology driven release is that of poly(lactic acid) where the mechanism of bioerosion is the hydrolysis of the backbone (Sinko and Kohn, 1993). There are two configurational forms of the polymer backbone, the racemic poly(D, L-lactic acid) and the stereoregular poly(L-lactic acid). The stereoregular polymer is semicrystalline and thus more dense than the amorphous racemic polymer, making the bioerosion rate much slower. Similar relationships exist for glassy vs. rubbery forms of polymers, since there is less free volume in the glassy phases, erosion and diffusion are limited. Thus plasticizers are often added to keep systems above their  $T_g$ .

Recent work by Greene, et al. (1993) uses an increase in soil temperature to trigger pesticide release. The pesticide is encapsulated in a matrix of polymer with a flexible backbone and crystallizable side groups. The temperature for melting of the side groups is tuned by the length of the side chain. They claim they can set the  $T_m$  between a range of  $0^\circ$  and  $65^\circ\text{C}$  within  $1\text{-}2^\circ\text{C}$  using a set of acrylic polymers. Once the soil reaches the melting temperature of the side chains, the conversion to amorphous polymer increases the ability of water to dissolve the pesticide. For advances in controlled release technology, more innovative designs based on morphology control should be investigated.

The goal of this study was to fabricate spheres of diacetylenes with free boundary conditions and examine how these conditions control the crystallization and to determine what defects are produced. Diacetylenes were used because they crystallize as small molecule monomers and then undergo a solid state phase transition to polymer crystals which preserve the defects from the monomer state. This reaction can be induced either by thermal, gamma, UV, or electron irradiation. In order to closely examine the

microstructure of the sub-micron spheres, a material with high radiation resistance was needed to perform electron microscopy. DCHD (1,6-di (N-carbazolyl)-2,4 hexadiyne) was chosen for its radiation stability and because it crystallizes in the small molecule state.

Precedent for crystallization in spherical boundary conditions is found in metal alloy systems. Kim et. al. (1988) showed that the iron-nickel system could be electrohydrodynamically atomized as a melt into a vacuum to form spheres. The spheres were sub-micron sized and exhibited a morphology transition with increasing size of the spheres. The spheres supercooled rapidly because of their small size and preserved the nucleation structure. Most of the spheres were either FCC or BCC single crystals, depending on the alloy composition, as confirmed from SAED. Smaller spheres tended to form an amorphous phase. This transition was approximately 30 nm in diameter, depending on the composition of the alloy. In the transition range spheres with both crystalline and amorphous components were found. The authors attribute the transition from amorphous to crystalline structure as indicative of faster supercooling rates as the diameter of the sphere decreased. Their study correlated well with theoretical predictions (Lin, et. al. 1988) of the nucleation of phases from classical nucleation theory.

Similarly, Bellare and Thomas (1989) formed spheres of poly(styrene-butadiene) block copolymers as an extension of droplet studies by Henkee et al. (1988). Henkee had found that the middle of the spheres showed lamellar, cylindrical, or spherical microdomains as seen in bulk systems, but in the thin peripheral region the bulk organization was inhibited. Morphologies exhibited suggested that the change is mediated by energy constraints. The phase component with the lower energy would be found at the surface. The removal of the substrate allowed the block

copolymer to organize the layers into concentric spheres about 100 nm in diameter. Without the influence of the substrate on the system energetics, the morphology might be dependent on a competition of the bulk, surface, and defect energy. The small size of the Bellare and Thomas spheres might provide the point defect of the concentric circles because the surface energy is the dominant term forcing the lower energy butadiene component to the surface. As the radius increases, different morphologies might form because of this competition of energy.

In our study, we have a system which crystallizes under a phase transition caused by a concentration difference from evaporation of the host solvent, unlike the cooling transition of liquid to solid. We might expect some morphology differences on that basis because of a loss of mass in our system that is not seen in metal systems.

The amorphous to crystalline transition as the sphere diameter is increased seen by Kim et al. is indicative not only of nucleation dynamics but also might be an effect of an increase in the number of defects in order to accommodate the high radius of curvature of the surface.

## Experimental

Diacetylene spheres were formed from a saturated solution of DCHD in chloroform at 0.434 wt. %. The solution was atomized through a port in a glass column (Figure 3.1) 70 cm tall and 4.5 cm in diameter. The column was closed at the top and open at the bottom to allow for sample collection and has four ports for the introduction of gases to control the evaporation rate if desired. The dried spheres were collected after 49 hours at the bottom of the column on a piece of carbon coated mica. The carbon film was floated onto the surface of deionized water for collection with copper TEM grids. Samples

were then gold shadowed to provide better contrast for TEM, SEM, and an internal calibration standard for SAED.

TEM, SAED, and HREM were performed on a JEOL 4000EX operated at 400 kV according to the low dosage operating procedures described by Wilson and Martin (1992). Diffraction patterns were recorded on spheres in the orientation they were found on the substrate. SEM and STEM images were collected using a JEOL 2000FX operated at 200 kV.

## Results

Transmission electron microscopy revealed a distribution of sphere sizes on the substrate. Spheres produced from a tower height of 65 cm ranged in size from 0.1 to 1.36  $\mu\text{m}$ . The distribution is shown in Figure 3.2. Gold shadowing at an incident angle gave an indication that the height of the spheres is nominally equal to their diameter. Upon closer examination, many of the spheres had regions of lighter contrast in the center or near the edge. Figure 3.3 is a composite of several spheres to illustrate the orientations and general morphology exhibited. A close up view of a representative sphere, seen in Figure 3.4, shows the region of lighter contrast more clearly. The edges of the spheres were relatively well defined with a few cracks running radially from the surface. Scanning electron microscopy along with STEM of the same sphere revealed that the regions of light contrast were holes in the surface (Figure 3.5). Because most of the spheres showed light contrast in TEM or holes in SEM, it was plausible that there were holes directly opposite each other making it more probable that a hole would be seen. Tilting spheres and recording both SEM and STEM images confirmed this hypothesis (Figures 3.6 and 3.7).

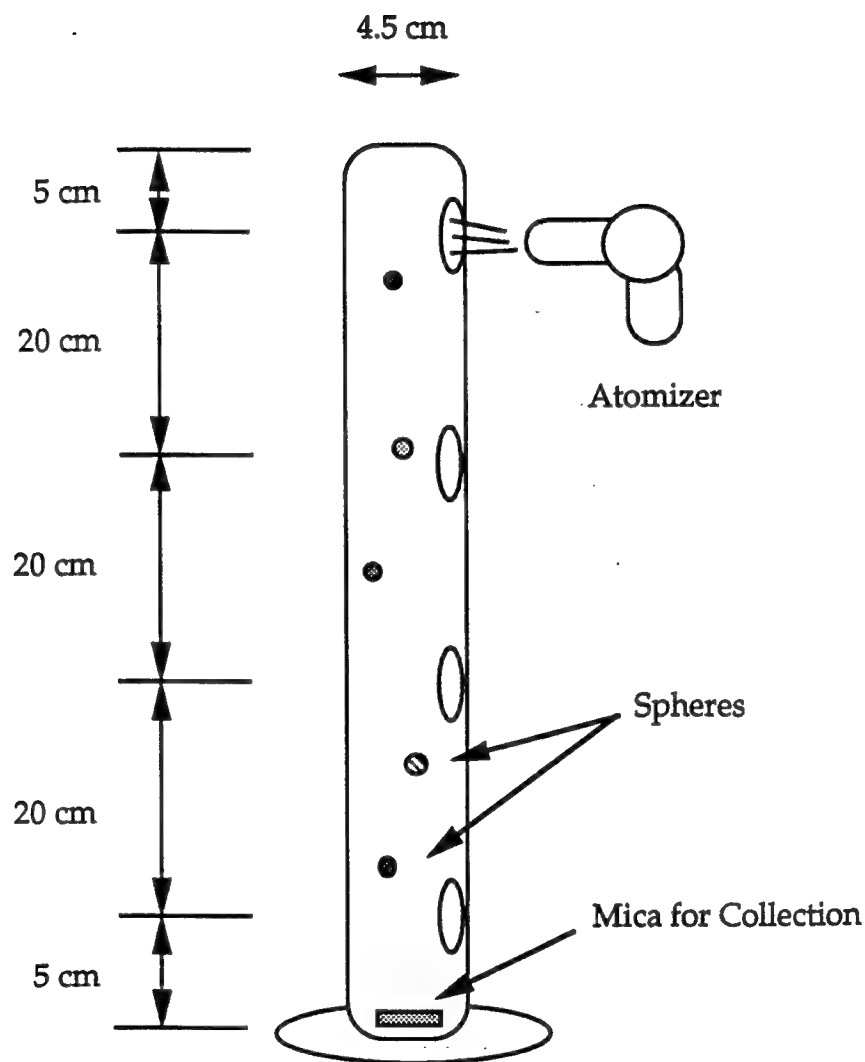
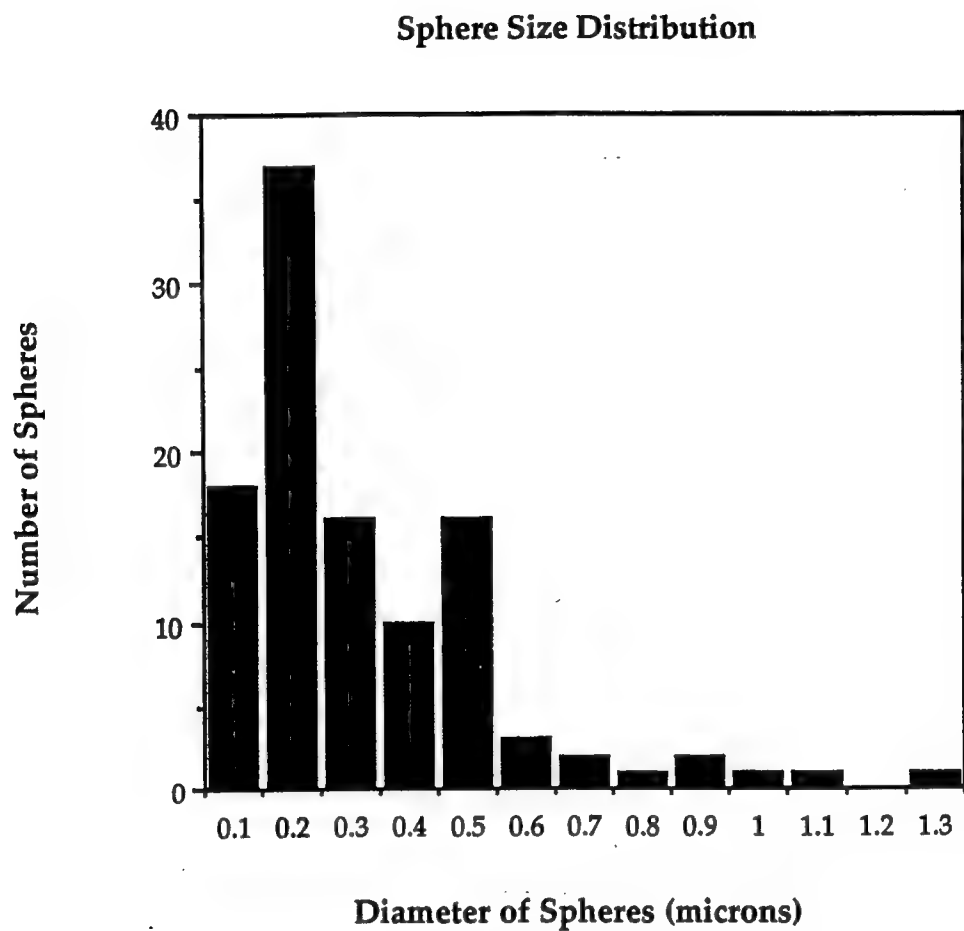
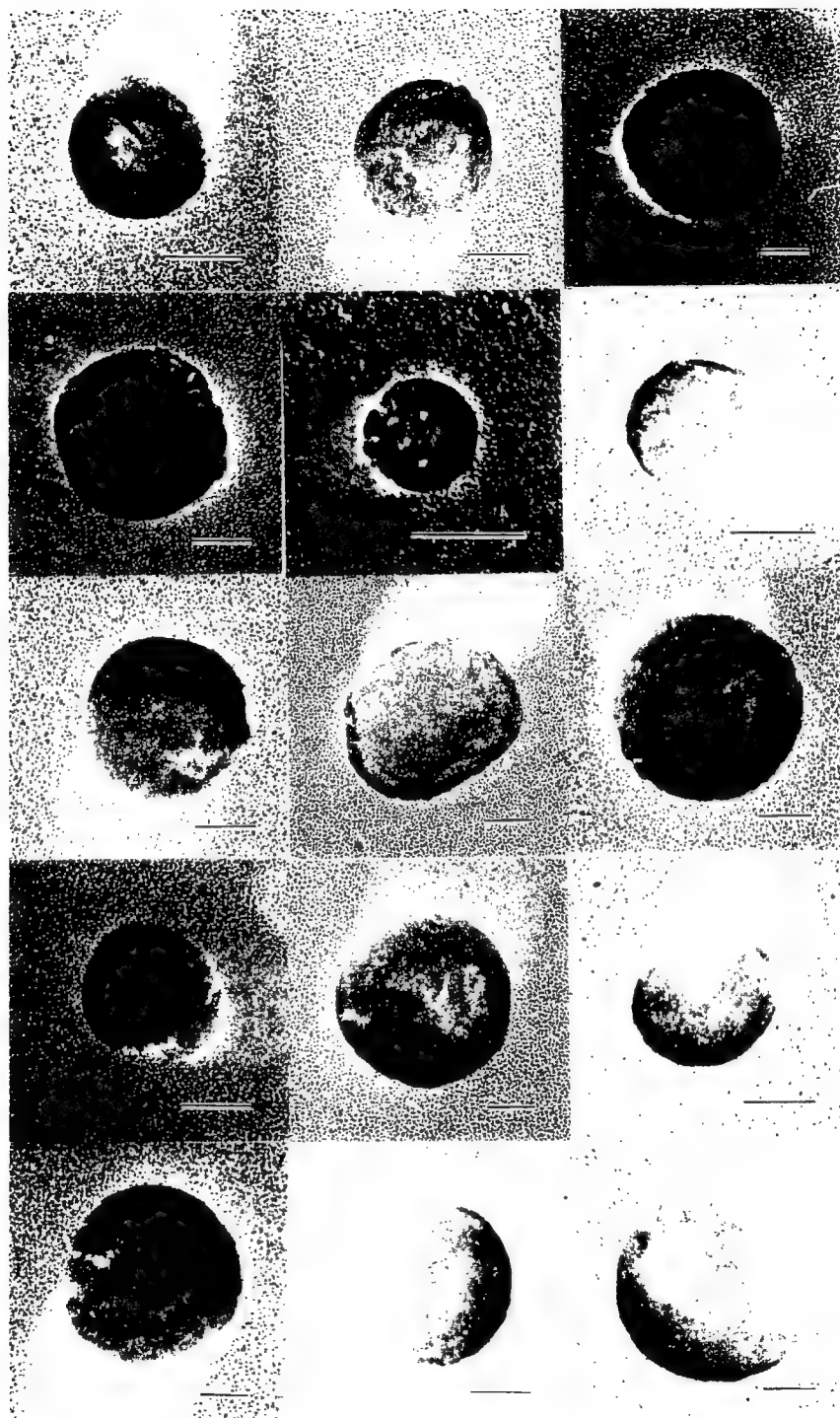


Figure 3.1: Schematic of glass column apparatus used to form spheres for study. The column is 4.5 cm in diameter and 70 cm high with four ports spaced 20 cm from each other. The spheres in this study were produced by atomizing solution at heights of 65 or 45 cm and allowing them to evaporate and settle under normal atmospheric conditions onto a collection media.



**Figure 3.2: Size distribution of spheres collected for 49 hours after atomization at a height of 65 cm under normal atmospheric conditions.**



**Figure 3.3: A composite of fifteen spheres imaged with TEM from a grid. The calibration bar is 0.2  $\mu\text{m}$ . Many of the spheres show both smooth and irregular outlines and areas of light contrast. The regions of light contrast indicate less dense regions.**

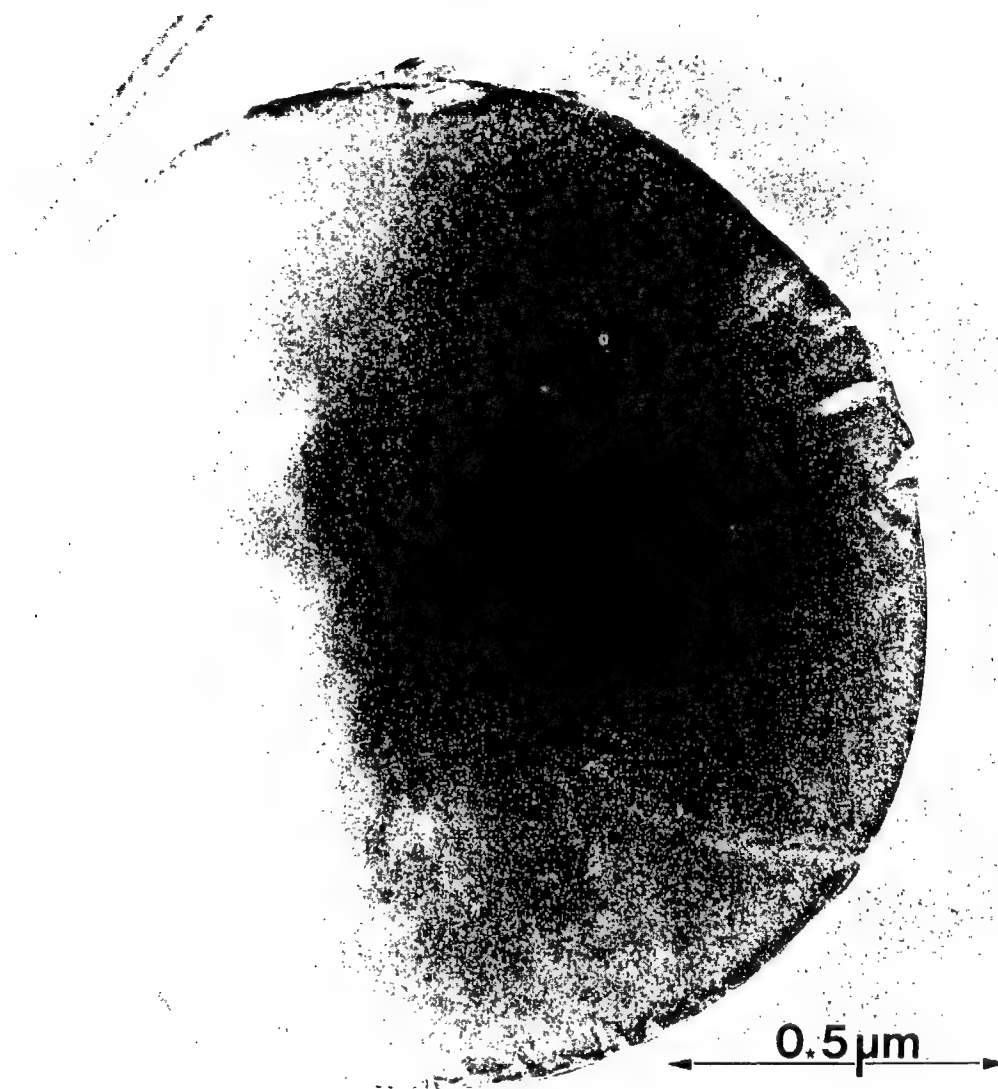


**Figure 3.4:** TEM image of a single sphere highlighting the region of light contrast believed to be a hole in the sphere. In general the perimeter of the sphere is smooth and sharp with few cracks emanating from it.



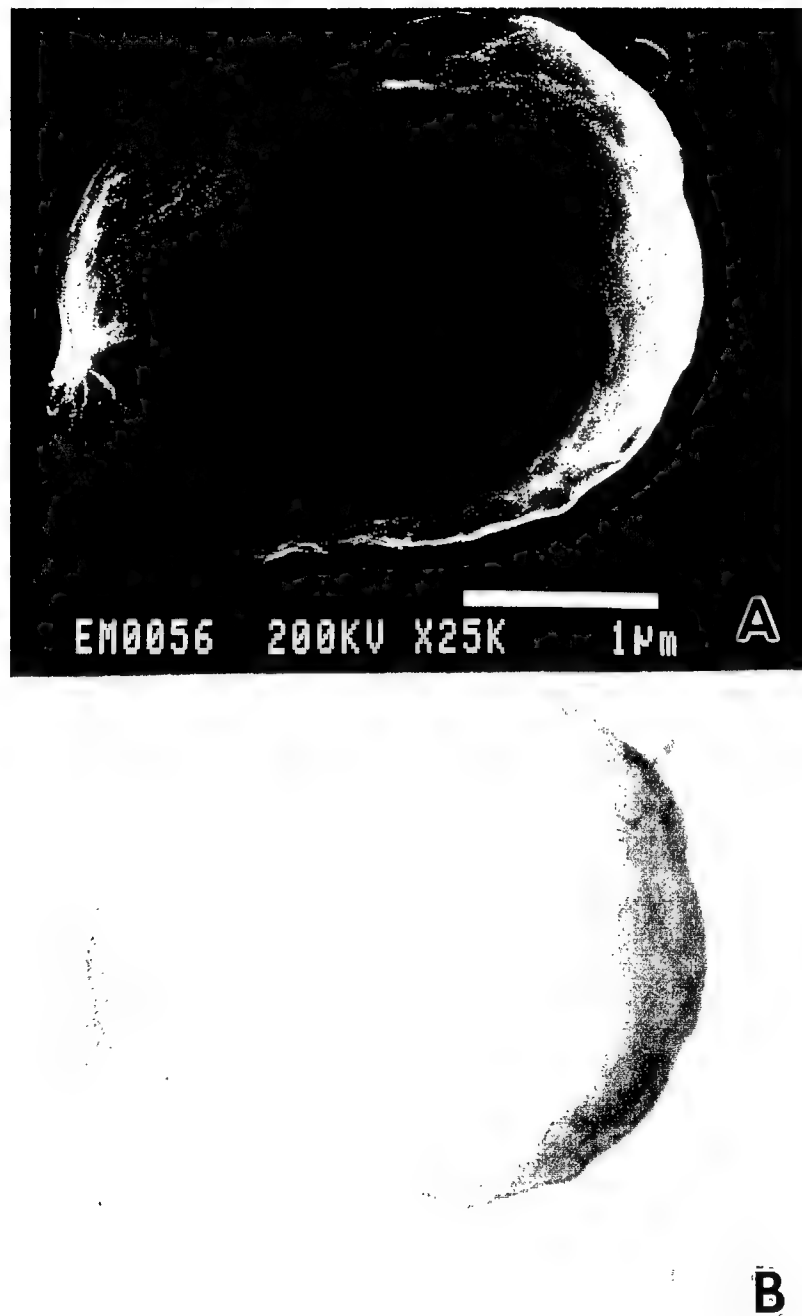


Figure 3.5: (a) SEM image of a large sphere showing two holes in the surface parallel to the beam. (b) STEM image of the same sphere with light regions of contrast that correspond to the holes in (a).

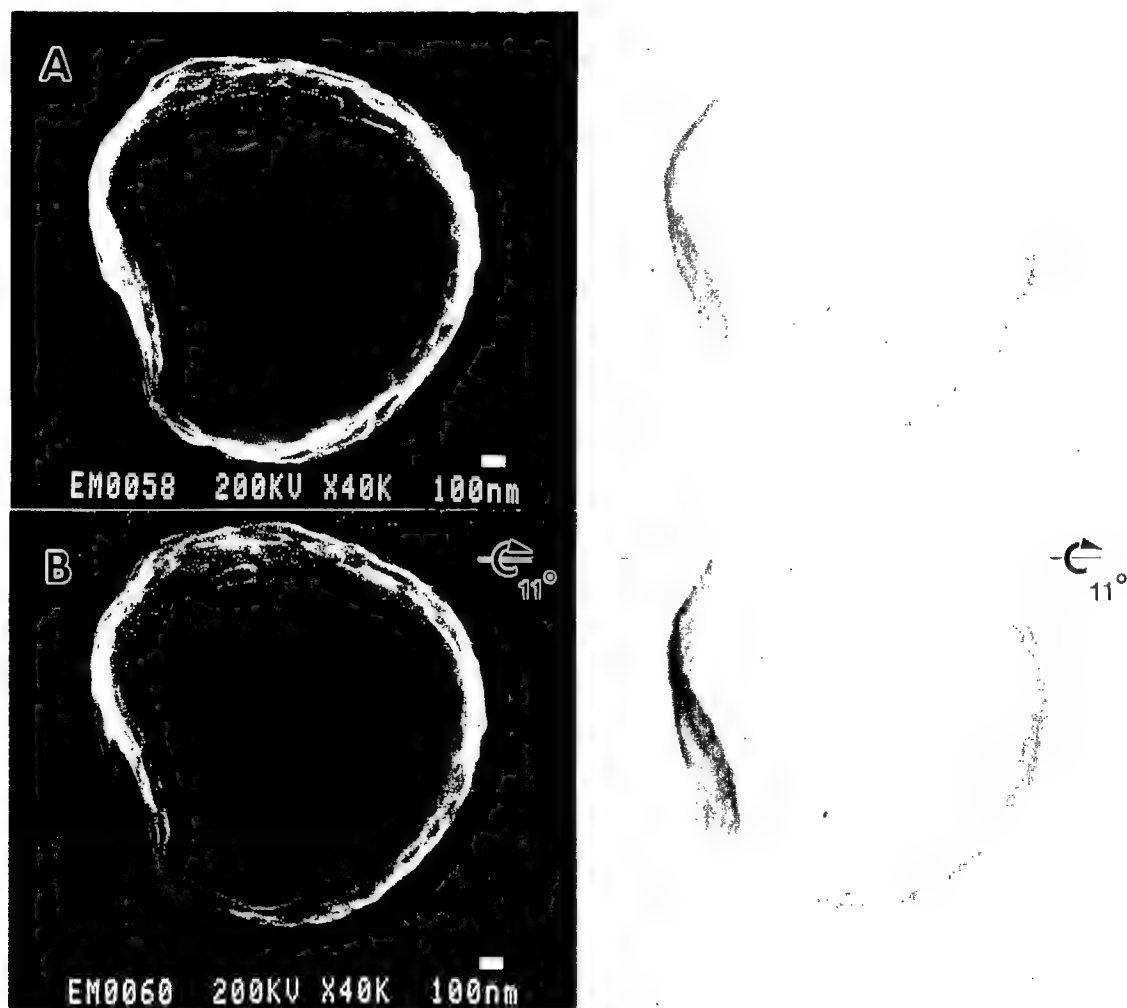


Figure 3.6: (a) SEM and STEM pair for a sphere with two holes, looking down the hole axis. (b) SEM and STEM pair of the same sphere tilted  $11^\circ$  confirming the existence of the holes.

**Figure 3.7: Tilt series of a one micron sphere. (a) SEM and STEM images of the sphere on the substrate. Two regions of light contrast are seen in the STEM image, which are believed to be holes. (b) SEM and STEM pair of the same sphere tilted  $47^\circ$  in the x-direction and  $30^\circ$  in the y-direction to bring a hole into view. The SEM image shows rough edges tilted into view and the corresponding STEM image shows a greater area of light contrast. (c) SEM and STEM pair tilted in the opposite direction by a  $30^\circ$  tilt along the y-axis from the original orientation. A second crack or hole is brought into view as noted by the rough area in the SEM image and light contrast in the STEM image.**

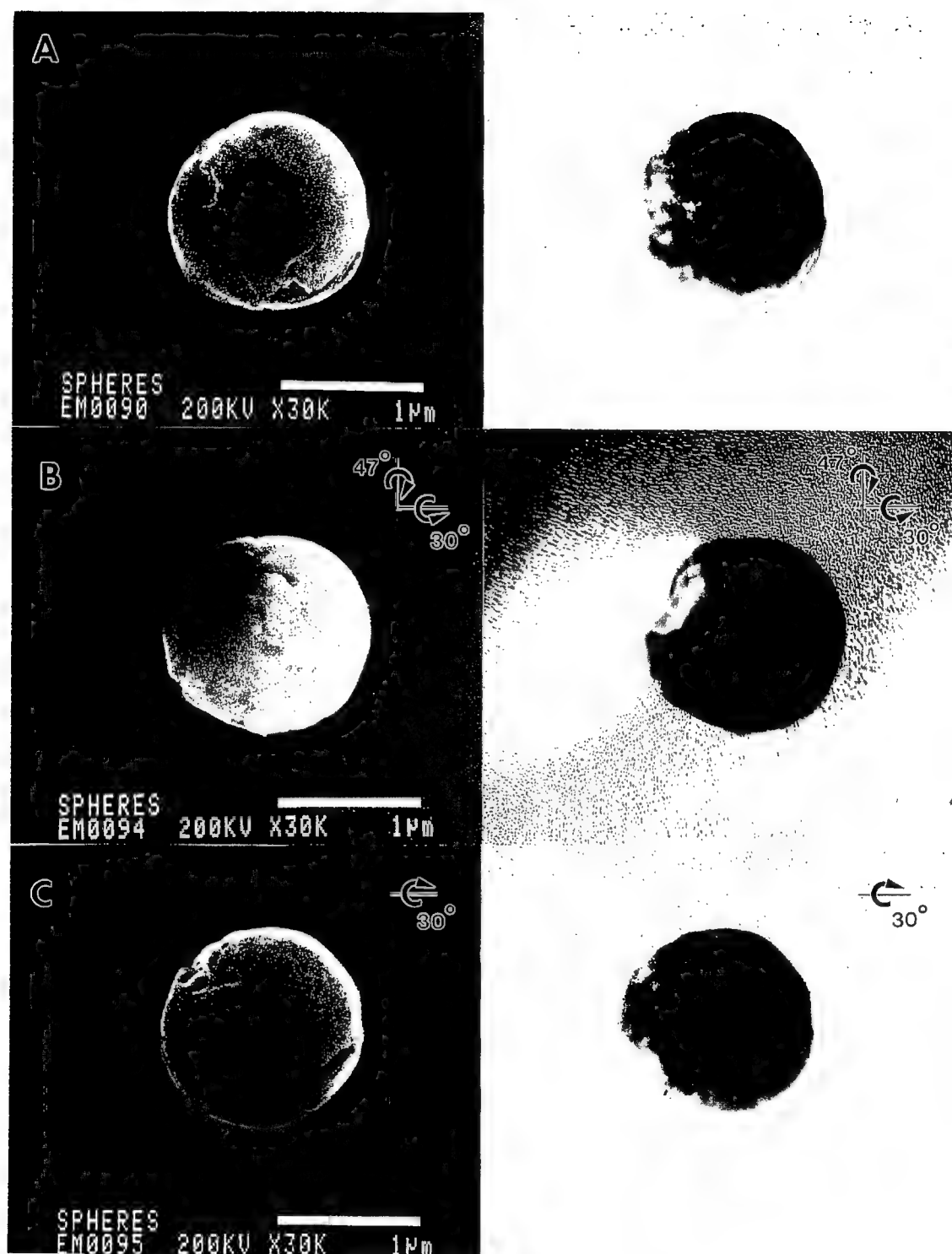


Figure 3.7

Spheres appeared to be hollow shells, as illustrated by TEM images of spheres which showed a rim of darker contrast at the edge approximately 70 nm in thickness (Figure 3.8). This was produced by the greater mass of the hollow sphere at the edge in projection than in the middle. SEM observation also corroborated this data showing in some spheres peeled back portions of the hole edge (Figure 3.5).

The surface of the sphere varies in quality from the perimeter of the holes to the sides. Figures 3.9 and 3.10 are examples of spheres where the axis joining the holes is parallel to the substrate. The surface near the holes is rough and characterized by what appear to be cracks and the ends of crystallites. The region closer to the equator appears uniform, smooth, and sharp.

HREM can be performed on the thin edges of the spheres. Figure 3.11 is an example of a sphere where the hole axis is parallel to the substrate, the insets of fringes show the polymer chain bending in response to the curvature of the sphere edge. The fringes have a spacing of 1.2 nm which corresponds to (010) planes. This corroborates with the SAED pattern in Figure 3.10 which shows arcs of spacing 0.83, 0.62 and  $0.41 \pm 0.02$  nm. The 1.2 nm arc is obscured by the inelastic scattering. The break in the arcs coincide with the hole axis suggesting that the polymer chains bend in response to the curvature. Table 3.1 lists spacings and sphere orientations for several SAED patterns recorded.

### Discussion

Spray drying is the dominant process by which spheres are formed in industry. In general, spray drying involves the dissolution or suspension of the material in a liquid followed by atomization at the top of a chamber. The

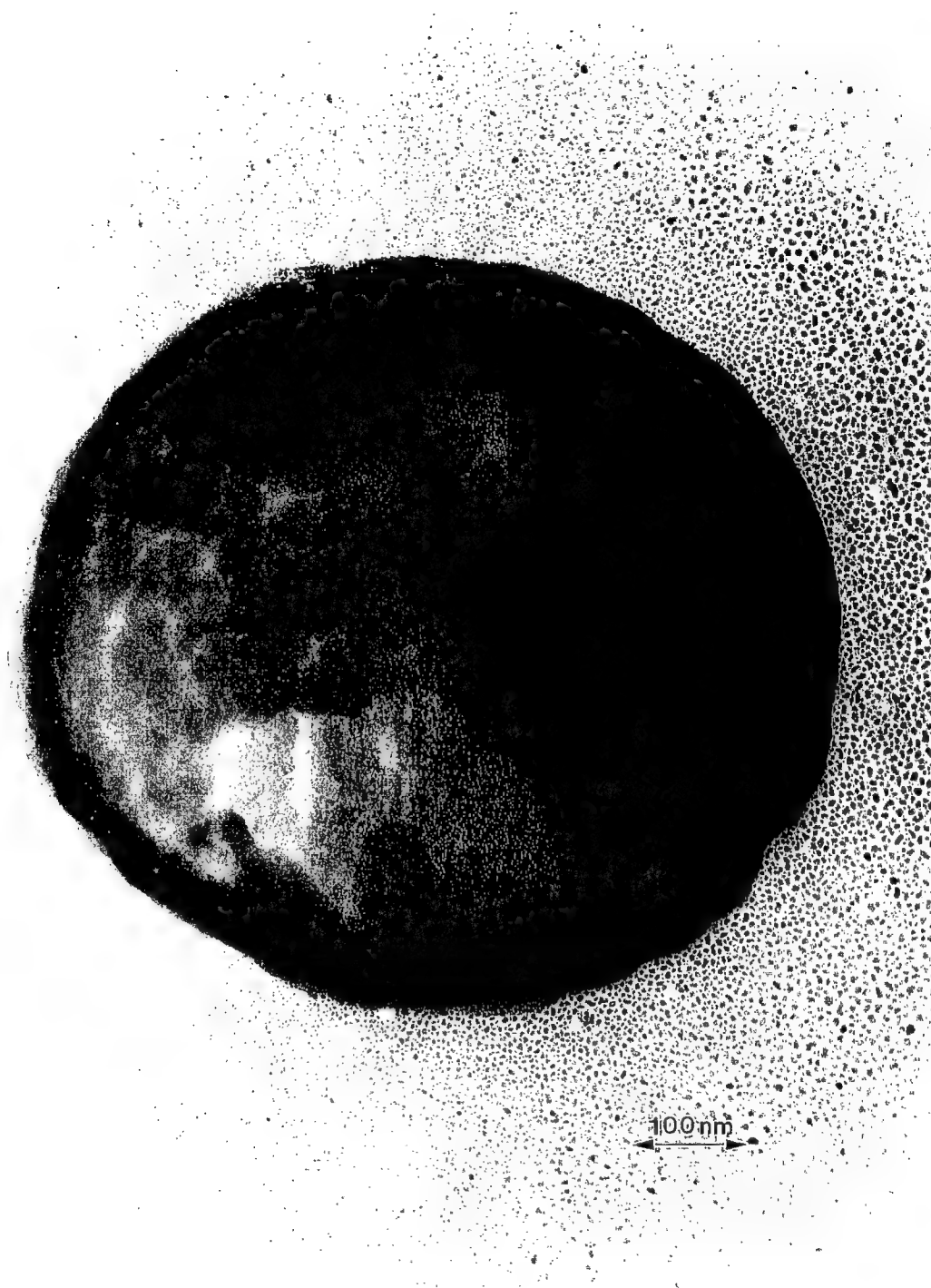


**Figure 3.8:** TEM image of a sphere with the shell thickness apparent. The shell is approximately 70 nm in width.

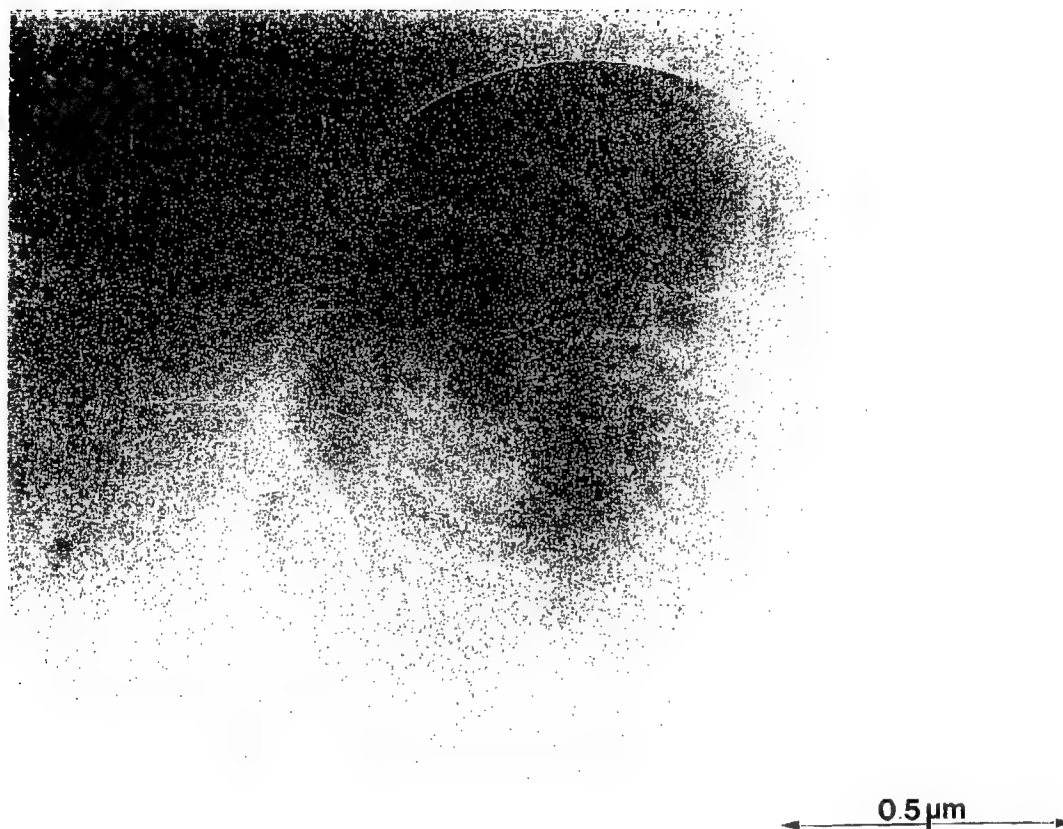


**Figure 3.9: TEM image of a sphere oriented so the axis of the two holes is in the plane of the substrate. The perimeter of both holes appears rough whereas the sides of the sphere are smooth and sharp.**

**Figure 3.10: A representative TEM image of sphere oriented with the hole axis in the plane of the substrate and its corresponding SAED. The SAED shows sets of arcs with an absence of spots corresponding to the hole axis. The arcs correspond to spacings which are 0.83, 0.62, and  $0.41 \pm 0.02$  nm. Similar TEM images also have shown HREM fringes along the side edges corresponding to both 0.8 nm and 1.2 nm fringes. This observation along with the SAED patterns suggest that the spheres are textured with a general orientation of the polymer chain parallel to the hole axis.**



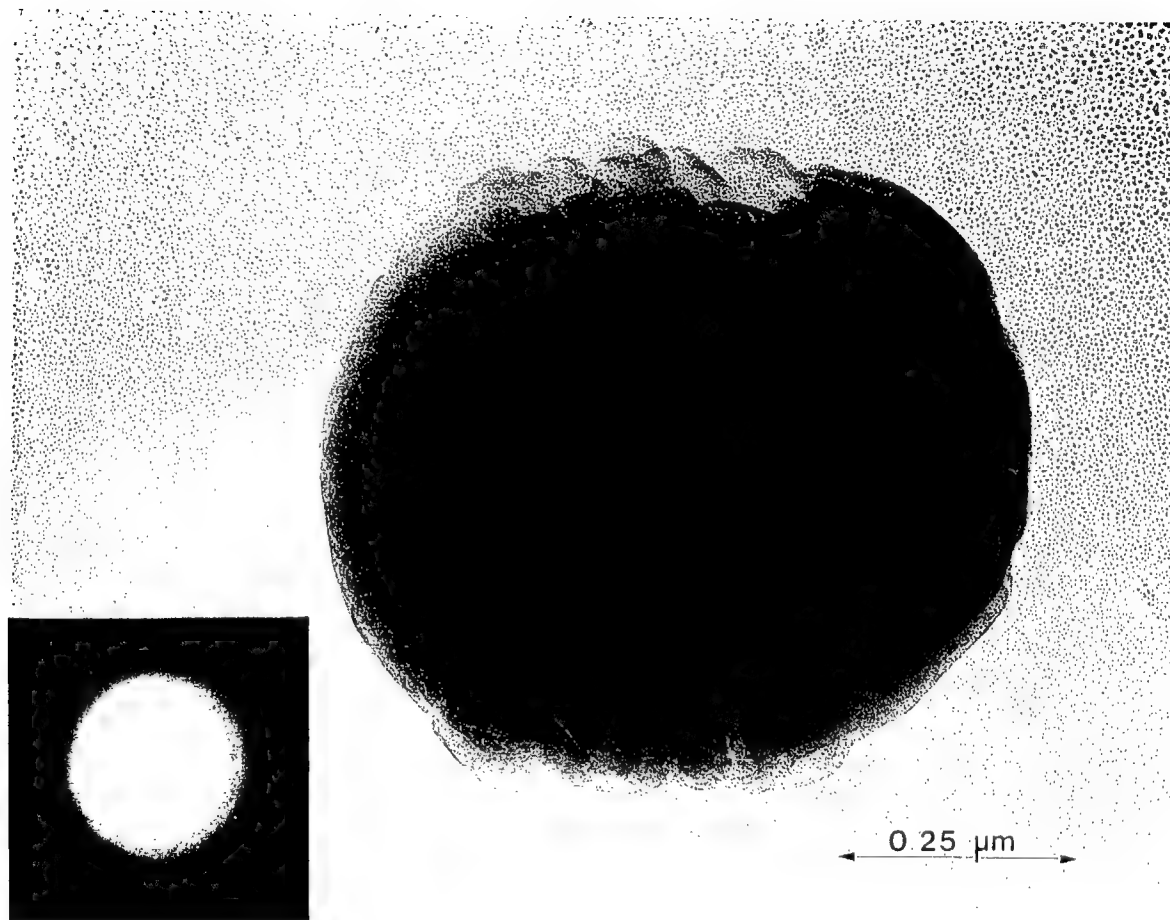


Figure 3.10

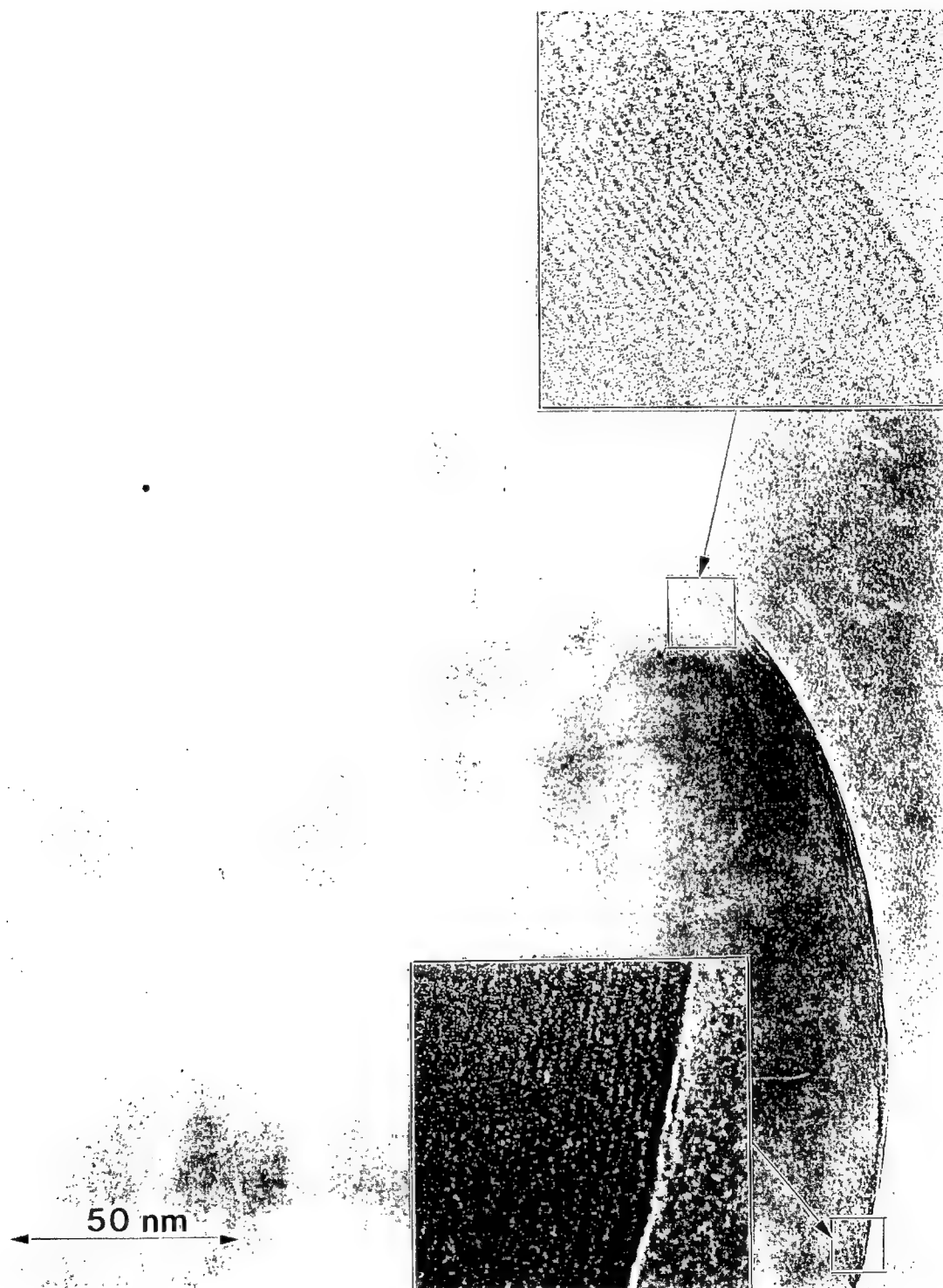


Figure 3.11: TEM image of a sphere with the hole axis in the plane. The hole perimeter is rough in contrast to the sides of the sphere which are sharp. Insets are magnified images of the boxed regions showing 1.2 nm fringes corresponding to the (010) planes. The region between the boxes shows these fringes bending with the same radius of curvature as the surface.

Table 3.1

Spacings from SAED of spheres including their orientation and what possible planes the data may correspond to along with proposed crystallographic texturing.

Sample	Beam Orientation	Spacing	Planes	Calculated Spacing	Calculated Intensity	Forbidden Zones	Possible Zones
1	Hole Parallel	4.1 +/- 0.2	(220)	4.30	100 %	[010]	[001]
			(111)	4.26	78.19%		
			(2-30)	4.21	49.62%		
		8.3 +/- 0.2	(200)	8.26	6.10%	[100]	Textured
			(2-10)	8.13	45.39%		
		6.2 +/- 0.2	(020)	6.11	34.84%		
2	Hole mostly Parallel		(210)	6.02	15.56%	[010]	[001]
		8.4 +/- 0.3	(200)	8.26	6.10%		
			(2-10)	8.13	45.39%		
		6.3 +/- 0.3	(020)	6.11	34.84%	[100]	Textured
			(210)	6.02	15.56%		
		4.1 +/- 0.3	(220)	4.30	100%		
3	Hole mostly Parallel		(111)	4.26	78.19%	[001]	Fiber
			(2-30)	4.21	49.62%		
			(200)	8.26	6.10%		
4	Hole Parallel	13.1 +/- 0.5	(010)	13.56		[001]	Textured
		8.7 +/- 0.5	(200)	8.78		[100]	
		6.7 +/- 0.5	(020)	6.78		[010]	
		6.4 +/- 0.3	(020)	6.11	34.84%	[010]	[100]
		4.1 +/- 0.3	(220)	4.30	100%		
			(111)	4.26	78.19%		
5	Hole Mostly Parallel		(2-30)	4.21	49.62%	[001]	Textured
		3.6 +/- 0.3	(021)	3.82	68.28%		
		3.2 +/- 0.3	(221)	3.24	67.72%		
		4.3 +/- 0.3	(220)	4.30	100%	[001]	Textured
			(111)	4.26	78.19%		
			(2-30)	4.21	49.62%		
6	Mixed		(021)	3.82	68.28%	[100]	[001]
			(4-30)	3.50	31.37%		
		8.3 +/- 0.3	(200)	8.26	6.10%		
			(2-10)	8.13	45.39%	[010]	Textured
		4.2 +/- 0.3	(220)	4.3	100%		
			(111)	4.26	78.19%		
7	Down Hole		(2-30)	4.21	49.62%	[010]	Textured
			(4-10)	4.35	46.86%		
			(4-20)	4.07	28.54%		
		4.4 +/- 0.3	(220)	4.3	100%	[100]	[001]
			(111)	4.26	78.19%		
			(2-30)	4.21	49.62%		
8	Down Hole		(4-10)	4.35	46.86%	[010]	Textured
			(4-20)	4.07	28.54%		
		3.7 +/- 0.3	(021)	3.82	62.28%		
9	Down Hole		(4-30)	3.50	31.37%	[010]	[100]
		8.7 +/- 0.6	(200)	8.26	6.10%	[010]	Textured
			(2-10)	8.13	45.39%		
		8.3 +/- 0.6	(200)	8.26	6.10%		
			(2-10)	8.13	45.39%	[010]	Textured
		Possible 6	(020)	6.11	34.84%		
			(210)	6.02	15.56%		
		4.1 +/-	(220)	4.3	100%	[010]	Textured
			(111)	4.26	78.19%		
			(2-30)	4.21	49.62%		
			(4-10)	4.35	46.86%	[010]	Textured
			(4-20)	4.07	28.54%		

liquid evaporates either in the chamber atmosphere or by the help of a heated gas flow to form spheres which are then collected. The heated gas flow can help suspend large particles that would normally fall before being fully dried. The methods used in this study were designed to conform to this process. The procedure was to investigate the formation of the spheres without any external processing control before changing evaporation rates or other environmental parameters.

As the atomized sphere of solution floats down the column, solvent at the surface evaporates increasing the concentration of DCHD in the surface layer. In this study, the solution used was saturated when atomized. A crystal nucleus would immediately precipitate and grow as more solvent evaporated. In this manner, the crystallization is at the surface and is directly affected by the surface geometry. This can be seen in HREM images of the polymer chains where they are seen to bend with a radius of curvature similar to that of the sphere (Figure 3.11). The crystalline phase that precipitates and grows at the surface is swollen with chloroform. After all the swollen DCHD has precipitated and grown via evaporation of the solvent, the swollen sphere dries. The size of the sphere can constantly become smaller during evaporation and growth because the DCHD shell has mobility due to the trapped solvent. If the diffusion of chloroform to the surface was slower than the evaporation rate, the shell would dry and the lattice structure would be frozen in place. The dried spheres are smaller than the expected atomized solution sphere (based on the volumetric calculations) and since the lattice bending seen in nearly the same radius of curvature of the sphere, reorganization of the lattice must have occurred constantly as the sphere evaporated. Figure 3.12 outlines the proposed evaporation-crystallization scheme as expected from examination of the phase diagram in Figure 3.13.

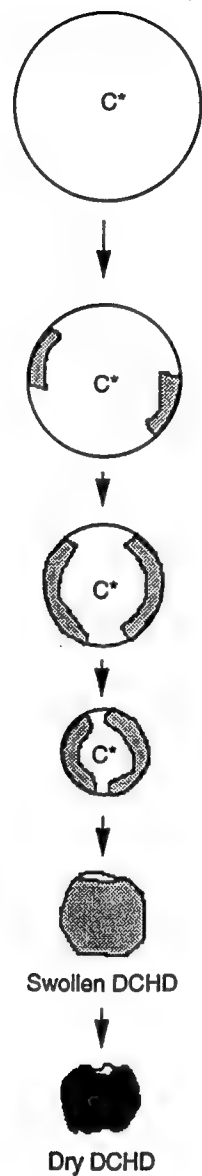


**Figure 3.12:** Schematic of proposed sphere formation which produces the observed holes and texturing. The solution which is atomized is at the solubility limit of DCHD in chloroform (0.434 wt% at room temperature). As the chloroform begins to evaporate at the surface, swollen DCHD precipitates and nucleates in the region at the surface which is depleted of solvent. Continued evaporation and growth forms a shell with possible holes.

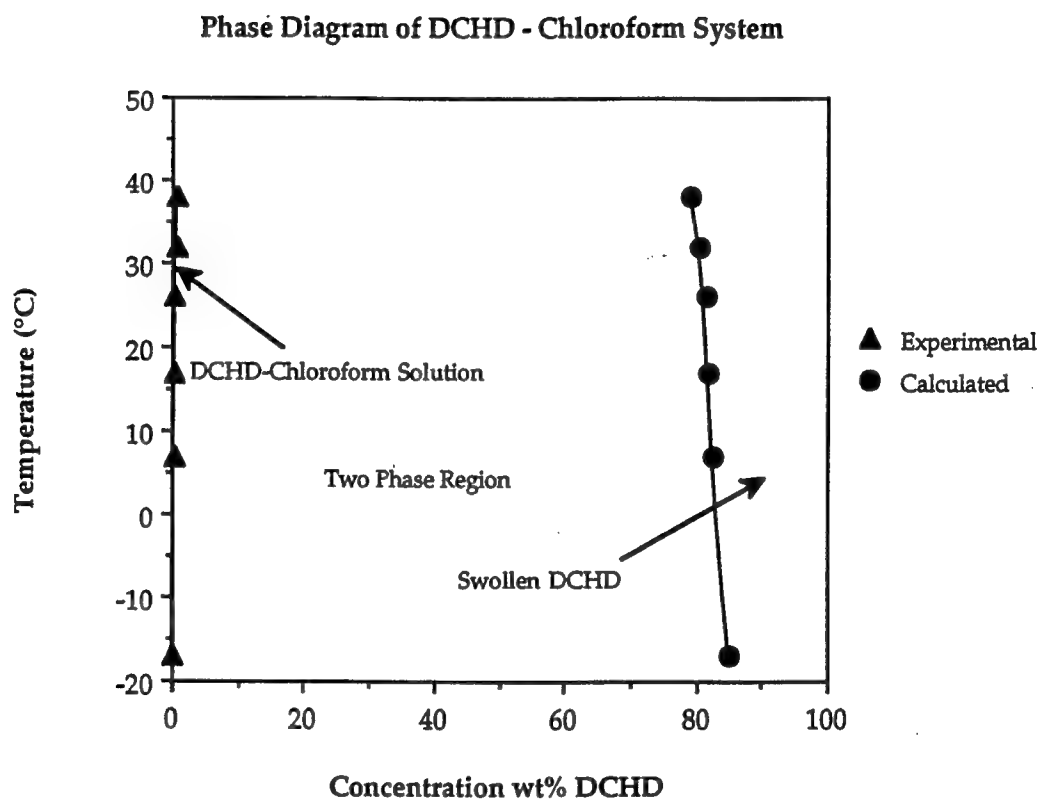


Figure 3.13: Phase diagram for the DCHD - Chloroform system. Solubility data of DCHD in solution was experimentally determined (Liao et al., 1994) and used to calculate the amount of chloroform able to swell DCHD from Flory-Huggins theory (Flory, 1953)

The phase diagram was calculated using the Flory-Huggins theory of polymer-solvent systems (Flory, 1953) from the measured solubility of DCHD in chloroform (Liao et al. 1994). The Flory-Huggins expression for the mixing per lattice site of two components of different sizes is:

$$\frac{\Delta G_m}{RT} = \frac{\phi_a \ln \phi_a}{N_a} + \frac{\phi_b \ln \phi_b}{N_b} + \chi \phi_a \phi_b$$

where  $N_a$  and  $N_b$  are the numbers of "lattice sites" species a and b occupy, respectively and  $\phi_a$  and  $\phi_b$  are the volume fractions. Table 3.2 contains the calculated volume fractions as a function of temperature. From this analysis  $\chi$  was estimated to be approximately 1.9.

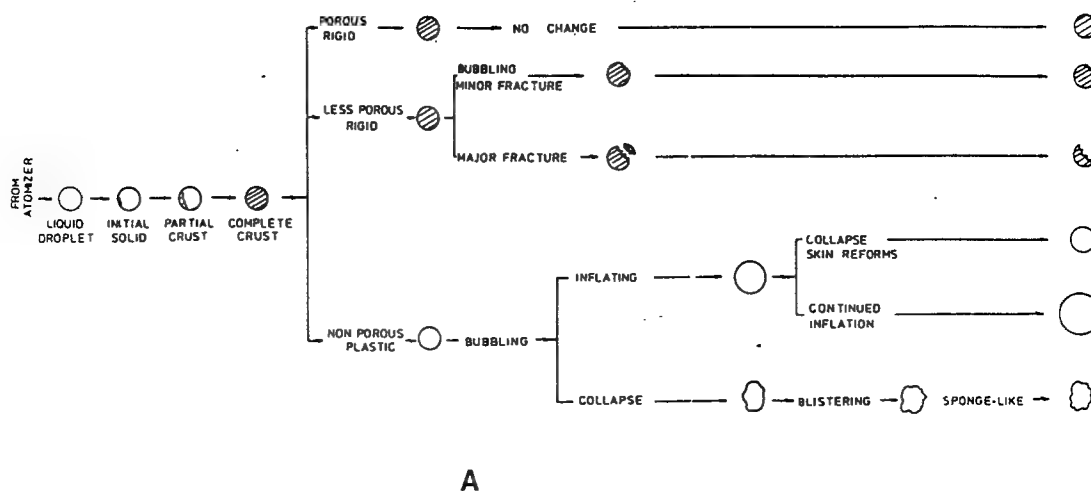
Qualitative information about evaporation versus gross morphology of spheres has been described by Masters (1991) based on work by Charlesworth and Marshall. They classify the shape and texture of the resulting particle as a function of the evaporation gas temperature and the whether the material dries into a rigid or plastic material. These schemes are shown in Figure 3.14. The basis for these mechanisms is the competition of evaporation rate at the surface and diffusion of solvent through the solidifying crust. If the mass transfer drops because of solidification, then the rate of heat transfer can increase the droplet temperature. This rise in temperature can cause vaporization within the droplet and pressure build up. If the crust is rigid, the crust can fracture to release the pressure, if it is plastic then it can bubble creating differing gross morphologies. The formation of holes in the surface of the DCHD spheres may allow the residual solvent to escape after the outer region of the swollen shell is crystallized. Questions arise as to the morphology of the DCHD shell; is it a single crystal, textured, polycrystalline, or amorphous? Figure 3.15 outlines possible

Table 3.2

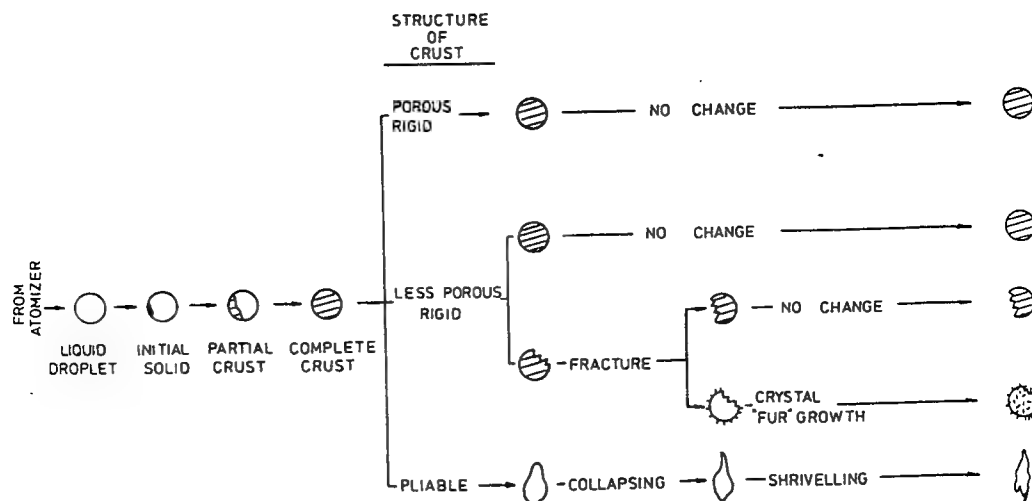
Experimental and calculated volume fractions from Flory-Huggins theory  
(Flory, 1953)

Temperature (°C)	Experimental Volume Fraction (Solvent solubility in dilute phase)	Calculated Volume Fraction (Concentrated phase)
-17	$5.2 \times 10^{-7}$	$2.0 \times 10^{-3}$
7	$2.3 \times 10^{-6}$	$4.3 \times 10^{-3}$
17	$3.3 \times 10^{-6}$	$5.2 \times 10^{-3}$
26	$3.4 \times 10^{-6}$	$5.3 \times 10^{-3}$
32	$5.9 \times 10^{-6}$	$6.9 \times 10^{-3}$
38	$9.4 \times 10^{-6}$	$8.7 \times 10^{-3}$



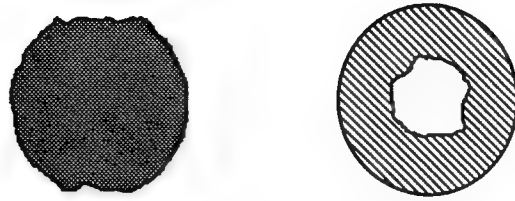


A



B

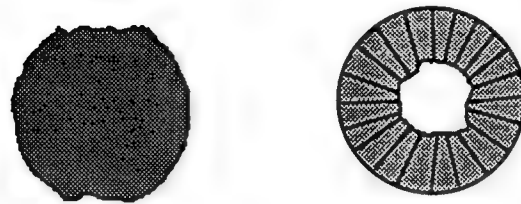
Figure 3.14: a) Characteristics of spheres undergoing drying at gas temperatures above the boiling point. b) the same scheme except at gas temperatures below the boiling point. Both Figures taken from Masters (1991).



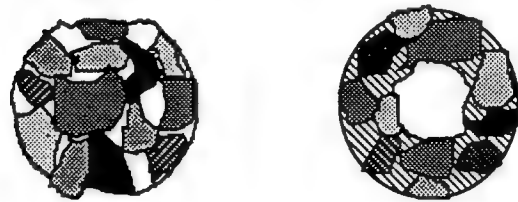
Single Crystal



Droplet Textured (Fiber textured)



Single Texture (all same crystal habit on surface)



Polycrystalline

**Figure 3.15: Some possible crystallographic texturing options for the spheres. Options are shown in projection parallel and perpendicular to the hole axis.**

crystalline texturing either looking perpendicular to the hole axis or parallel to the hole axis. In summary, if the sphere was amorphous then the SAED would appear as a diffuse ring roughly at the molecule to molecule correlation spacing no matter what the orientation of the sphere was. We did not observe this, but rather observed arcs and distinct crystallographic reflections. Table 3.1 summarizes the spacings and orientations of several SAED patterns measured. If the spheres were polycrystalline with a random orientation of the crystallites, the SAED patterns for any sphere orientation would be composed of rings of all spacings. Since there are distinct partial arcs and points in the recorded patterns, a certain degree of texturing is apparent which is evidently not randomly oriented. This also eliminates the possibility that the spheres are single crystalline, since reflections from both the [100] and [010] zones are seen in the same SAED and also in both orientations, looking down the hole and perpendicular to the holes. HREM evidence from several spheres show both 1.2 nm and 0.8 nm fringes at the surface. One such sphere shows fringes corresponding to the chain axis on both sides of the sphere, suggesting that the chain wants to lie parallel to the surface. Previous studies of droplets on surfaces (Wilson and Martin, 1992) using DCHD also showed that the chain preferred to lie parallel to the surface, bending to accommodate the droplet curvature. Since DCHD grows from chloroform as long needle crystals in the [001] direction with the (200) and (010) as habit planes, the preference of the chain to lie on the surface is consistent with energetics of the surfaces. Plausible possibilities for texturing with the chain lying parallel to the surface are for the sphere to be fiber textured or for the same crystal plane to be at the surface, rotated around the sphere. The SAED patterns from these two textures would appear the same. Looking perpendicular to the hole, a fiber pattern would be apparent with

large arcs due to the bending of the lattice seen in the HREM images.

Observation down the hole would show the [001] zone axis with large arcs or rings. SAED evidence looking perpendicular to the holes is consistent with a fiber pattern (Figure 3.10), although SAED from the second orientation are a combination of arcs and spots. The SAED results combined with the HREM observations are consistent with a texturing of the spheres which has most of the chains lying parallel to the surface, running from hole to hole, and a limited degree of fiber texturing. This hypothesis is diagrammed in Figure 3.16.

The high density of defects incorporated in the crystals because of the surface bending account for the diffuseness of the reflections in the SAED patterns. Also, since the spheres have lateral chain invariant grain boundaries (Martin and Thomas, 1991) which are parallel to the chain several zone axis are represented in each SAED pattern, as is evident from the spacing data in table 3.1.

The development of the holes in the spheres may be correlated to their crystallographic texturing. DCHD is known to prefer to crystallize into long needles with the (200) and (010) surfaces on the sides and the (001) surface at the ends, inferred from this is that the chain end surface is of higher energy and the crystal wants to minimize its area. A reasonable assumption might be that the crystallization in the sphere would want to minimize the chain end surface area. This tendency was also seen in the similar crystallization of DCHD in droplets on a substrate. The resulting droplets had a fiber symmetry with the chain in the plane of the substrate. At the edges, the chains bent to accommodate the surface and to minimize the area of chain ends.

As before the bending of the thin crystal shell should be mediated by dislocations. The density of dislocations needed to bend the shell can be

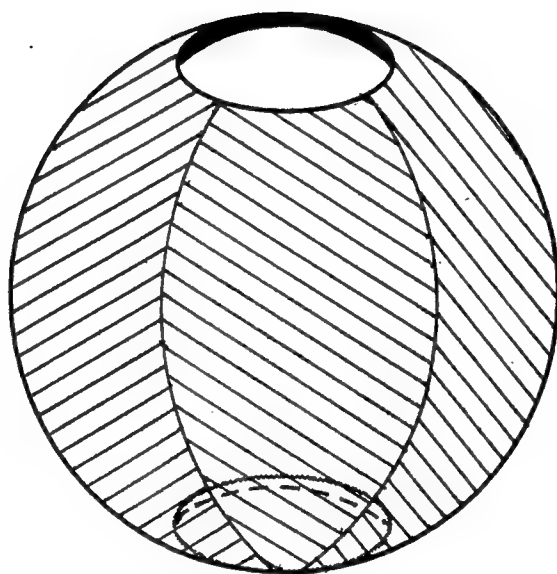


**Figure 3.16:** Schematic showing proposed idealized structure and texturing of spheres formed via the mechanism and processes outlined in the text based on the experimental data.

roughly estimated as  $1/rb$ , where  $r$  is the radius of curvature of the shell and  $b$  is the Burger's vector. HREM results show the chain parallel to the surface which would require the Burger's vector to be equal to 0.49 nm in the [001] direction. For spheres from 0.1 to 1.3 microns in diameter, maximum dislocation densities caused by curvature would be  $4 \times 10^{16}$  to  $3 \times 10^{15} \text{ m}^{-2}$ , respectively. Recently, Srolovitz et al. (1994) have formulated expressions for the total bending energy of covalently bonded fullerenes to explain the different morphologies seen in nested fullerenes. Their analysis showed that there is a critical thickness or curvature above which dislocations will spontaneously form to reduce the energy required to uniformly curve the lattice. They also showed that if the kinetics of the system allowed it, grain boundaries would form to further reduce the total bending energy.

The total bending energy is comprised of the partially relaxed energy required to bend the lattice and the elastic strain energy of the dislocations. Srolovitz's analysis using isotropic elasticity predicts that the critical radius of curvature is:

$$\frac{1}{r_c} = \kappa_c = \frac{3}{2\pi(1-\frac{a}{h})} \frac{b}{h^2} \ln\left(\frac{h}{r_o}\right)$$

where  $b$  is the Burger's vector of the dislocation,  $r_o$  is the dislocation core cut off,  $h$  is the film thickness, and  $a$  is the molecular layer thickness. This analysis predicts that above a radius of 87 nm (at a 70 nm shell thickness) no dislocations would be generated to reduce the bending energy in poly(DCHD) spheres. Because of the covalent bonding along the chain axis and weak van der Waals forces between chains, this system is highly anisotropic. The critical radius based on isotropic theory does not take into account the

bending energy of the covalent bonds, and as such may not be appropriate. Their derivation for anisotropic elasticity assumes a two dimensional covalently bonded plane unlike our one-dimensional bonding of the polymer and so their derivations of bending energies are not applicable for our situation. The equation for critical curvature is modified by a factor  $K/k$  where  $K$  is the energy factor from anisotropy elasticity and  $k$  is an elastic bending modulus.  $k$  measures the resistance of the system to bending with a non-zero mean curvature.  $k$  will be high in our polymer system, while  $K$  is found to be small when the dislocation Burger's vector is in the covalently bonded direction. This serves to reduce the critical curvature, or increase the radius of curvature, over the isotropic solution where spontaneous formation of dislocations will occur.

Future work could use the analysis by Srolovitz et al. to formulate the bending energy relationships based on the symmetry of the DCHD polymer system. This work could be expanded on to analyze the role of processing conditions needed to form various curvatures or thicknesses which would give control over the dislocations formed by bending the lattice in spherical or other boundary conditions.

## Conclusions

Hollow spheres of DCHD were produced by the evaporation of atomized solution in a tower under atmospheric conditions. Crystallization occurred at the surface of the spheres and followed the curvature of the surface, inducing two holes to form predominately directly across from each other. Observations of the surface showed a sharp, smooth surface in the bulk of the sphere with rough edges emanating near the holes. Preliminary results suggested that the overall chain orientation is from hole to hole.

## CHAPTER IV

### DIRECT IMAGING OF RELAXATIONS NEAR DISLOCATIONS IN POLYDIACETYLENE

#### Introduction

Defects in polymer materials have been studied, mainly in lamellar crystals, for the past twenty years. New interest has been generated in polymer defects due to the development of linear conjugated polymers which exhibit conductive properties that make them attractive for polymer device fabrication. Limitations in the performance of these polymer devices are expected due to the inclusion of certain defects, such as chain ends, in the crystal structure (Hone and Singh, 1992). The relationships between defects and macroscopic properties have not been as fully explored in polymers as in other material systems. An important first step in this process is to characterize the local relaxation around defects which are expected to dominate property relationships.

Here we will look at the nature of the distortion in highly anisotropic polymer materials. We might expect that as a material becomes more anisotropic due to covalent bonding along one direction, the correlations between chains would be weakened. Furthermore, we want to compare this with a related material, columnar liquid crystals, where symmetry dictates that there are no correlations between the columns.



Wunderlich (1973) developed a classification scheme to encompass the types of defects which could be found in polymeric materials. He postulated that all macromolecular defects are included in nine classifications. These classifications could be further divided into the familiar headings used to describe metallurgical defects, which take into account the dimensionality of the defect. Extra defects, such as point defects along the chain attributed to Reneker (1962, 1983), arise from the inclusion of covalent bonding in polymers. He also stressed the necessity of understanding the relationships of structure-sensitive macroscopic properties.

Properties such as conduction along a delocalized backbone and mechanical strength should be limited by those defects which interrupt the covalent bonding of the chain. Chain end point defects, chain end dislocations (both edge and screw type), and grain boundaries which cross the covalent bonding plane (ACI and ACR by the classification scheme of Martin and Thomas, 1991) can all disrupt chain conductivity. Dislocations are agglomerations of point defects, and grain boundaries are arrays of dislocations. Predecki and Statton (1966) showed in nylon 66 that the random inclusion of chain ends (predicted from molecular weight distribution) would result in a structure too disordered to explain X-ray data. They postulated that the energy of the lattice would decrease by the migration of chain ends to form dislocations, which would also explain scattering effects seen from X-ray diffraction. Dislocations formed from chain ends have not been studied in detail since most work has been accomplished in semi-crystalline polymers. Lamella deposit with the chain axis perpendicular to the substrate. Consequently, studies using electron microscopy are limited because the chain is parallel to the incident beam. Polydiacetylenes commonly deposit with the chain axis in the plane of the substrate and have yielded images of

chain end edge dislocations (Read and Young, 1984 and Wilson and Martin, 1992).

Chain end dislocations could affect conductive properties due to the disruption of the conjugation path. Relaxations of the structure around the dislocation, evident in the bending of the chain, could also change the electronic structure of the local region. This study intends to measure the strain field around chain end edge dislocations in polydiacetylenes in order to help predict structure-property relationships. Polydiacetylenes are a good system for studying dislocations because they are formed from a solid state topochemical reaction of the monomer crystal yielding a polymer single crystal. Young and Petermann (1982) observed dislocation images in poly(toluene sulphonate) diacetylene. They postulated that dislocations are present in the monomer crystal and are thus preserved in the polymer structure after polymerization.

Local structure can be imaged using high resolution electron microscopy (HREM). Advances by several groups (Martin, 1990, Voigt-Martin, 1992, Zhang and Thomas, 1992, Liao and Martin, 1993) to limit the amount of radiation damage during imaging and maximization of the information content have paved the way for advanced studies of polymers using this technique.

Recently work has been executed to extract strain field information from high resolution images of dislocations in silicon (Tsai 1992, Choi 1992). The procedure, Computational Fourier Transform Deformation analysis, was to extract the Moiré pattern from a digitized HREM image by filtering the optical diffractogram and calculating the inverse Fourier transform. The Moiré pattern was then algebraically manipulated to derive the displacement gradient from which the strain fields were calculated. The full analysis has

yet to be published although the calculated strain fields (from a model defect image) resemble the predictions from linear isotropic elasticity theory. This work fails to take artifacts due to filtering the defect image into account. Pradere and Thomas (1990) showed that by changing the size of the window used to filter a dislocation image in polyparaxylylene, drastically different images could be produced in which the defect information could vanish or bending of the associated defect planes was increased. A method that does not depend on filtration of the data is desired because of problems known to exist in extracting defect information from periodic filtration means.

A measurable quantity from HREM images is the local tilt of the polymer chain, represented by a fringe under the imaging conditions used in this paper. It will be shown that the tilt is related to the shear strain field around the dislocation. The shear strain field of chain end edge dislocations will be examined and compared to available theories for the deformation around dislocations. Strain fields for dislocations in metals are commonly modeled using isotropic linear elastic dislocation theory. Polymers exhibit a high anisotropy of their crystalline moduli due to the one-dimensional covalent bonding and relatively weak van der Waals or hydrogen bonding between chains. The applicability of isotropic elasticity to polymers is therefore questionable. A better approach is to use the more rigorous development for anisotropic materials (Steeds, 1973). Peterson and Lindenmeyer (1966) recognized the need to analyze screw dislocations in orthorhombic polyethylene using anisotropic theory. Their analysis of the contrast of dislocation images using two-beam electron imaging provided them with an estimate of the anisotropy of the elastic stiffness moduli,  $C_{66}$  and  $C_{55}$ . Their study relied on the kinematic prediction of the extinction thickness in polyethylene as a parameter to match the anisotropy to the

contrast. Research presented in Chapter VI of this dissertation will show that this is an unreliable prediction.

Liquid crystalline materials also exhibit dislocations in both layered and rod like structures. A chain end edge dislocation with a Burger's vector perpendicular to the chain in an anisotropic polymer is analogous to a transverse dislocation in a columnar liquid crystal. A columnar phase has two-dimensional positional order in the transverse direction but no correlations along the column resulting in no axial correlations (DeGennes and Prost, 1993). In a polymer crystal the high anisotropy of the chain modulus to the transverse modulus reduces the correlations between chains. It will be shown in this paper that as the anisotropy of the moduli is increased, the strain around a polymer chain end edge dislocation as predicted by linear elasticity takes on characteristics of the columnar liquid crystal solution.

## Experimental

### Analysis of Dislocation Images

Images of chain end dislocations in diacetylenes were obtained by the methods outlined in Chapter II (Wilson and Martin, 1992). HREM images were taken at Gaussian defocus (-11 nm). The 0.8 nm fringe periodicity was determined to be the (200) planes from knowledge of the sample orientation and subsequent multislice image simulations. The fringes are parallel to the chain axis and each fringe arises from a single stack of polymer chains. Determining the character of deformation was done by mapping the molecular director around the dislocation. In this case the molecular director also corresponds to the local normal of the chain. The directors were

determined starting from the center of the dislocation plane (along the extra half plane) and mapped at equal distances along the plane. The director to a chain would indicate the point along the next chain where the next director would be drawn.

The distortion around a dislocation in a calibrated image was quantified by measuring the tilt of the HREM lattice fringe at a radius of five Burger's vectors from the origin of the dislocation. The measured tilt was relative to the chain axis of a perfect crystal, defining  $\theta=0$ .

### Modulus Calculations

Full elastic compliance and stiffness matrices were needed for DCHD in order to predict the anisotropic behavior of the strain field. Moduli were calculated using the elastica module of Polygraf (Molecular Simulations, 1993). The procedure was to minimize the energy of the X-ray unit cell of DCHD monomer (Enkelmann et al., 1977) and polymer (Apgar and Yee, 1978) to a RMS value of 0.01 by conjugate-gradient methods using the Dreiding II force field. The minimized unit cell energies were 84.26 kcal/mol and 152.97 kcal/mol respectively. Polygraf calculates the stiffness matrix,  $c_{ij}$ , from the second derivative of the energy expression,  $U$ , by:

$$c_{ij} = \frac{\partial^2 U}{\partial \epsilon_i \partial \epsilon_j}$$

where  $\epsilon$  is the strain. The compliance matrix is calculated as the inverse of the stiffness matrix. Young's modulus values and isotropic Lamé constants,  $\lambda$  and  $\mu$ , are calculated (Molecular Simulations, Inc., 1992) as follows:

$$E_x = \frac{1}{s_{11}} \quad E_y = \frac{1}{s_{22}} \quad E_z = \frac{1}{s_{33}}$$

$$\lambda = \frac{1}{3}[c_{11} + c_{22} + c_{33}] - \frac{2}{3}[c_{44} + c_{55} + c_{66}]$$

$$\mu = \frac{1}{3}[c_{44} + c_{55} + c_{66}]$$

All modulus values are calculated in reference to the crystal unit cell axes. The compliances, Young's moduli and Lamé constants for both monomer and polymer DCHD are shown in Table 4.1. Due to symmetry, monoclinic elastic matrices have only 13 independent constants with all other values being zero (Nye, 1957). The calculation by Polygraf correctly predicted the placement of the zeros to two significant digits both with and without the symmetry constraints available in the software.

### Theories of Distortions Around Dislocations

#### Isotropic Linear Elastic Dislocation Theory

The foundation of linear elastic dislocation theory is the assumption that the material obeys Hooke's Law which states that there is a reversible linear relationship between stress and strain on a material:

$$\sigma_{ij} = c_{ijkl} \epsilon_{kl}$$

Normally, polymers exhibit non-linear behavior, but in extended chain polymer crystals Hooke's law might be obeyed at small strains. Isotropic

theory assumes that the properties in all directions of the material are the same. This simplifies the elastic stiffness matrix considerably and allows for easy solution of the governing equations. Isotropic theory is the simplest to derive, and will be used to illustrate a few generalities.

A dislocation is defined in terms of its Burger's vector and the dislocation line. The closure failure of a Burger's circuit around the defect when compared to the same circuit in perfect material defines the magnitude and direction of the Burger's vector. When the Burger's vector is perpendicular to the dislocation line, it is an edge dislocation. An edge dislocation can often be described as an extra half plane inserted into a crystal if the distortion is localized. In the case where the Burger's vector is perpendicular to the chain axis of a polymer crystal, this would result in a plane of chain ends incorporated into the crystal structure. The strain fields around the dislocation are determined by assuming a set of displacements,  $u$  and  $v$ , that satisfy the equations of equilibrium and compatibility along with boundary conditions. The strains are then calculated by taking the derivatives of the displacements and the stresses are found from the strains from Hooke's law.

The equations of equilibrium state that there are no net forces acting on the body when the dislocation is present. They are formulated from the force-mass-acceleration relationship:

$$0 = \rho \frac{\partial^2 u_i}{\partial t^2} = \frac{\partial \sigma_{ij}}{\partial x_j}$$

Table 4.1

## Elastic modulus determination by molecular mechanics simulations

Monomer					
<u>Elastic Stiffness Constants: <math>c_{ij}</math> (Gpa)</u>					
11.6	11.3	8.9	0	0	0.4
11.3	15.4	11.3	0	0	0.6
8.9	11.3	11.8	0	0	1.1
0	0	0	4.8	2.1	0
0	0	0	2.1	3.3	0
0.4	0.6	1.1	0	0	6.9

Young's Modulus

X 3.2

Y 3.1

Z 3.4

Lamé Constants (GPa) $\lambda$ : 2.9 $\mu$ : 5.0**Polymer**Elastic Stiffness Constants:  $c_{ij}$  (Gpa)

20.2	11.8	9.6	0	0	-2.7
11.8	13.5	12.9	0	0	4.2
9.6	12.9	81.7	0	0	6.2
0	0	0	11.9	8.7	0
0	0	0	8.7	13.0	0
-2.7	4.2	6.2	0	0	6.2

Young's Modulus

X 1.5

Y 0.9

Z 67.5

Lamé Constants (GPa) $\lambda$ : 17.7 $\mu$ : 10.4



Since the body is at rest, the acceleration term is zero. The compatibility equations relate the six strain components, since they are all derived from the three displacements. These equations are:

$$\frac{\partial^2 \epsilon_{ii}}{\partial x_j^2} + \frac{\partial^2 \epsilon_{jj}}{\partial x_i^2} = \frac{\partial^2 \epsilon_{ij}}{\partial x_i \partial x_j}$$

The tilt of the unit cell is the shear strain in the plane. Figure 4.1 illustrates the tilt of a unit cell in terms of the strain.

The shear around a edge dislocation in a isotropic medium is given by (Hull and Bacon, 1984):

$$\epsilon_{xy} = \frac{b}{2\pi(1-\nu)} \frac{x(x^2 - y^2)}{(x^2 + y^2)^2}$$

where  $b$  is the Burger's vector and  $\nu$  is the Poisson's ratio. The Poisson's ratio is related to the Lamé constants by:

$$\nu = \frac{\lambda}{2(\mu + \lambda)}$$

The shear strain field of an edge dislocation is shown in Figure 4.2. The tilt can be plotted as a function of angular position around the dislocation at a constant radius. The dislocation is oriented so that the Burger's vector is parallel to the x-axis, in this case the extra plane of chains lie along the positive y-axis. The tilt is plotted from the x-axis of the dislocation strain field around 180° and then reverses and plots it to -180°. Examination of the strain field and tilt plots show that the tilt is highest along the Burger's vector direction and undergoes a reversal of tilt at  $\pm 45^\circ$ ,  $90^\circ$ , and  $135^\circ$ . The shear

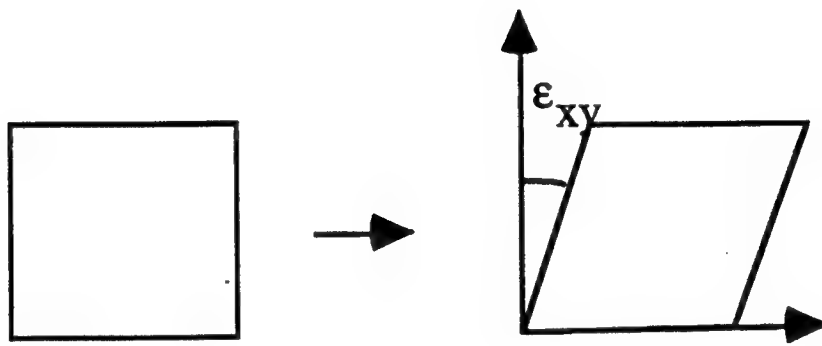
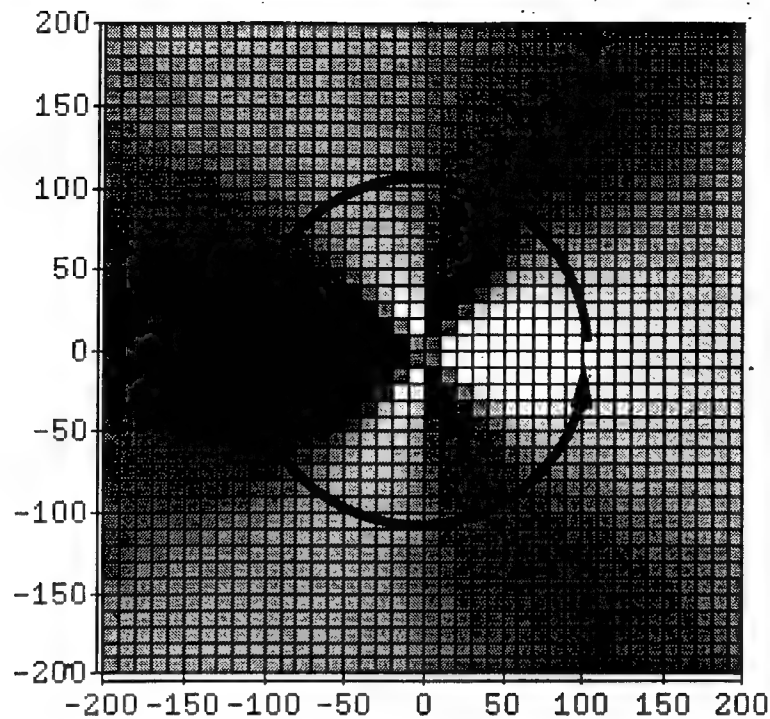
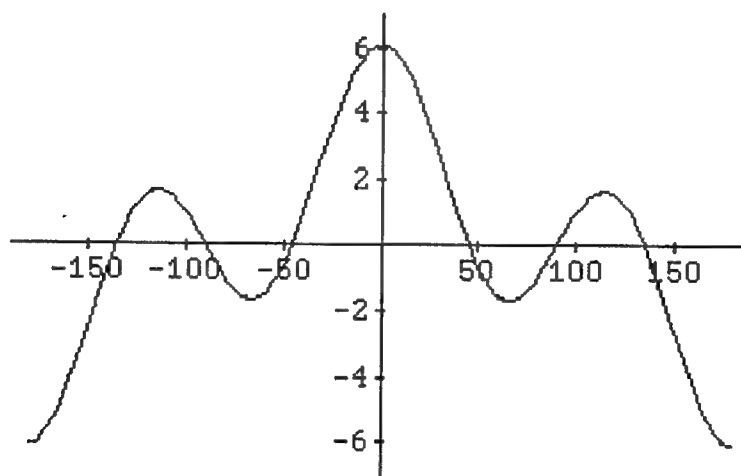


**Figure 4.1** Shear of a unit cell in the  $xy$  plane results in a tilt distortion equal to the shear.



**A**



**B**

Figure 4.2: (a) is the shear strain around a isotropic edge dislocation where the extra half plane is oriented along the positive y axis. If the tilt is plotted by making a trace around the dislocation core as shown, (b) is produced. The large lobes with maximums at  $0^\circ$  and  $180^\circ$  are produced by the tilt of the layers incorporating the extra planes. The smaller lobes are the effect of shear in the x direction between individual repeat units along the y direction.

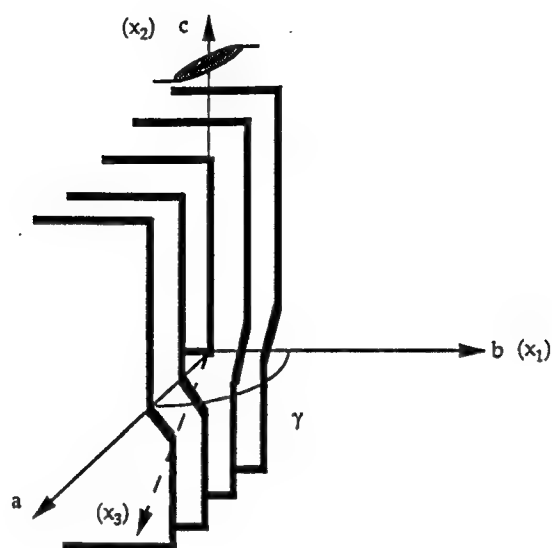
deformation of columns parallel to  $z$  represent the values of the compliances  $c_{44}$  and  $c_{55}$ . This is the main characteristic we will be focusing on when analyzing the behavior of polymer dislocations.

### **Anisotropic Linear Elastic Dislocation Theory**

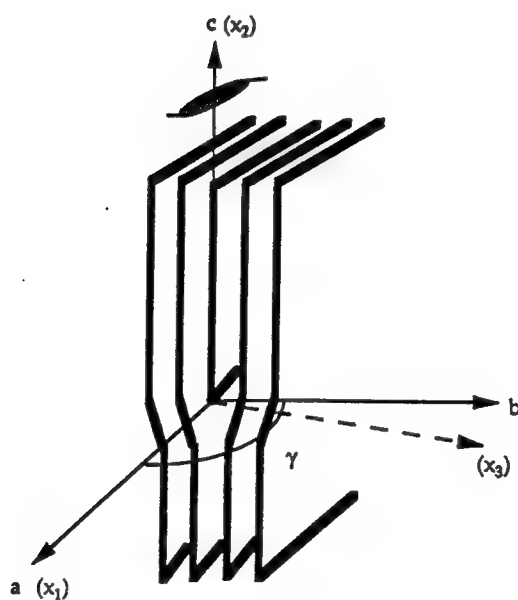
Anisotropic linear elastic dislocation theory has been described by Steeds (1973). The solution of the stress-strain fields involves using only the compatibility equation method of solution. The boundary conditions for an infinite elastic medium results in a sextic equation for which the solution for the roots comprises the essential problem in anisotropic theory. For cases of high symmetry, analytic solutions are available. The symmetry of chain end edge dislocations in DCHD conforms to one of the most widely used solutions. The configuration of the two types of chain end dislocations possible in DHCD are shown in Figure 4.3. Both have the dislocation line perpendicular to a diad axis of symmetry in the crystal. This solution also applies to many of the industrially important dislocation slip systems in cubic materials. Appendix 4.1 describes the process and calculations necessary to derive the tilt of the unit cell (shear strain) from the monoclinic stiffness matrix for both monomer and polymer.

### **Liquid Crystal Dislocation Theory**

Liquid crystal theory (DeGennes and Prost, 1993 and Kléman and Oswald, 1982) derives the distortion of the columns around a edge dislocation in terms of a perturbation length,  $\lambda_3$ .  $\lambda_3$  is a characteristic length, defined as the square root of the bend modulus over a combination of two elastic moduli for columnar phases.



A



B

Figure 4.3: Orientations of the two types of chain end edge dislocations in poly(DCHD). The  $a$ ,  $b$ ,  $c$ , axis refer to the unit cell axis system, whereas the  $x_1$ ,  $x_2$ ,  $x_3$  are the orthogonal dislocation coordinate system required for strain field calculations using anisotropic dislocation theory (Steeds, 1973). The diad axis of the space group ( $P2_1/c$ ) is along the  $c$ -axis and perpendicular to the dislocation lines. (a) shows the orientation for the experimental three chain end edge dislocation analyzed in the text.

$$\lambda_3 = \sqrt{\frac{K_3}{B+C}}$$

where  $K_3$  is the splay modulus (energy/length) and  $B$  and  $C$  are bulk moduli (energy/length<sup>3</sup>).

Two types of edge dislocation are present in columnar systems, a transverse and a longitudinal dislocation. The transverse case occurs when the dislocation line is perpendicular to the column axis, whereas in the longitudinal case they are parallel. The transverse case shown in Figure 4.4 is analogous to chain end dislocations.

The Burger's vector of a liquid crystal dislocation is defined as the integral of the local normal to the layers,  $n$ , around the dislocation core. As long as the path encompasses the core, the result is independent of the contour chosen. The distortion around the extra half plane of columns is separated into the tilt of the layers and the dilation of the layers. The dilation of the layers, formulated by minimizing the free energy density of the material, is:

$$M_x = \frac{-xna_o}{8\sqrt{\pi\lambda_3}\sqrt[3]{|x|}} \exp(-y^2/4\lambda_3|x|)$$

where  $n$  is the strength of the Burger's vector and  $a_o$  is the layer thickness in the undistorted material. The tilt of the layers is the parameter we are interested in:

$$M_y = \frac{\pm na_o}{4\sqrt{\pi\lambda_3}\sqrt[3]{|x|}} \exp(-y^2/4\lambda_3|x|)$$

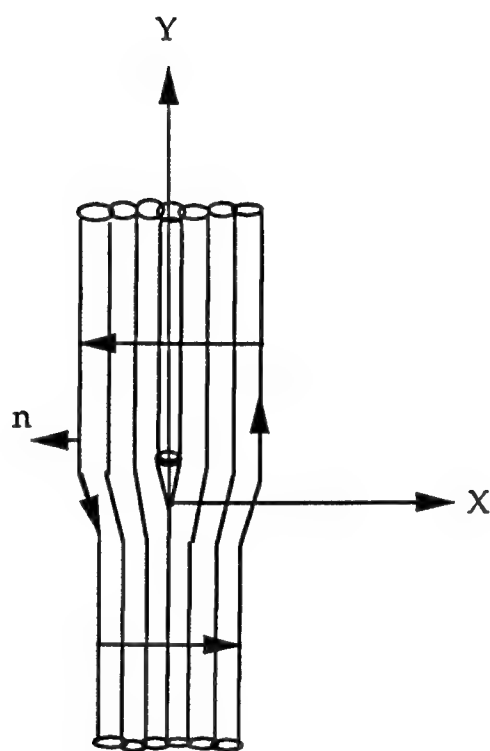


Figure 4.4: Transverse edge dislocation in a columnar liquid crystal. A Burger's circuit is shown which results in a strength of +1 (DeGennes, 1993).

where the angle of tilt is defined as the arcsin of the tilt vector,  $M_y$ .

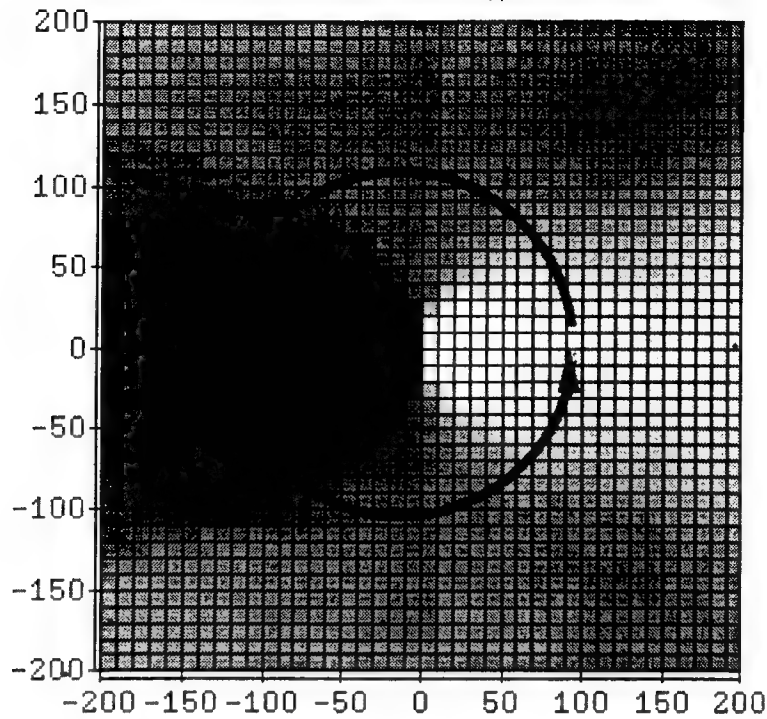
$$\theta_{tilt} = \arcsin(M_y)$$

The distortions are both confined to parabolas along the x-axis defined by  $y^2=4\lambda x$  and decrease as rapidly along y. This distortion is shown in Figure 4.5 along with the corresponding tilt diagram. Unlike the isotropic solution for the tilt, the small lobes which represent inter column shear are not present in the liquid crystal solution. This is because there are no correlations within or between columns.

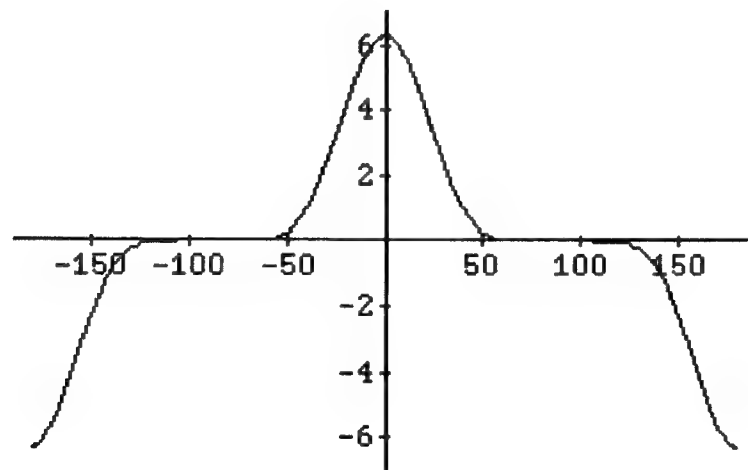
### Results and Discussion

Figure 4.6 is a HREM image of a DCHD three chain end edge dislocation with a Burger's vector of  $3a/2$  [100]. The fringes are 0.8 nm in spacing, corresponding to the [100] planes. By plotting the normal to the fringes, the bend or splay character of the distortion can be determined. Figure 4.7 is a map of the molecular director for Figure 4.6. The uniform bending of the normal can be interpreted as a splay of the molecules to accommodate the extra plane. This is consistent with the expectation that the high tensile modulus of the chain would resist bending. The same information can be quantified by measuring the local tilt of the chains. The tilt at a radius of  $5b$  was measured around the dislocation and is shown in Figure 4.8. The procedure was to measure the local tilt of the layer away from its perfect orientation at a constant radius around the dislocation core. Hudson et al. (1993) have mapped the orientation of the director around a disclination core using a fast Fourier transform (FFT) technique. They used a small window for the FFT to determine the local orientation of the director. This technique could not be used to analyze our data because of the small





A



B

Figure 4.5: (a) is the shear strain around a columnar liquid crystal edge dislocation where the extra half plane is oriented along the positive y axis. If the tilt is plotted by making a trace around the dislocation core as shown, (b) is produced. The large lobes with maximums at  $0^\circ$  and  $180^\circ$  are produced by the tilt of the layers incorporating the extra planes. Notice the lack of small lobes as seen in the isotropic elasticity case. Because there are no correlations along the column in a liquid crystal the effect of shear is suppressed.

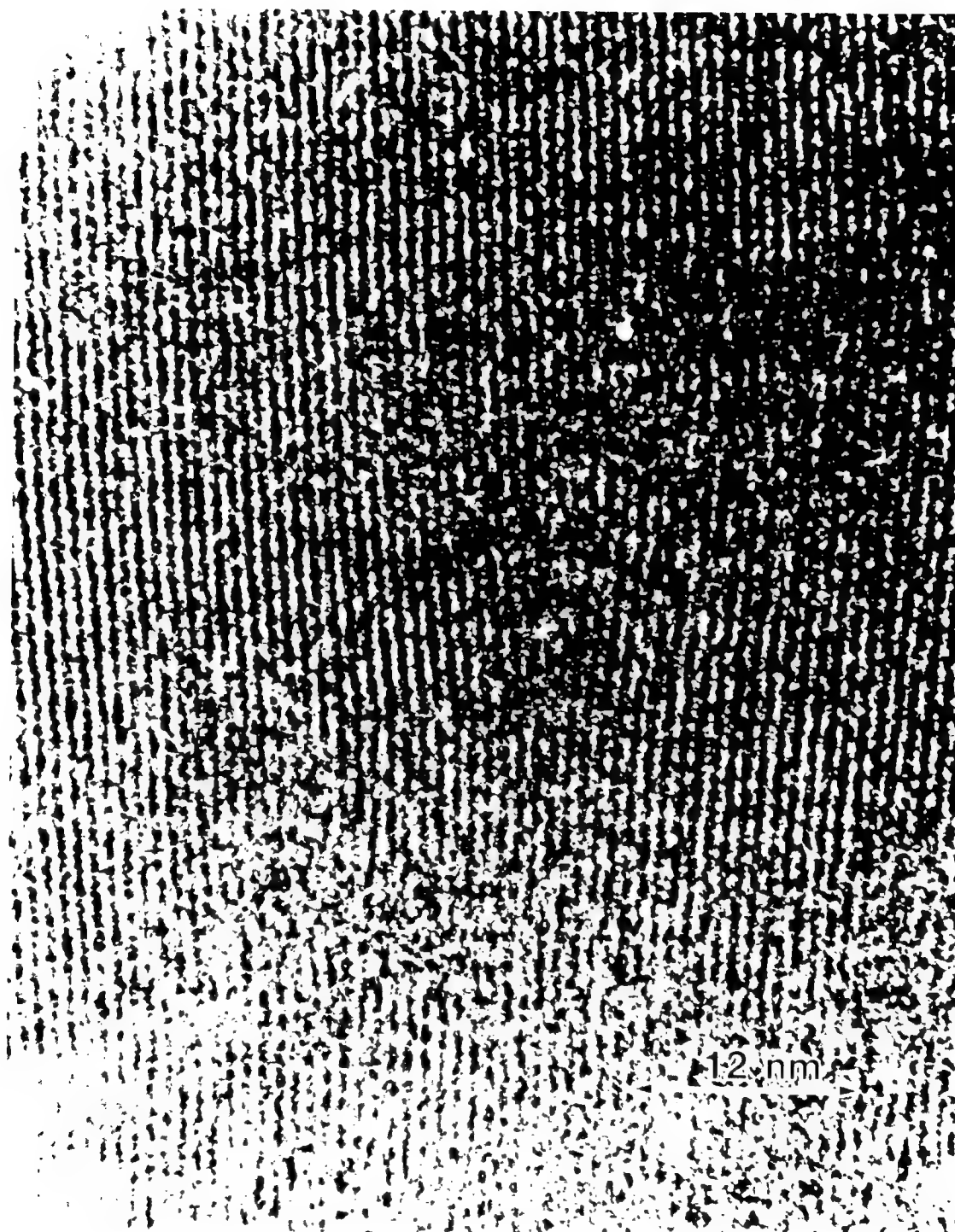
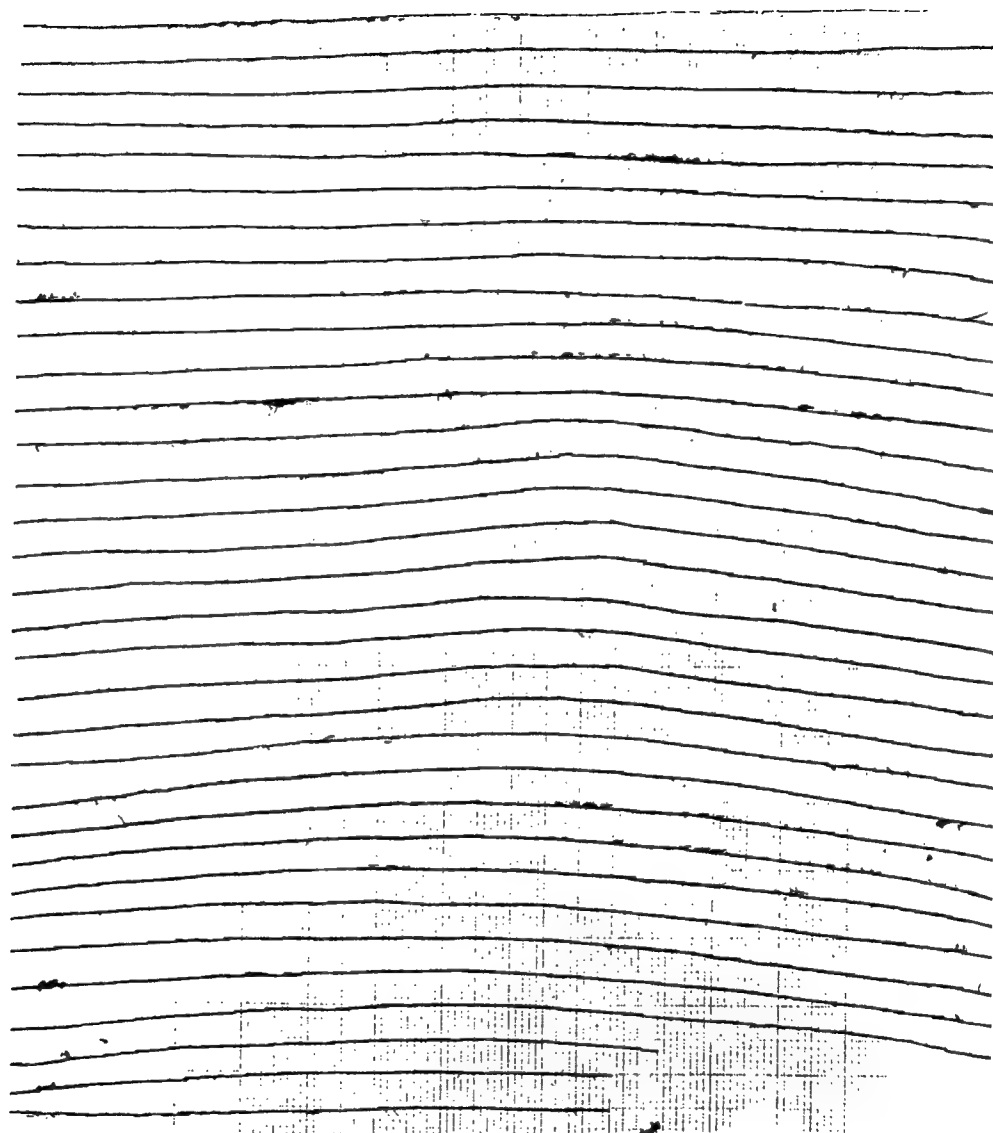
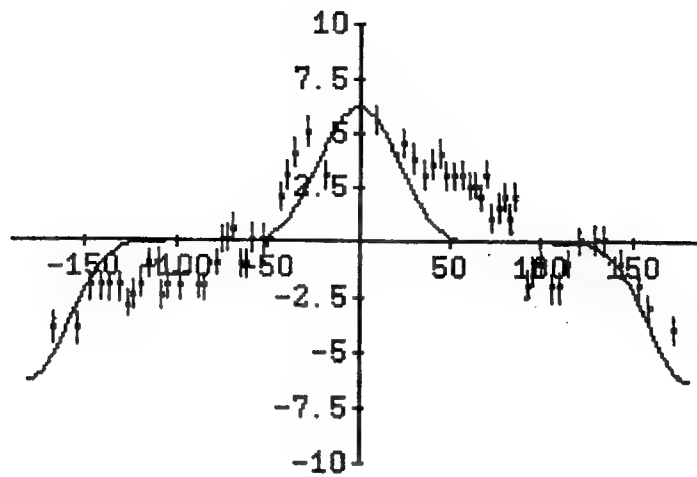


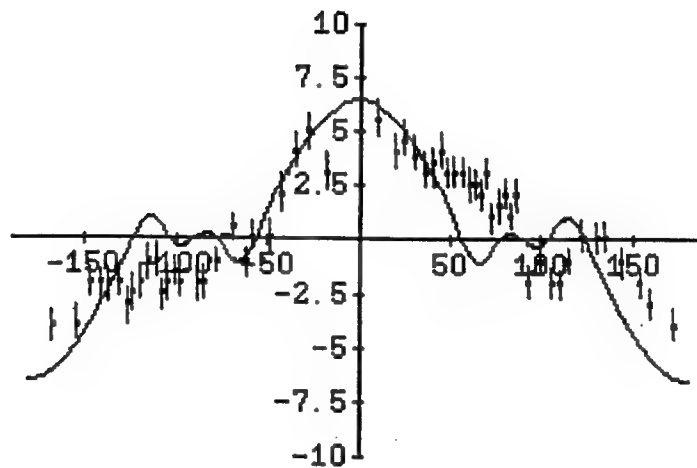
Figure 4.6: A HREM image of a poly(DCHD) three chain end edge dislocation with Burger's vector  $3a/2[100]$ . The lattice fringes correspond to the chain axis.



**Figure 4.7:** A map of the molecular director of the chains in Figure 4.6. The bending of the director is indicative of the splay character of the deformation of the polymer chains.



A



B

Figure 4.8: The experimental tilt measured from HREM images of a three chain end edge dislocation. The tilt was measured with an error of  $\pm 0.5^\circ$ . (a) shows the data overlapped with the solution from liquid crystal columnar theory. A value of  $\lambda = 0.8 \pm 0.1$  nm was used to fit the data. (b) The experimental data matched by the best fit from the anisotropic linear elastic solution. A polymer anisotropy parameter of  $W = 3.5$  was needed to fit the data.

amounts of tilt involved and the localization of the deformation near the defect. A window needed to be four fringes in width and height to produce a peak recognizable over the background in the FFT. The lower limit of area which would be averaged over was thus 3.4 nm square, but the angular resolution in the FFT in this case was only 9.7°. The resolution of this technique was inappropriate for the analysis of dislocations where the tilt is small, although in disclinations where the misorientation is larger, the technique is valuable.

The data was fit using both the columnar liquid crystal and anisotropic linear elasticity derivation. The columnar theory needed a value of  $\lambda = 0.8 \pm 0.1$  nm to fit the experimental data.

The anisotropic elasticity solution was fit using a polymer anisotropy parameter. The introduction of covalent bonding in the chain direction influences several elements of the stiffness matrix. An examination of the stiffness matrix by expanding the contracted notation (Nye, 1957) shows which terms will be effected by the covalent bonds. For example, the component  $c_{3321}$  ( $c_{36}$ ) relates the strain of the chain in the x direction to the normal stress in the chain direction.

We define here an anisotropy parameter,  $W$ , which is a ratio of stiffnesses dependent on c-axis bonding to all other terms. The equation is shown for monoclinic materials but could easily be formulated for polymer crystals of other symmetries.

$$W \equiv \frac{c_{33} + c_{36} + c_{44} + c_{45} + c_{55}}{c_{11} + c_{12} + c_{13} + c_{16} + c_{22} + c_{23} + c_{26} + c_{66}}$$

For DCHD monomer and polymer elastic stiffnesses calculated from molecular mechanics,  $W$  is 0.35 and 1.6 respectively. For isotropic materials,  $W$  reduces to:

$$W = \frac{2c_{11} - c_{12}}{2.5(c_{11} + c_{12})}$$

Using the monomer stiffnesses for  $c_{11}$  and  $c_{12}$ , this equation gives a  $W$  of 0.2. Although the moduli calculated from molecular mechanics predicted an anisotropy of 1.6 for the polymer, the experimental data required a value of 3.5 for a fit. The simulations overestimate the chain modulus and underestimate the transverse modulus when compared to values determined by other researchers. A summary of experimental modulus values published is shown in table 4.2. Future work analyzing these images would be aided if a full stiffness matrix could be experimentally determined. Recent work to measure the full stiffness matrix by Brillouin scattering from a polyimide films has been performed by Kumar et al. (1994).

Figure 4.9 shows the behavior of the tilt around a three chain end edge dislocation as a function of the anisotropy of the polymer moduli. The peaks at  $50^\circ$  and  $130^\circ$  are a result of the shearing of individual repeat units of the chain in the  $x$  direction. As the moduli increase due to the covalent bonding in the  $c$ -direction, the ability of the repeat units in the chain to shear with respect to each other decreases. This results in the suppression of these peaks in the tilt plot and the small lobes in the plot of  $\epsilon_{xy}$ . The magnitude of the tilt in the  $x$  direction (around  $0^\circ$  and  $180^\circ$ ) decreases also. As the anisotropy increases the tilt takes on the characteristics of the columnar solution. The magnitude of the tilt is reduced and the shearing within the chain, evident as a reversal of tilt found between  $40^\circ$  and  $150^\circ$ , is suppressed. As the anisotropy

Table 4.2

## Elastic modulus of diacetylenes

Elastic Constant	GPa	Material	Method	Source
C <sub>33</sub>	62±2	p ETU	Fiber Testing	Young and Petermann (1981)
C <sub>33</sub>	45	p DCHD	Mechanical	Young
C <sub>33</sub>	60	p EUHD		Young
C <sub>33</sub>	50	p TSHD	Theoretical Calculation	Batchelder and Bloor (1979)
C <sub>33</sub>	47	p TS	Brillouin	Enkelmann, Leyrer, and Wegner (1979)
C <sub>33</sub>	45±2	p DCHD	Mechanical	Galiotis (1984)
C <sub>33</sub>	72	p EUHD (thermal)	Raman	Galiotis and Young (1983)
C <sub>33</sub>	74	p EUHD (gamma)	Raman	Galiotis and Young (1983)
C <sub>33</sub>	50	p TSHD	Raman	Galiotis and Young (1983)
C <sub>33</sub>	43.3	p TSHD	Brillouin	Young (1985)
C <sub>33</sub>	10	m TS	Brillouin	Enkelmann, Leyrer, and Wegner (1979)
C <sub>33</sub>	9	m EUHD		Young (1985)
C <sub>33</sub>	6.7	m TSHD	Brillouin	Young (1985)
C <sub>33</sub>	9.7	m TSHD	Sound Velocity	Young (1985)
C <sub>11</sub>	5.5	mTSHD	Brillouin	Young (1985)
C <sub>22</sub>	7	pTSHD	Brillouin	Young (1985)

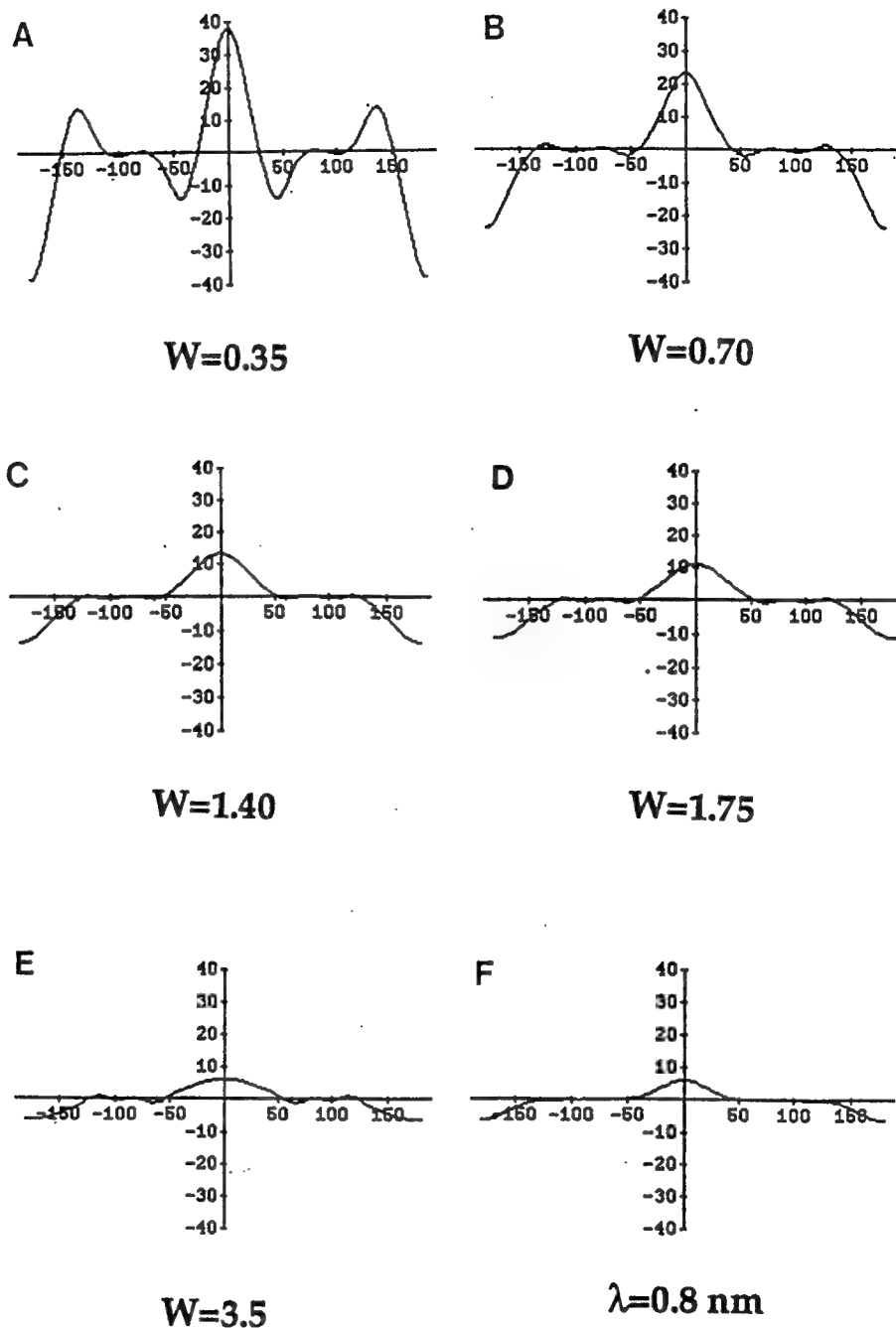


Figure 4.9: Behavior of the tilt around a three chain end edge dislocation as predicted by (a-e) anisotropic linear elasticity for values of  $W=0.35-3.5$ . (f) shows the corresponding solution provided by columnar liquid crystal theory with  $\lambda=0.8 \text{ nm}$ . As the polymer anisotropy parameter,  $W$ , increases the magnitude of the tilt at  $0^\circ$  and  $180^\circ$  decreases. The width of the major tilt distortion increases also. The small lobes are suppressed as the anisotropy is more pronounced until they take a value close to zero and approach the liquid crystal solution.



parameter is increased the width of the parabola that defines the major tilt increases.

Plotting the solutions for the tilt around the dislocation (Figure 4.10) illustrates several conclusions that can be inferred from this analysis. The polymer tilt ( $W=3.5$ ) is very similar to the columnar liquid crystal solution, and they both closely resemble the HREM image. Conclusions can be drawn as to the character of the strain field for the polymer. It was speculated before analysis of the data that the strain field would be a mixture of the characteristics of both monomer and polymer, since the dislocation was formed in the monomer first and then polymerized. The data shows instead that the dislocation character closely resembles that of a polymer dislocation.

Our analysis predicts that the distortion of the monomer lattice is spread over a large area near the dislocation core whereas it is localized near the core in the polymer case. Dynamic dark field images recorded during the polymerization by Liao and Martin (1993) confirm this finding. They observed bend contours in the monomer film which disappeared as the material polymerized under affect of the electron beam. Bend contours appear when the crystal planes are rotated or bent into the Bragg condition used for imaging. The bend contours observed in the monomer correlate to regions of tilt around the dislocation. Upon polymerization, the lattice stiffens and the distortion becomes localized causing the disappearance of the bend contours.

The tilt around the monomer dislocation resembles the behavior of isotropic materials far away from the core. As the core is approached, the tilt varies greatly from point to point and suggests that the elastic solution is not valid close to the core. When the shear stress reaches the shear strength of

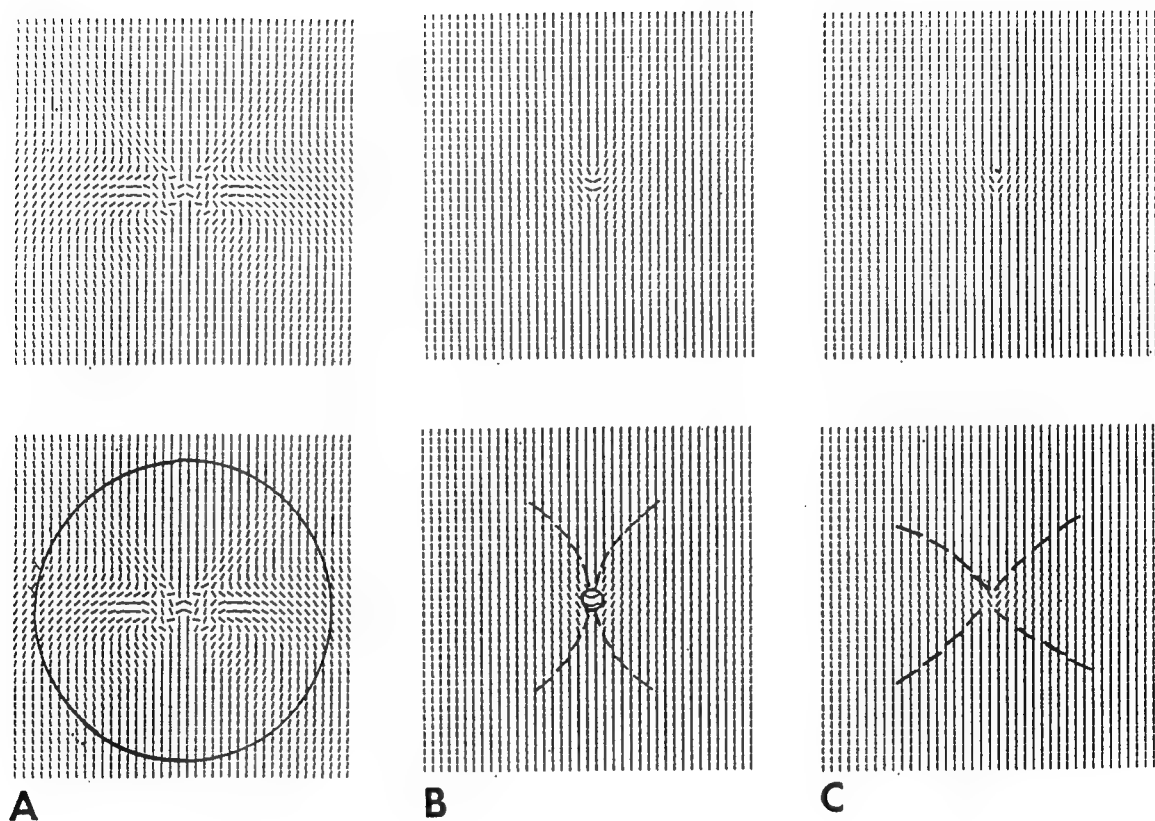


Figure 4.10: Plots of the local tilt for the three solutions: (a) the monomer elastic solution ( $W=0.35$ ), (b) the polymer elastic solution ( $W=3.5$ ), and (c) the columnar liquid crystal solution ( $\lambda=0.8\text{nm}$ ). The monomer solution behaves non-linearly inside a core radius drawn of  $5b$ . The polymer elastic solution is uniform close to the origin of the dislocation. Dashed lines define the parabola inside of which the tilt is non-zero. The polymer and columnar solutions both closely resemble the HREM image of a dislocation in Figure 4.6.

the material it will plastically deform. Once the material deforms plastically, the elastic solution is not applicable. The shear stress required to slide the molecules over one another in the monomer can be described using the analysis of Frenkel (Hirth and Lothe, 1982). The theoretical critical shear stress is:

$$\tau_{th} = \frac{Gb}{2\pi a}$$

where  $a$  is the spacing height of the valley the molecule needs to overcome to move. Experimentally,  $\tau_{critical}$  is found to be between  $G/30$  to  $G/15$  for metals (Hull and Bacon, 1984). The shear stress around an edge dislocation by isotropic elasticity is:

$$\sigma_{xy} = \frac{Gb}{2\pi R}$$

which would equal  $G/30$  at a radius of  $5b$  from the dislocation. This usually is defined as the core of the dislocation. In the monomer diagram, the circle is drawn  $5b$  from the origin. The tilt of the elastic solution for the polymer changes uniformly as the dislocation origin is approached. This suggests that the core may be small. Because of the covalent bonding in the  $y$  direction, the shear stress to plastically deform the chain the  $x$  direction is that needed to break the covalent bond. This should be close to the value of the shear modulus which would bring the value of the core radius to approximately one Burger's vector. The implication is that anisotropic elastic dislocation theory may be considered valid over most of the area around a polymer chain end dislocation.

The elastic strain energies of the dislocations can be calculated for both the monomer and polymer. The elastic strain energy for an isotropic dislocation is:

$$E_{el} = \frac{Gb^2}{4\pi(1-\nu)} \ln\left(\frac{R}{r_o}\right)$$

where  $R$  is usually taken as 1 mm and  $r_o$  is the core radius. For an anisotropic dislocation, the energy takes a similar form:

$$E_{el} = \frac{K_{ij}b_i b_j}{4\pi} \ln\left(\frac{R}{r_o}\right)$$

where  $K_{ij}$  is the energy factor which takes into account all the moduli (see Appendix 4.1). The calculated energies using the anisotropic derivation are  $6.3 \times 10^{-8}$  and  $1.8 \times 10^{-7}$  for monomer and polymer three chain end edge dislocations with core radii of  $5b$  and  $b/6$  respectively. The values are higher by one to two orders of magnitude than those predicted for metals. This may be expected due to the energy penalty for distorting covalent bonds.

This energy penalty is illustrated by experiments to determine the yield strength of diamond (Weidner, et al., 1994). They found that pressures of 10 GPa at 1500°C were needed to plastically deform the material which slipped by the movement of dislocations through the covalent bonds.

Previous estimations of dislocation energies have been made by Shadrake and Guiu (1976) for polyethylene. They used a calculated stiffness matrix and anisotropic dislocation theory to estimate the energies of several types of screw and edge dislocations. If the dislocation did not have an analytical solution available, they dissociated it into partials and used them to

calculate the energy. They found that the energy for screw dislocations was in general 30% less than that for edge dislocations. The most energetically favorable dislocation was a screw dislocation with the line direction and Burger's vector along the chain axis [001]. This dislocation is commonly seen in the growth spirals of polyethylene lamellar crystals and is comprised of the slipping of chains relative to their neighbors in the  $c$  direction. They also were able to predict the anisotropy of the elastic displacements around this type of screw dislocation relative to the isotropic prediction. The anisotropy present showed that the screw dislocation was slightly extended on a plane at an angle of  $54^\circ$  to the  $a$  unit cell axis. Their work was theoretical in nature and only compared qualitatively to show that dislocations experimentally seen were of lowest energy.

The magnitudes of the elastic strain energy calculated by Peterson and Lindenmeyer (1966), and Shultz (1974) are two magnitudes lower than those for metals. This is due to the type of dislocation investigated. A screw dislocation where the slippage of chains past each other in the chain axis direction should be the lowest energy dislocation in polymers, depending on a small shear modulus. The shear modulus for polyethylene ( $10^{10}$  dyne/cm<sup>2</sup>) is lower than the typical metal. A similar screw dislocation in DCHD might have a higher energy because of the large carbazol side groups compared to the small CH<sub>2</sub> groups of polyethylene. The value for a [001] screw dislocation in polyethylene,  $\sim 10^{-5}$  erg/cm should form the lower bound for polymer dislocation energies. Edge dislocations have larger strain fields and thus will have higher energies than screw dislocations.

The core energy of the polymer dislocation may be significant due to the electronic structure of the chain end. Contributions to the elastic energy due to electronic structure changes because of chain bending are also not

accounted for in the calculation. The polydiacetylene chain may be terminated by several different structures dependent on chain length (Wright, 1989). Below a degree of polymerization of six, diradicals are seen whereas in longer chains dicarbenes exist. In the dicarbene a  $p_z$ -electron can become delocalized and move along the chain, its position defining the phase boundary between the butatriene and acetylene regions of the chain. This structure may be stable for long chains where the energy gained by the combination of the  $p_z$ -electron with another at the far end of the chain to form a  $\pi$  bond is offset by the energy required to move the electron over that distance.

The implications of the possible electronic structure changes at the core and due to chain distortion are apparent for device fabrication. Diacetylenes are known as one dimensional semiconductors because of the conjugation along the extended backbone and the large distance ( $\sim 0.7$ - $0.8$  nm) between chains which inhibit a lateral hopping between chains. Traps would be created at dislocations formed by chain ends where the conjugation is disrupted. Bending of the backbone could also disturb the conjugation length. Hone and Singh (1992) have treated this problem for the nonlinear susceptibility of diacetylenes. They looked at the effect of a random distribution of bond breaking defects on the nonlinear susceptibility ( $\chi^3$ ) using a tight binding (Huckel) model. They found that the susceptibility was decreased as the density of  $\pi$ -bond breaking defects increased.

Experiments measuring the photocurrent through manufactured polydiacetylene bicrystals being undertaken in our laboratory should give insight on the behavior of these traps. The "depth" of the trap or ease of charge carrier jumping between chains may be illuminated. Information

from these experiments and the data presented in this thesis could provide the framework necessary to design devices based on bicrystal geometries.

Chain end dislocations form from the aggregation of point defects, such as substitutional or vacancy defects, in the monomer state while it is swollen. The swollen monomer would allow dislocation formation to lower the energy of the lattice. The subsequent polymerization would freeze in the dislocations into the polymer lattice.

The chain end dislocations can be classified as sessile with respect to their ability to move. Movement by glide would be restricted because neighboring covalent bonds would have to be broken. Climb, would be possible if the chain was more flexible and could include dispiration, disclination, dislocation defects as defined and described by Reneker et al. (1983) that would reptate along the chain under an applied stress. But the extended conformation of polydiacetylene precludes this as a possibility.

This is in contrast to the  $b=[001]$  edge dislocations mentioned in Chapter II. Dislocations with a Burger's vector parallel to the chain have a lower Pierels barrier to their movement by glide along the Burger's vector and would be termed glissile. Similar glissile dislocations have been described in polyethylene (Shultz, 1974). Their movement is the mechanism that explains shearing of the lamella when a crystal settles on a substrate step or particle.

## Conclusion

The introduction of covalent bonds in the chain direction increases the anisotropy of the elastic modulus. This anisotropy was shown to suppress the effect of shear between the chains due to weakening of correlations between chains. As the anisotropy increased, the behavior of the shear stress

approached that seen in columnar liquid crystals where correlations along the chain are removed by symmetry constraints.

The strain field around chain end edge dislocations in DCHD manifest as the tilt of the chains has been experimentally quantified from HREM images. Theoretical modeling using anisotropic linear elastic dislocation theory was used to predict the anisotropy of the elastic moduli. The polymer anisotropy defined as the ratio of stiffnesses dependent on covalent bonds in the chain direction to those unaffected, was determined to be 3.5 by matching the theoretical tilt with the data. By varying the anisotropy it was found that the shear strain field behaved like that for a columnar liquid crystal dislocation as the anisotropy increased due to covalent bonding along the chain direction. The character of the distortion, manifest as a splaying of the chains, was more like the polymer prediction than the monomer suggesting that large scale relaxations take place around the defect during polymerization.

The uniformity of the polymer elastic solution near the dislocation origin suggests that the core is small. Although this effects the area over which the elastic solution is applicable, it does not give a more accurate prediction of the strain energy. Effects due to electronic structure changes and the structure of the chain ends should make the core energy significant. Dislocation strain energies were found to be higher than comparable dislocations in metals due to the bending of covalent bonds.



## APPENDIX 4.1

**Procedure to calculate the strain field for a chain end dislocation in an anisotropic media**

For the DCHD chain end dislocations discussed in this chapter the following procedure was used to determine the shear strain and tilt around a dislocation. The compliance matrix determined by Polygraf,  $s_{ij}$ , is a 6x6 matrix in contracted form and referenced to the unit cell (monoclinic) coordinate system. This coordinate system, shown as  $a, b, c$  in Figure 4.3 is not in the correct reference frame to use for anisotropic theory. The derivation uses an orthogonal axis system with the dislocation line parallel to the  $x_1$  axis and the diad axis of symmetry as  $x_2$ . In order to perform the needed transformations of the compliance matrix to the correct coordinate system, the matrix must be in its full 9x9 format.

Expansion of the compliance matrix,  $s_{ij}$  to  $s_{ijkl}$  uses the contraction rules (1=11, 2=22, etc.) as listed by Steeds (1973). The full compliance matrix,  $s_{ijkl}$ , is transformed to an orthogonal coordinate system from the monoclinic system by:

$$s'_{ijkl} = l_{ip} l_{jq} l_{kr} l_{ls} s_{pqrs}$$

$$l_{im} = \cos(x'_i, x_m)$$

where  $l_{lm}$  are the direction cosines of new ( $x'_i$ ) coordinate system relative to the old one ( $x_m$ ). Summation over the duplicated variables is assumed unless otherwise noted. The  $l_{lm}$  for the experimental situation was:

$$l_{lm} = \begin{bmatrix} \cos \gamma & 0 & 0 \\ \cos(\frac{\pi}{2} + \gamma) & 1 & 0 \\ 0 & 0 & 1 \end{bmatrix}$$

A second transformation is necessary to find the stiffness matrix for the dislocation coordinate system outlined above. The direction cosines used were:

$$l_{lm} = \begin{bmatrix} 1 & 0 & 0 \\ 0 & 0 & 1 \\ 0 & -1 & 0 \end{bmatrix}$$

The resulting compliance matrix (9x9) is referenced to the correct coordinate system but must be contracted to the 6x6 form,  $s'_{ij}$ , via the contraction rules cited before. Since  $\epsilon_{33}$  will be considered zero, the compliance matrix can be further simplified. A reduced compliance matrix,  $S'_{ij}$  is calculated from  $s'_{ij}$  via:

$$S'_{lm} = s'_{lm} - (s'_{3l} s'_{3m} / s'_{33})$$

The solutions to the differential equation derived from the equations of compatibility are a function of  $p$ . Solving for  $p$  results in a sextic equations which needs to be solved for  $p_n$  (1->6).

$$p^6 - q_1 p^4 + q_2 - q_3 = 0$$

Where

$$q_1 = -\left\{ \frac{S'_{11} S'_{44} + S'_{55} (2S'_{12} + S'_{66}) - 2S'_{15} (S'_{25} + S'_{46})}{S'_{11} S'_{55} - S'^2_{15}} \right\}$$

$$q_2 = \frac{S'_{22} S'_{55} + S'_{44} (2S'_{12} + S'_{66}) - (S'_{25} + S'_{46})}{S'_{11} S'_{55} - S'^2_{15}}$$

$$q_3 = -\frac{S'_{22} S'_{44}}{S'_{11} S'_{55} - S'^2_{15}}$$

The roots will occur as pairs of complex conjugates  $p_n = p'_n \pm ip''_n$  ( $n=1, 2, 3$ ). The roots are chosen so that either:

$$\begin{aligned} & \text{(a)} \\ p_1 &= ip''_1 \\ p_2 &= p'_2 + ip''_2 \\ p_3 &= -p'_2 + ip''_2 \end{aligned}$$

$$\begin{aligned} & \text{(b)} \\ p_1 &= ip''_1 \\ p_2 &= ip''_2 \\ p_3 &= ip''_3 \end{aligned}$$

DCHD monomer and polymer are both case a). The roots found for the Polygraf simulated stiffnesses were:

monomer		polymer	
p1	1.5802 i		0.501663 i
p2	0.703452 + 0.656873 i		0.324411 + 0.377039 i
p3	-0.703452 + 0.656873 i		-0.324411 + 0.377039 i

These roots are in general similar to roots for other materials (Teodosiu, 1982), the monomer being closer in magnitude since it is less

anisotropic in nature. Several sets of constants are developed as part of the solution to the differential equations.

$$\gamma_n = -\frac{(S'_{15}p_n^2 + S'_{25} + S'_{46})p_n}{S'_{44} + S'_{55}p_n^2}$$

(no summation)

$$\mathbf{s} = [s_1, s_2, s_3] = \mathbf{p} \times \boldsymbol{\gamma}$$

$$D = s_1 + s_2 + s_3$$

$$B_n(b_1) = -\frac{K_2 b_1}{4\pi D} p_n s_n$$

(no summation)

$$K_2 = \frac{D}{iS'_{22}(s_1/p_1 + s_2/p_2 + s_3/p_3)}$$

$$K_1 = \frac{K_2 p_n^2 s_n}{D}$$

$K_1$  and  $K_2$  are the energy factors, and are used in calculating the energy of a dislocation. The stresses,  $\sigma_{ij}$ , are found for each component of the Burger's vector. In our case,  $\mathbf{b}=[b_1 \ 0 \ 0]$  so only terms derived for  $b_1$  are needed.

$$\sigma_{11}(b_1) = \frac{b_1 K_2 x^2}{2\pi D y} \frac{p_n^2 s_n}{x^2 - p_n^2 y^2} - \frac{K_1 b_1}{2\pi y}$$

$$\sigma_{12}(b_1) = \frac{b_1 K_2 x}{2\pi D} \frac{p_n^2 s_n}{x^2 - p_n^2 y^2}$$

$$\sigma_{22}(b_1) = \frac{b_1 K_2 y}{2\pi D} \frac{p_n^2 s_n}{x^2 - p_n^2 y^2}$$

$$\sigma_{13}(b_1) = \frac{b_1 y [x^4 p_n^3 \gamma_n s_n + (q_3 \gamma_n s_n / p_n - q_2 \gamma_n s_n p_n) x^2 y^2 + p_n \gamma_n s_n q_3 y^4]}{2\pi i S'_{22} (s_m / p_m) (x^6 - q_1 x^4 y^2 + q_2 x^2 y^4 - q_3 y^6)}$$

$$\sigma_{23}(b_1) = \frac{b_1 x [x^4 p_n \gamma_n s_n + (\gamma_n s_n p_n^3 - q_1 \gamma_n s_n p_n) x^2 y^2 + (\gamma_n s_n / p_n) q_3 y^4]}{2\pi i S'_{22} (s_m / p_m) (x^6 - q_1 x^4 y^2 + q_2 x^2 y^4 - q_3 y^6)}$$

The tilt,  $\varepsilon_{12}$ , is then found from:

$$\varepsilon_{ij} = s'_{ij} \sigma_{ij}$$

## **CHAPTER V**

### **PREDICTION OF GRAIN BOUNDARY STRUCTURE AND PROPERTIES USING O-LATTICE THEORY**

#### **Introduction**

Many polymers are made up of small crystallites surrounded by grain boundary regions. By definition, a grain boundary is the interface between two adjacent crystals, so it is expected that the properties of crystalline polymers will be greatly effected by grain boundaries. The role of grain boundaries in determining the properties of crystalline polymers is not yet well established. There are several reasons for this lack of information. The disorder inherent to semi-crystalline polymers makes studies designed to isolate the grain boundary difficult. Also, common methods to investigate the molecular organization in a grain boundary such as HREM are limited by the radiation damage susceptibility of organic materials. A series of studies in our laboratory are attempting to address these questions by using polydiacetylenes, a model crystalline polymer system.

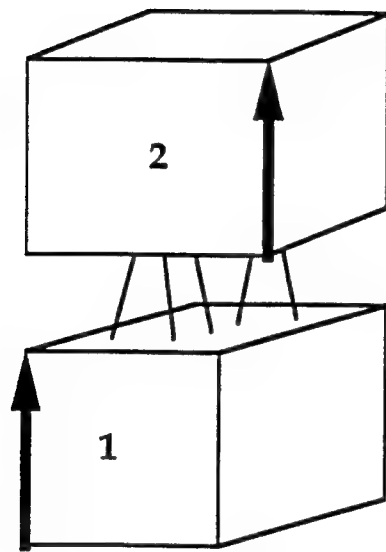
Previous theoretical work by Bevis in 1978 classified deformation twins in polymers as either chain invariant or chain rotation depending on whether the chains were parallel or not. Bevis failed to consider the orientation of the domain boundary plane in his analysis. This was expanded on by Martin and Thomas (1991) who provided a more complete framework to classify polymer grain boundaries. Martin and Thomas discussed two

parameters, the orientation relationship between the chain direction in the two crystallites and the orientation of the grain boundary plane. This resulted in four classifications: lateral chain invariant, lateral chain rotation, axial chain invariant, and axial chain rotation grain boundaries. If the chain orientation in each crystallite is denoted  $c_1$  and  $c_2$ , then lateral boundaries are formed when the plane of the grain boundary is parallel to both  $c_1$  and  $c_2$ . Axial boundaries are found when the plane of the boundary is not parallel to either  $c_1$ ,  $c_2$ , or both. Axial boundaries are expected to effect polymer properties more than lateral boundaries since they cross the chain axis resulting in breaking, bending, or twisting the chain. The chain axis is not crossed in a lateral boundary so polymer properties are only influenced by misorientation of the crystallite from the axis of interest.

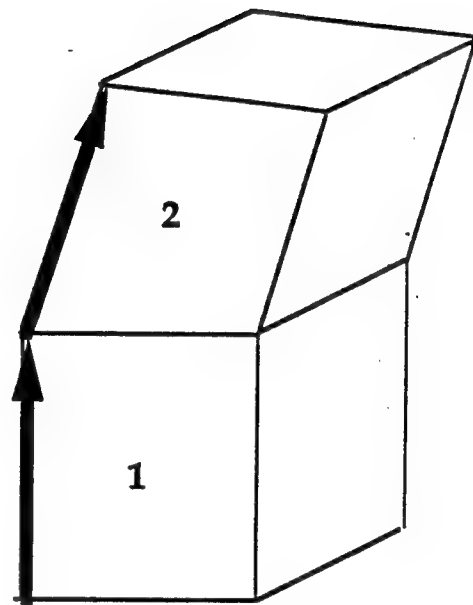
Figure 5.1 is a schematic of the two types of axial boundaries: axial chain invariant (ACI) and axial chain rotation (ACR) as described by Martin and Thomas. The orientation of the chain from one crystallite to the next separates these two classes. If the chain axis directions are parallel then an ACI boundary exists, which can also be called a twist boundary as drawn. When the two directions are not parallel, a rotation of axes have occurred defining a ACR boundary. A pure tilt boundary is a special case of this.

Although Martin and Thomas ranked the classifications in terms of expected boundary energies they did not support this analysis with explicit energy calculations. They also discussed qualitatively how grain boundaries might effect property relationships. But neither discussions included how the energy or properties would vary with misorientation angle.

Martin and Thomas went on to show an example of a ACI boundary in a HREM image of a poly(p-phenylenebenzobistiazole) (PBZO) fiber. They



**ACI Grain Boundary**  
**Twist**



**ACR Grain Boundary**  
**Tilt**

**Figure 5.1: Definition of grain boundaries where the interface disrupts the chain axis. A twist boundary of this type may be called an axial chain invariant (ACI) boundary and a tilt boundary as an axial chain rotation (ACR) after Martin and Thomas (1991).**



recognized two crystallites along the fiber axis, one with a (200) orientation as noted from the 0.55 nm fringes and another with a (010) orientation represented by 0.35 nm fringes. The boundary between the two crystallites was diffuse over a region 5.0 nm long. They suggested a model of the boundary where the chains twist and translate to move from one crystallite to the next.

Martin (1992) went on to expand on twist defects in a theoretical study which determined their general properties. His constitutive model, based on those derived for twisted wire rope, predicted a Poisson's ratio equal to 2.0 to fit the data simulated from molecular mechanics. This would require the system's density to increase under an applied load. Martin's simulations though, were based on the Dreiding II force field (Mayo, et al, 1990) using a Fletcher-Powell minimization scheme with a gradient convergence criterion of 0.1 kcal/mol. Minimizations to predict moduli of DCHD in Chapter IV needed a convergence criterion ten times less than that used by Martin in his analysis to predict positive Young's moduli. This suggests that his simulations may not have been fully minimized.

Jones et al. (1994) recently showed that grain boundaries are important in determining the reactivity of PPTA-XTA copolymers. A crosslinkable BCB moiety on the terephthalic acid unit segregated into (100) planes within the crystallites. As a result, for the average crystallite size, 70% of the active units were at the interface. The efficiency of the crosslinking reaction during post processing heat treatment was also on the order of 70%, implying that the reaction occurred preferentially at the grain boundary interface.

The understanding of grain boundaries is better developed in atomic crystals. Several researchers have performed bicrystal experiments to determine structure-property relationships. Dimos, et al. (1990) recently

showed that the grain boundary interface was the weak link in the critical current density of superconducting  $\text{YBa}_2\text{Cu}_3\text{O}_7$  bicrystals.

Here we will discuss a few geometrical theories which describe the structure of grain boundaries: the dislocation model, coincident site lattice (CSL) construct, O-lattice theory, and computer simulations based on interatomic potentials. The coincident site lattice theory is actually a special case of O-lattice theory, and will be treated as such in our discussion.

The dislocation model describes the structure of low angle grain boundaries in terms of discrete lattice dislocations. The relationship which describes the set of dislocations that produce a general grain boundary was described by Frank (Hull and Bacon, 1984):

$$\mathbf{d} = (\mathbf{r} \times \mathbf{l}) 2 \sin \frac{\theta}{2} \equiv (\mathbf{r} \times \mathbf{l}) \theta$$

where  $\mathbf{r}$  is any arbitrary unit vector in the plane of the boundary,  $\mathbf{l}$  is the unit vector parallel to the axis of relative rotation of the two crystals,  $\theta$  is the angle of rotation about  $\mathbf{l}$ , and  $\mathbf{d}$  is the sum of the Burger's vectors of all the dislocations intersected by  $\mathbf{r}$ . For a simple tilt or twist boundary the spacing,  $D$ , between the sets of dislocations for small angles is:

$$D = b / \theta$$

The dislocation model is only valid at low angles where the distances between dislocations are large enough so the cores of individual dislocations do not overlap.

O-lattice theory developed by Bollman (1970) provides a useful means to describe the geometry of interfaces. It formulates the geometry as a

function of coincidences of equivalent points in the lattice. Coincident site lattices (CSL) are a subset of Bollman's theory. CSL's are limited because they describe only special cases of atom overlap between two misoriented crystals, whereas O-lattice theory continuously describes the overlap as a function of angle. This makes it very powerful and allows its use to model misorientation-property relationships, as will be shown.

As a special case of O-lattice theory, coincidence site lattices were derived separately from the recognition that at certain rotations of two crystals a three-dimensional periodicity of coincidences of lattice points existed. The degree of matching between two crystals is specified by the reciprocal density,  $\Sigma$ , of coincidence lattice points in terms of the density of ordinary lattice points. Thus a small  $\Sigma$  would signify higher coincidence between the two crystals. Boundaries with low  $\Sigma$  values have been found to have low energies or high migration rates in the presence of impurities (Sutton, 1984).

Orientations of crystals with small  $\Sigma$  are usually determined by inspection. As the lattice becomes more complicated by reductions in symmetry, it is difficult to ascertain CSL's. No general relationships which provide all values for  $\Sigma$  are known, although few special cases have been formulated. It would be more appropriate to use the O-lattice language instead.

Since O-lattice theory was introduced, it has found limited use, perhaps because of the mathematical complexity of the description used in its definition. Also metallurgists and ceramists are more interested in models which predict atomic configurations to use in analysis of HREM micrographs or predict low energy structures. King et al. (1994) have used O-lattice theory to describe a constrained coincidence-site lattice (CCSL) for orthorhombic and

tetragonal crystals. A CCSL is a CSL with a small strain applied to fit the lattices to a set of axial rules. The CCSL construction is especially applicable for interphase grain boundaries where the two lattices are different and a small strain must be included to form any coincidence between them.

Computer simulations of grain boundary structure rely on estimates for the energy potentials between atoms. The method is to assign ideal lattice atomic positions to two halves of a block misoriented by an angle and separated by a boundary plane (Wolf, et al. 1989-1992). The problem is to minimize the energy of the block according to some method of relaxation and periodic boundary conditions. Inconsistencies in the predictions of atomic arrangement are often due to the interatomic potentials used. In metals, usually these are found from ab-initio calculations and assumptions of van der Waals or ionic attractions. For organic materials, such force fields are formulated from available sets of thermodynamic properties and crystallographic data. Krimm, et al. (1994) have shown that force fields commonly in use in available molecular modeling software (Polygraf (Molecular Simulations, Inc., 1993) and BioSym (Bioscience Resource Project, 1993)) do not correctly predict observed vibrational spectra. They stress that new force fields for organic material should be derived by also incorporating available vibrational spectroscopy data.

Energy calculations for organic materials need to incorporate the bending and stretching of covalent bonds, van der Waals interactions, and hydrogen bonding. A simulation of a grain boundary in a polymer would require that the block chosen is periodic along the plane of the grain boundary so that the environment of molecules at the edge resembles that of the bulk. The block must also be sufficiently thick to negate the effects of extra boundaries created from the periodic replication of the block perpendicular to

the grain boundary. One method would be to choose blocks whose vertices are O-lattice points. For DCHD the distances between O-lattice points are of the order of several unit cell parameters at angles of misorientation of 3-5°. Combined with the thickness requirement, the number of atoms required is on the order of thousands to tens of thousands compared to hundreds in metallic or ionic systems (Wolf, 1989). The time to minimize a structure with minimization schemes, such as steepest descent, conjugate gradient, and Newton-Raphson, scale as  $N$  to  $N^3$  where  $N$  is the number of atoms. The number of atoms needed to correctly simulate crystalline polymer interfaces within periodic boundary conditions makes this technique too computationally intensive to use.

Sutton and Balluffi (1987) have shown that geometrical descriptions of interfaces are limited in their ability to determine the energetics of grain boundaries in atomic and small molecule crystals. However, the strong anisotropic bonding in polymers may make geometrical concerns useful for description of boundary-property relationships.

To measure the influence of grain boundaries on properties such as photoconductivity and mechanical strength, a set of controlled bicrystal experiments have been performed in our laboratory by Liao (1994). His method was to grow large monomer single crystals of DCHD, cut them using a solvent saw, and rejoin them in a controlled misorientation. The interfacial region was rejoined by immersing the fixed crystals in a slightly undersaturated solution of monomer in acetone. This removed a small amount of damaged material at the interface. The two crystals were held together under the load of a weak spring. Slow controlled evaporation of the acetone induced regrowth to connect the two crystals and form a bicrystal.

Liao has successfully formed both twist and tilt monomer boundaries for study.

Subsequent polymerization of the bicrystals qualitatively revealed the amount of chain connectivity at the interface. Bicrystals with misorientation larger than  $25^\circ$  broke apart when polymerized using either thermal or gamma radiation. Bicrystals that remained intact retained an appreciable fraction of the single crystal tensile strength confirming the presence of covalent bonding through the interface.

Experiments using a time of flight technique have measured the photoconductive response through the grain boundary. A series of grain boundaries with different misorientation angles showed that the photoconductive response decreases with increasing misorientation angle.

The purpose of this study was to model the behavior of these property measurements. Information about the extent of relaxation at the grain boundary and dominant modes of transport was expected to be determined. A model could be useful in the future to help design devices based on bicrystals.

### O-lattice Theory

O-lattice theory, as described by Bollman (1970), is a geometrical construction relating points from one crystal to another as a function of their relative misorientation. Whereas CSL theory defines coincidence as the overlap of atoms or lattice points (point groups), O-lattice theory defines a set of "O-points" which are generalized lattice coincidences. These generalized lattice coincidence sites are coincidences of elements of related equivalent classes. An equivalence class is where the internal coordinates of the point is the same. For example, the points (12.333, 5.554, and 6.354) have external

coordinates of (12, 5, 6) being multiples of the corresponding unit cell parameter. The internal coordinates are (0.333, 0.554, 0.354) which are fractions of the corresponding unit cell parameter. Figure 5.2 shows four sets of equivalence classes. While the CSL formalism only includes the subset called lattice points, the O-lattice approach includes all points in space.

As described by Bollman (1970), every point in one crystal (denoted by a vector  $\mathbf{x}^{(1)}$ ) is related to a point in another crystal ( $\mathbf{x}^{(2)}$ ) by the direction cosine matrix  $\mathbf{A}$ :

$$\mathbf{x}^{(2)} = \mathbf{A}\mathbf{x}^{(1)}$$

All other points of the same equivalence class in a crystal can be found by adding the translation vector of the lattice,  $\mathbf{t}$ , to the coordinates of the point:

$$\mathbf{e} = \mathbf{x}^{(1)} + \mathbf{t}^{(1)}$$

where  $\mathbf{e}$  are the other points in the equivalence class. If the points  $\mathbf{x}^{(1)}$  and  $\mathbf{x}^{(2)}$  coincide then we call them O-points,  $\mathbf{x}^o$ , and the general relationship exists:

$$\mathbf{x}^{(2)} = \mathbf{x}^{(1)} + \mathbf{t} = \mathbf{x}^o$$

Combining this equation with the relationship between the two crystals defined by  $\mathbf{A}$ , results in:

$$\mathbf{x}^o = (\mathbf{I} - \mathbf{A}^{-1})^{-1}\mathbf{t}$$

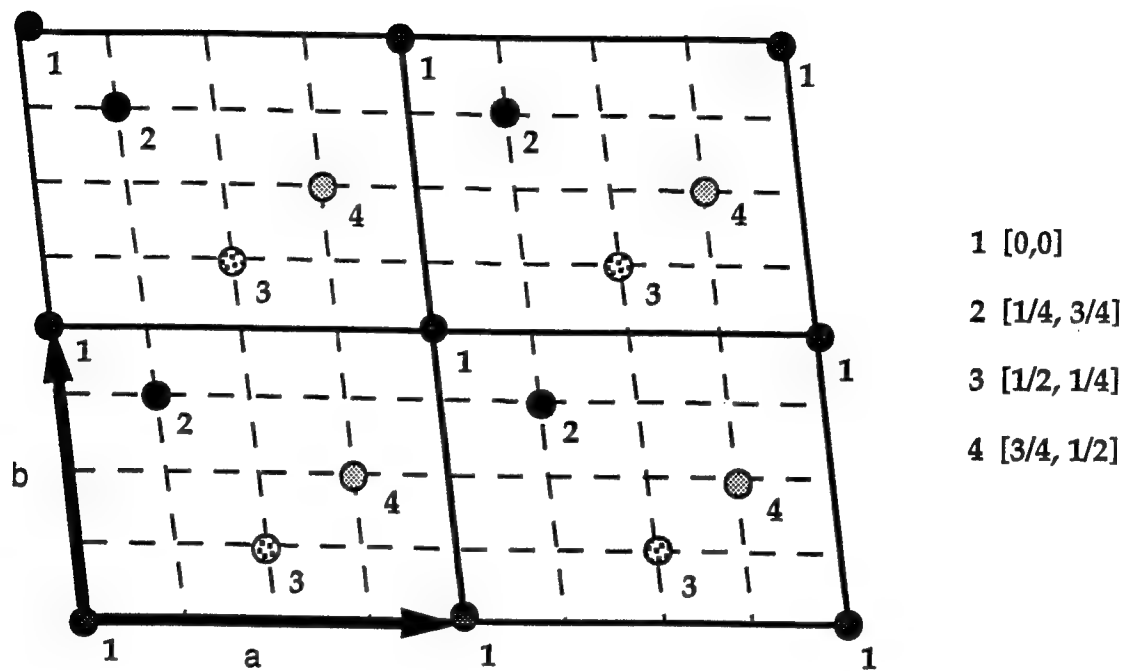


Figure 5.2: A schematic showing equivalent classes in four unit cells. Each numbered point in a unit cell is equivalent to the same numbered point in another unit cell (Adapted from Bollman, 1970).



where  $\mathbf{I}$  is the identity matrix. Bollman calls all the translation vectors of the crystal,  $\mathbf{b}^L$ , thus the set of all points which define the O-lattice,  $\mathbf{X}^o$ , are:

$$\mathbf{X}^o = (\mathbf{I} - \mathbf{A}^{-1})^{-1} \mathbf{b}^L$$

For twist grain boundaries where the chain axis is invariant between crystals,  $\mathbf{A}$  is the two-dimensional matrix of the direction cosines between the orthogonal coordinate systems:

$$\mathbf{A} = \begin{bmatrix} \cos \theta & -\sin \theta \\ \sin \theta & \cos \theta \end{bmatrix}$$

In order to use the O-lattice construct to describe the geometry of non-cubic materials, the metric tensor of the crystal,  $\mathbf{S}$ , needs to be incorporated into the O-lattice solution. Incorporating  $\mathbf{S}$  to relate the point from one non-cubic lattice to another non-cubic lattice results in:

$$\mathbf{x}^{(2)} = \mathbf{S} \mathbf{A} \mathbf{S}^{-1} \mathbf{x}^{(1)}$$

Rederiving the O-lattice construct from this results in a general form applicable for non-cubic materials:

$$\mathbf{X}^o = (\mathbf{I} - \mathbf{S}^{-1} \mathbf{A}^{-1} \mathbf{S})^{-1} \mathbf{b}^L$$

If we take Bolman's construction and derive it for monoclinic materials the following relationships apply. For twist around the c-axis of monoclinic materials, the transformation matrix is:

$$S = \begin{bmatrix} a & 0 \\ b \cos \gamma & b \sin \gamma \end{bmatrix}$$

Calculating the matrix operations results in:

$$(I - S^{-1}A^{-1}S)^{-1} = \begin{bmatrix} \frac{1 - \cos \theta - \frac{b}{a} \cos \gamma \sin \theta}{2(1 - \cos \theta)} & -\frac{\sin \theta (\frac{b}{a} \cot \gamma \cos \gamma + \frac{a}{b} \csc \gamma)}{2(1 - \cos \theta)} \\ \frac{\frac{b}{a} \sin \gamma \sin \theta}{2(1 - \cos \theta)} & \frac{1 - \cos \theta + \frac{b}{a} \cos \gamma \sin \theta}{2(1 - \cos \theta)} \end{bmatrix}$$

As in the crystal coordinate system, the two basic translation vectors in the plane of the boundary are given by the coordinates (1, 0) and (0, 1), the O-lattice vectors,  $u_1$  and  $u_2$ , are given by the column vectors of the matrix:

$$(I - S^{-1}A^{-1}S)^{-1} = \begin{bmatrix} u_{11} & u_{21} \\ u_{12} & u_{22} \end{bmatrix}$$

$$u_1 = (u_{11}, u_{12})$$

$$u_2 = (u_{21}, u_{22})$$

### Prediction of Grain Boundary Properties

The above O-lattice derivation provides the geometrical description of the grain boundary formed when two DCHD monomer crystals are brought together with a twist angle of  $\theta$ . Baughman (1974) predicted that if two

monomer units were not in a narrow range of positions with respect to each other, they would be unable to polymerize. By applying Frank's idea of discrete dislocations existing at the interface, Bollman extended the geometrical description of the O-lattice to include relaxations. He described O-lattice sites as nucleation sites for relaxation to a more perfect structure to reduce the energy of the boundary (Figure 5.3). For a twist boundary the regions between the relaxed areas become two interpenetrating grids of screw dislocations (Figure 5.4). Two sets of screw dislocations are needed to offset the shear produced by one alone. As the angle of twist increases, the density of dislocations also increase as shown in Figure 5.5.

The hypothesis we have used to predict properties assumes that relaxed regions would allow polymerization while the unrelaxed regions would not. Thus the fraction of relaxed area would correspond to the fraction of chains covalently bonded through the grain boundary. For properties which are chain connectivity dependent, such as tensile strength and conduction along the conjugated backbone, this would be proportional to the magnitude of the response. The fraction of relaxed area,  $f$ , can be formulated from the O-lattice geometry. Figure 5.6 illustrates this geometry. The area of an O-lattice unit cell is the product of the O-lattice vectors,  $\mathbf{u}_1$  and  $\mathbf{u}_2$ . The relaxed area of an O-lattice unit cell is the product of each O-lattice vector minus the width of the unrelaxed line ( $b_1$  and  $b_2$  for screw dislocations).

$$f = \frac{(|\mathbf{u}_1| - b_1)(|\mathbf{u}_2| - b_2)}{|\mathbf{u}_1||\mathbf{u}_2|}$$

The relaxation width at the grain boundary is not precisely known. In order to obtain this information the experimental data was fitted with a

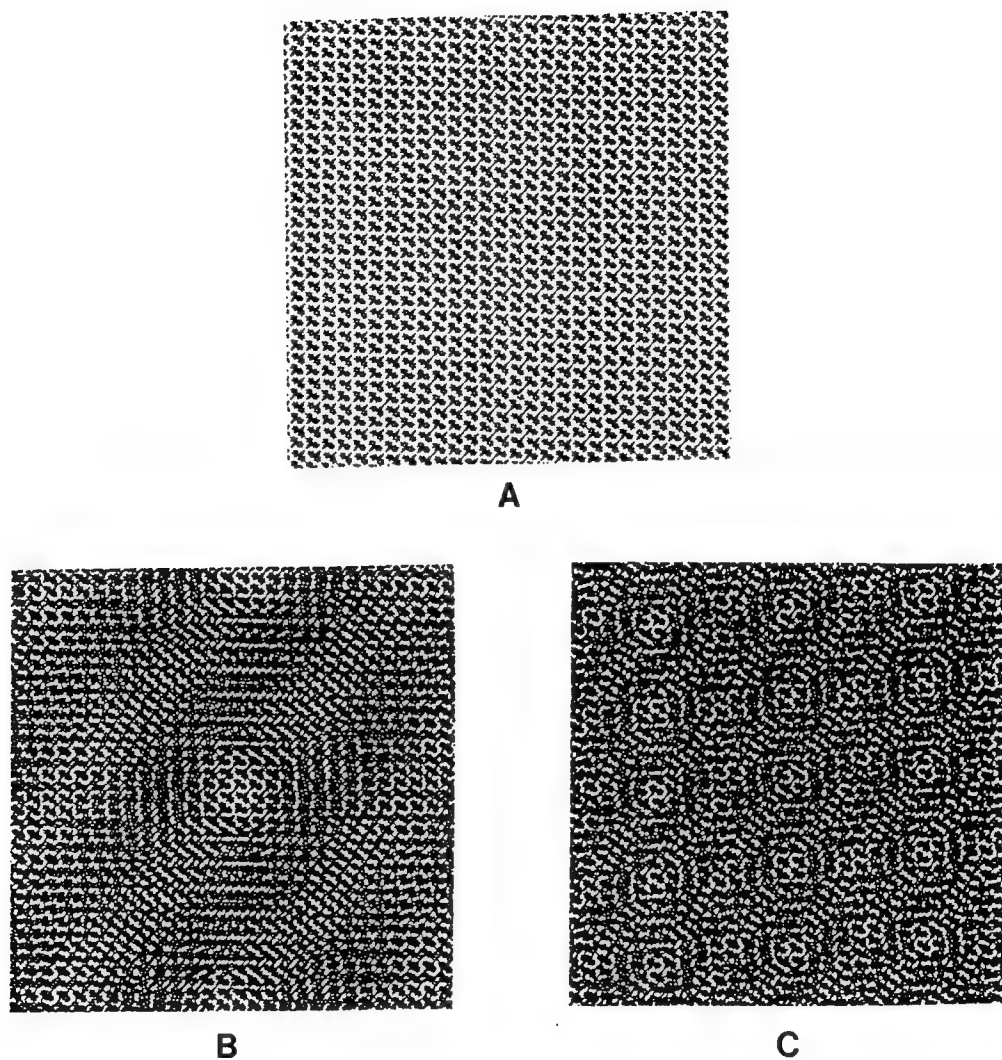


**Figure 5.3:** (a) Projection of the DCHD monomer down the c-axis which will eventually become the chain axis after polymerization. (b) The c-axis projection of a 3° twist misorientation between two crystals showing overlap of few molecules. (c) A 10° twist misorientation projection which increases the number of overlap sites. These sites of overlap are called O-lattice points. These points are the nucleation for relaxation at the interface.

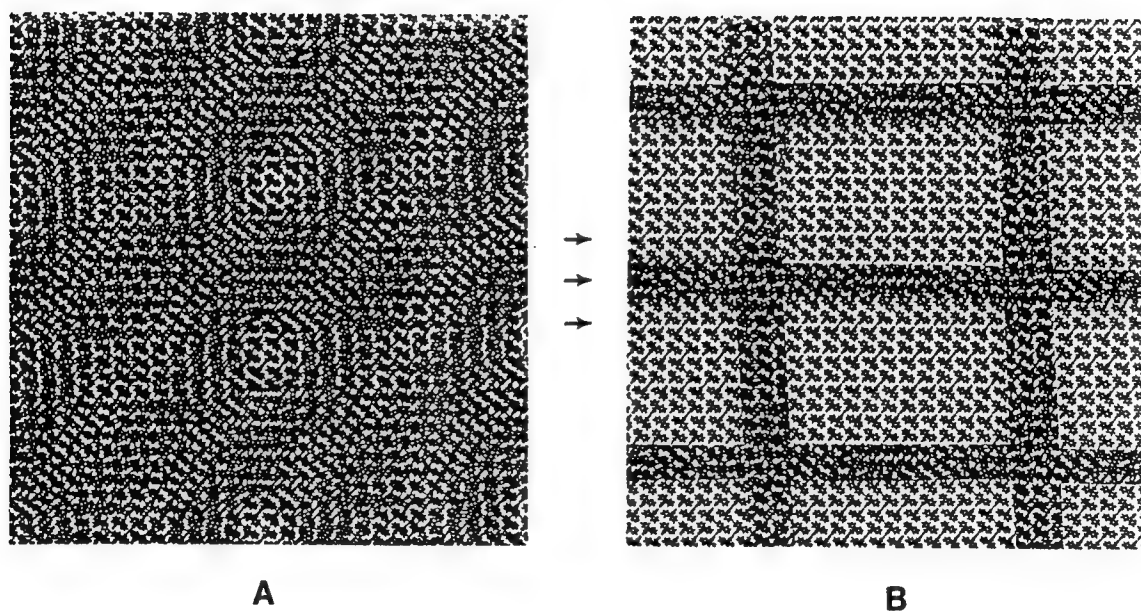


Figure 5.4: (a) C-axis projection of a  $5^\circ$  twist misorientation between two monomer DCHD crystals. Relaxation of the interface begins at the O-lattice sites. (b) The relaxed boundary in (a). The interface relaxes into regions of perfect overlap and a network of screw dislocations.

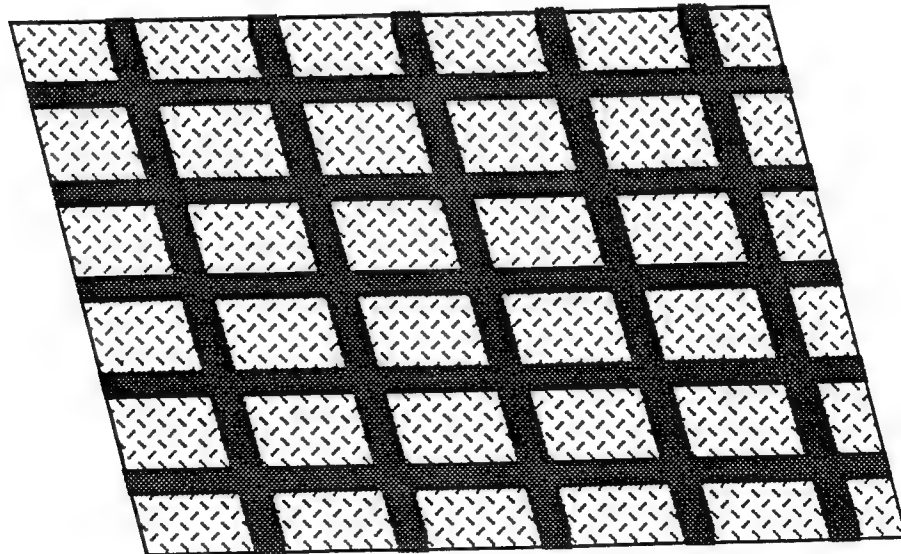
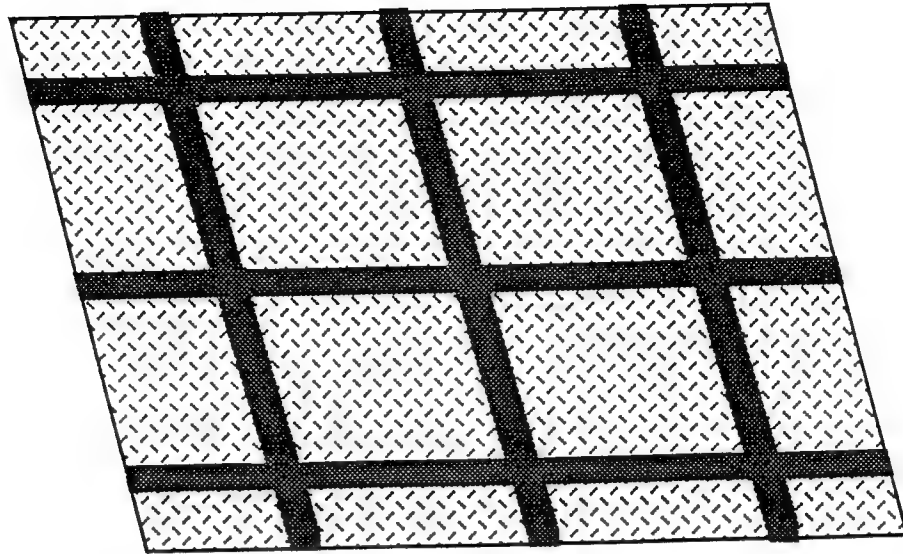


Figure 5.5: Two relaxed twist grain boundaries illustrating that the density of screw dislocations increases as the angle of misorientation of the crystals increases.

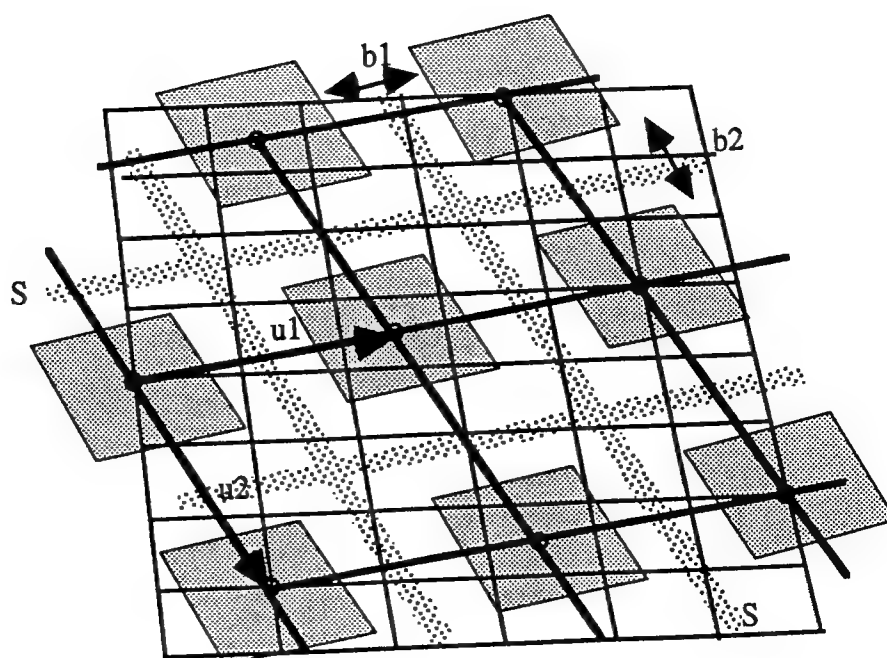


Figure 5.6: A schematic defining the parameters used in deriving the fraction of area relaxed. The vectors  $u_1$  and  $u_2$  define the O-lattice. Shaded areas are regions that have relaxed, and in between them are screw dislocations,  $S$ , of width  $b_1$  and  $b_2$ .

parameter  $n$ . The fitting parameter,  $n$ , is the number of Burger's vectors  $b_1'$  and  $b_2'$  that equal the core radius. The width of the core is assumed to be equal to  $b_1$  and  $b_2$ .

Another assumption in this derivation is that the grain boundary is symmetric. This means that the local flux of chains is the same for both crystals. Typically grain boundaries are asymmetrical which would result in a excess number of chains on one side of the interface. This density flux was discussed by Martin et al. (1991). An excess of chains would necessarily lead to chain ends at the boundary, decreasing the amount of connectivity.

### Results and Discussion

It might be expected that as the number of chains covalently bonded at the interface decreased, the mechanical strength of the interface would decrease. Figure 5.7 shows the tensile strength of a twist bicrystal grown by Liao (1994). Fitting the curve with the prediction based on O-lattice theory results in a value of  $n$  of 1.0. This is consistent with a local dislocation core since the tensile strength will be dependent on how many chains are covalently bonded through the interface. Screw dislocations, which make up twist boundaries, have an in plane strain field that is just the core. The core is one Burger's vector in radius, corresponding to a value of one for  $n$ .

Our derivation for  $f$  should also be appropriate for analysis of data for bicrystals in other material systems where relaxations at the interface effect the property measured. The critical current density for superconductive response as measured by Dimos et al. (1990) is shown in Figure 5.8. They measured three types of grain boundaries, (001) tilt, (100) tilt, and (100) twist bicrystals grown by epitaxy. An interesting result was that when plotted as a function of misorientation angle, the three sets of data lie on the same curve.



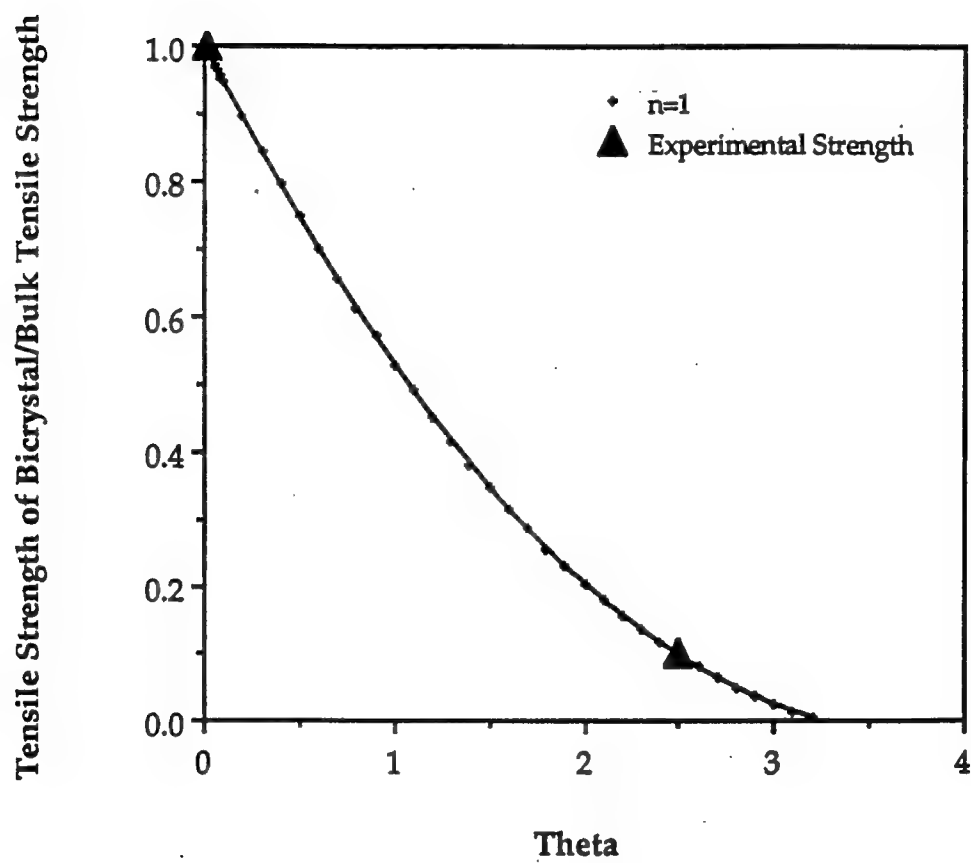


Figure 5.7: Mechanical strength data for polymer twist bicrystals (Liao, 1994) fitted using  $n=1.0$ .

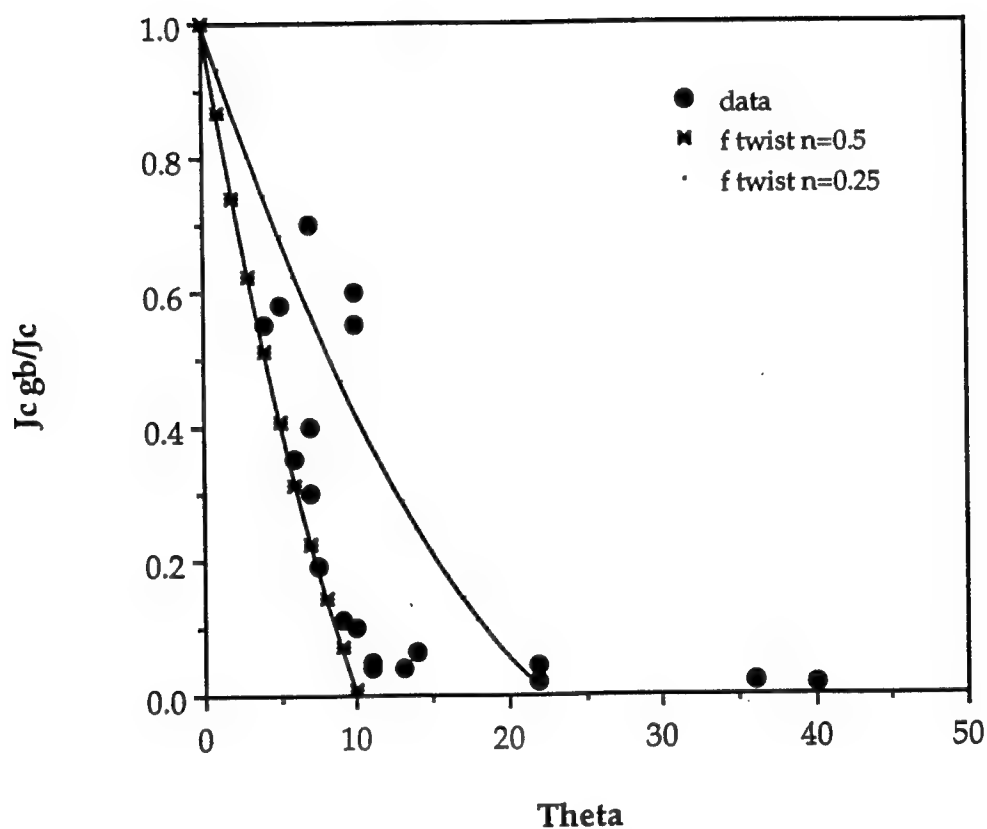


Figure 5.8: Data from the bicrystal experiments by Dimos, et al. (1990) showing the decrease of the critical current for onset of superconductivity through a grain boundary (normalized to the bulk crystal) as a function of grain boundary misorientation. Overlapped is the prediction by an extension of O-lattice theory to describe the expected behavior. The results are bracketed by curves predicting that the width of disorder that influences this property at the screw dislocation is 0.5 to one Burger's vector

It suggests that our twist solution may be used as a first order approximation to model the results obtained by Liao for tilt DCHD monomer bicrystals.

Using the twist solution to fit the data by Dimos, values for  $n$  of 0.25 and 0.5 were needed to bracket the data. There is a transition in the response at high angles which could not be fitted by the O-lattice solutions. This transition in behavior was discussed by Dimos as a transition from strong coupling to weak link behavior. Above about  $10^\circ$  the boundary becomes a high angle boundary where the dislocations are no longer discrete and the core regions overlap. After  $10^\circ$  in misorientation the response levels out to a plateau in value. This evidently corresponds to the response for disordered material. The modified O-lattice theory correctly models the behavior at low angles where the dislocations are still expected to be discrete. The fitting suggests that the core radius which effects the superconductive response is 0.50 of the Burger's vector for this particular type of dislocation.

Using the modified O-lattice theory the photoconductive response of DCHD polymer tilt bicrystals at an electric field strength of  $10^4$  V/cm, as measured by Liao (1994), was modeled using  $n=0.30$ , shown in Figure 5.9. Similar to the case of the oxide superconductivity, the photoconductive response decreases rapidly at low angles and then plateaus off above approximately  $5^\circ$ . The transition to high angle behavior in this system can be rationalized as the transition from charge carrier transport dominated by conduction along the backbone to hopping between the chains. The behavior of the mechanical strength did not have a plateau as was seen when measuring conductive properties. This is consistent since when the cores of the dislocations would begin to overlap, there would be no covalent bonding at the interface and the strength would be equal to the much weaker van der Waals forces. Our modification of O-lattice theory to predict

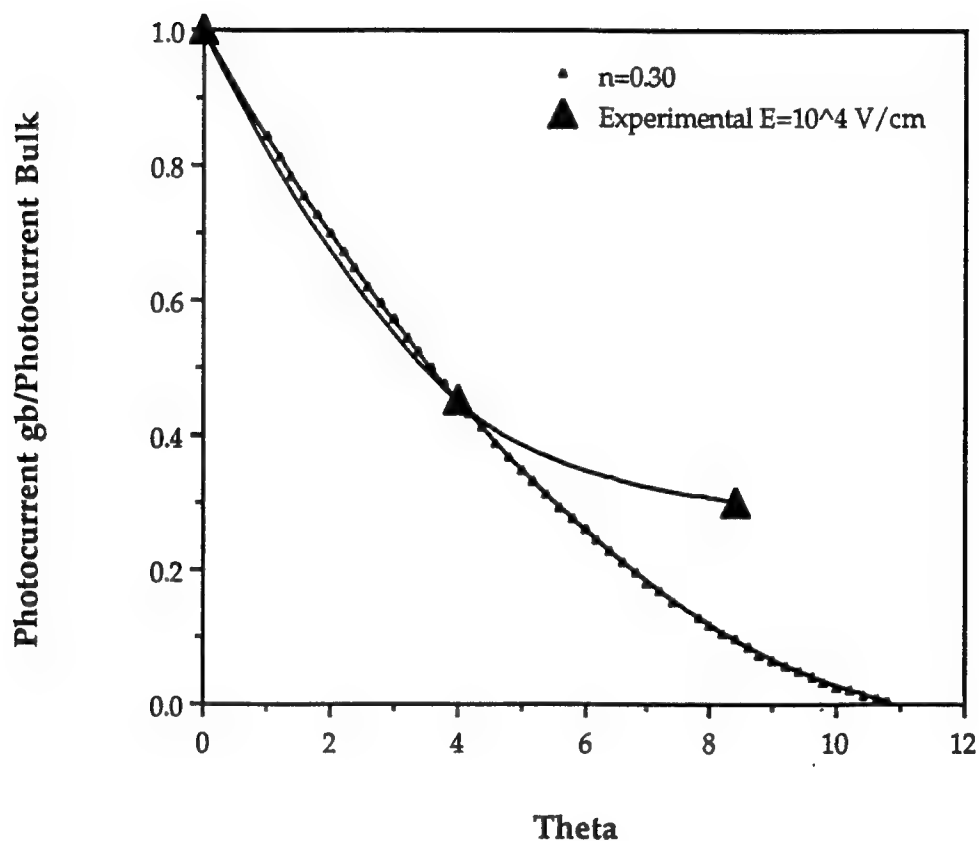


Figure 5.9: Experimental photocurrent as a function of grain boundary misorientation for DCHD polymer bicrystals (Liao, 1994). The data follows the trend predicted by polymerization retardation on the basis of O-lattice theory. The width of the lines of unpolymerized screw dislocations is fitted to be half the Burger's vector.

properties is based on the assumption that relaxations occur at O-lattice points. Therefore it assumes discrete dislocations similar to Frank's dislocation model of grain boundaries. Because of this, it is mostly appropriate to describe low angle behavior property decreases at low angle, whereas Frank's relationship formulated in terms of  $f$  is linear in  $\theta$ :

$$f = 1 - 2n\theta$$

Fitting of the experimental data reveals that relaxations at the grain boundary are large enough to allow for polymerization through the boundary. Small values of the disordered region, below one Burger's vector, were found. This is consistent with results from Chapter IV which measured the strain fields around chain end edge dislocations. It also showed that the deformation was localized around the dislocation. The experimental results suggest that although the symmetry of the DCHD system produces very high dislocation densities at extremely small misorientation angles, significant relaxations occur at the interface. If these relaxations did not occur, it would be expected that a slight misorientation (less than one degree) would quickly reduce the transport properties and mechanical strength to zero.

### Conclusions

O-lattice theory was used to describe the geometry of the monomer bicrystal interface for ACI twist boundaries where the boundary plane is flat and has no tilt component. The predicted O-lattice was used to formulate the fraction of interfacial area where polymerization could take place between the two monomer grains. This fraction was equated to the density of chains covalently bonded across the interface which in turn is proportional to

properties that are backbone dependent. Measurements of the tensile strength and photoconductive response for experimental bicrystals (Liao, 1994) were analyzed with this formalism. A value of  $n=1.0$  was needed to model the tensile strength while a value of  $n=0.30$  predicted the photoconductive response. The shape of the photoconductive response curve was qualitatively matched at low angles. There appeared to be a transition in the mechanism of response from conduction along the backbone to hopping between chains between  $3^\circ$  and  $5^\circ$ . Our predictions using O-lattice theory are valid for small angles where the separation between dislocations is larger than the core.

The behavior of the mechanical strength and photoconductive response was found to vary greatly with dislocation density. The rate of decrease of the macroscopic properties was able to predict the extent of relaxation at the interface. The relaxations predicted by fitting the experimental data qualitatively matched the results in Chapter IV. Disorder is localized around the core of chain breaking dislocations.

Future work could expand this formalism to include tilt grain boundaries, the roughness at the interface or chain flux arguments based on asymmetrical boundary orientations.

## **CHAPTER VI**

### **HIGH RESOLUTION ELECTRON MICROSCOPY AS A FUNCTION OF THICKNESS ON WEDGE SHAPED POLYMER SAMPLES**

#### **Introduction**

High resolution electron imaging of atomic planes provides a means to investigate the local disorder around defects in crystalline or liquid-crystalline (Voigt-Martin et al., 1992) materials. A limitation of HREM is that the interpretation of image contrast in terms of the original structure can be complicated. In order to correctly interpret the details of high resolution electron microscopy images of defects a range of microscope and sample parameter needs to be known. This study investigates the effects of crystal thickness on image formation in polymer samples and compares experimentally obtained results to theoretical predictions on the basis of dynamical electron scattering theory.

An understanding of the relationship between image contrast and structure can facilitate defect analysis by providing a means of analyzing the local defect area. Ideally, the image would be a direct mapping of the sample's projected electron potential. Atoms would appear as black spots and the contrast of the image would be linearly related to the amount of material scattering in the sample. In practice the interaction of electrons with matter is a multiple scattering process coupled with the response of the objective lens being non-uniform over all frequencies. This results in the exit surface wave

carrying complex information about the material structure which is non-uniformly transferred to the image plane. Studies of image formation as a function of thickness are necessary since areas sufficiently thick as to preserve the bulk structure, such as dislocation cores, provide complex multiple scattering events and thus the complicate analysis.

Image intensities in high resolution electron microscopy are dominated by phase contrast mechanisms in which the amplitudes and phases of the incident electron beam are changed from the interaction with the electron potential of the sample. In sufficiently thin and low atomic number samples, the material acts as a weak phase object and the kinematic theory of scattering is approached. Kinematic theory predicts a nearly unscattered central beam and a single scattering event for each Bragg beam and thus an easily interpretable image, provided one has a perfect microscope with an ideal lens. Polymer materials have low atomic number as compared to metals, but as will be shown in the discussion, kinematic approximations still do not predict the experimental results. Also, our interest is in thicker sections for defect analysis, for which dynamical electron scattering is even more important.

The multiple interactions of the beam with the sample can be described by dynamical scattering theory. Figure 6.1 is a schematic which models the processes in an electron microscope. The incident electron beam,  $\psi_0$ , interacts with the sample's potential,  $\phi_0(x_1, x_2, x_3, t)$ , to produce an exit wave,  $\psi_x$ , whose amplitude and phase are changed according to the strong phase object approximation, SPOA:

$$\psi_x = \psi_0 \exp(-i\sigma\phi(x_1, x_2))$$



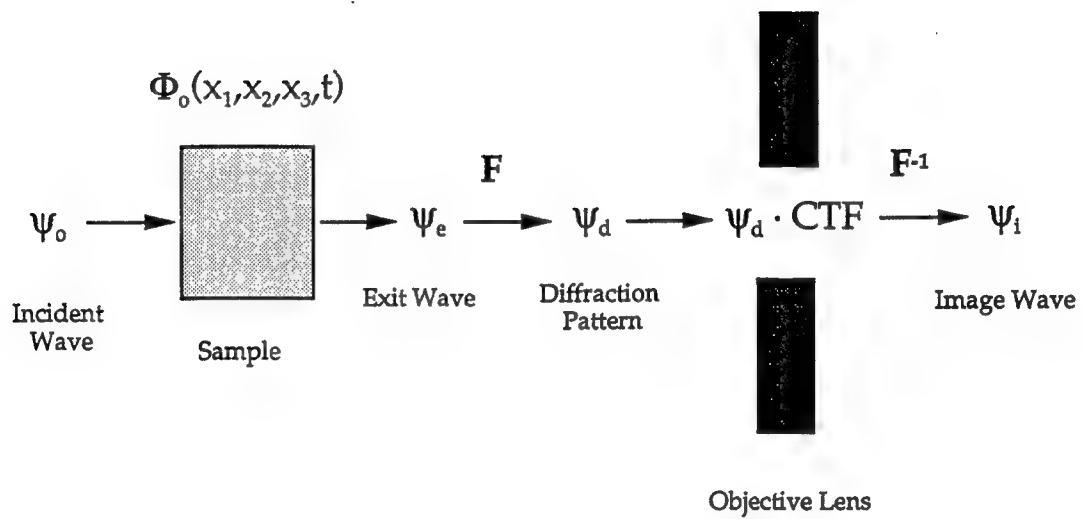


Figure 6.1: Schematic of the general processes in an electron microscope to form a high resolution image.  $F$  and  $F^{-1}$  are the Fourier transform and inverse Fourier transform operations.

where  $\sigma$  is the scattering efficiency of an electron and  $\phi_0(x_1, x_2)$  is the total projection of the sample potential in the  $x_3$  (beam) direction. The exit wave is then Fourier transformed to  $\psi_d$ , which may be collected as the diffraction pattern,  $\psi_d \psi_d^*$ .  $\psi_d$  is then operated on by the contrast transfer function,  $CTF$ , of the objective lens and inverse Fourier transformed to form an image,  $\psi_i$ .

The contrast transfer function of the microscope is given by:

$$CTF = \exp(i\chi(k, \Delta f)) D_1(k) D_2(k, \Delta f) D_3(k, M) A(k)$$

where  $D_1$ ,  $D_2$ , and  $D_3$  are damping terms due to focus spread, beam divergence, and film response (Martin, 1990).  $A(k)$  is the function which takes into account the objective aperture. The exponential term contains the variation of the phase change,  $\chi(k)$ , imposed by the microscope parameters of defocus ( $\Delta f$ ), wavelength, and spherical aberration coefficient ( $C_s$ ). The usual aim is to have the  $CTF$  uniform over the largest range of spatial frequencies possible. The primary control the user has over the  $CTF$  is the selection of objective focus conditions. Two special focus conditions are the Gaussian focus,  $\Delta f_g$ , and Scherzer focus,  $\Delta f_s$ :

$$\Delta f_g = -0.3(C_s \lambda)^{1/2}$$

$$\Delta f_s = -1.2(C_s \lambda)^{1/2}$$

Gaussian focus (Buseck, et al., 1988) is the value which best cancels out the contrast-producing effect of the spherical aberration. Scherzer focus gives a value of -1 for  $\sin\chi(k)$  for the largest number of spatial frequencies and thus

allows the most straightforward interpretation of the structure over the broadest range of spacings.

What is observed in an HREM image is  $\varphi_i \varphi_i^*$  the square of the complex  $\varphi_i$  in the form of optical density on photographic film. The intensity distribution,  $I(r) = \varphi_i(r) \varphi_i^*(r)$ , in the image can be given as a function of the amplitudes and phases of the transmitted and diffracted beams of the exit wave:  $U_0$ ,  $U_g$ ,  $\theta_0$ , and  $\theta_g$  respectively (Glaisher et al., 1992).

$$\begin{aligned}
 I(r) = & \{U_0^2 + 2 \sum_{g>0} U_g^2\}_1 + \{4 \sum_{g>0} U_g U_0 \cos(\theta_g - \theta_0 + \chi(g)) \cos(2\pi \mathbf{g} \cdot \mathbf{r})\}_2 \\
 & + \{2 \sum_{g>0} U_g^2 \cos(4\pi \mathbf{g} \cdot \mathbf{r})\}_3 \\
 & + \{8 \sum_{|g|=|g'|} U_g^2 \cos(2\pi \mathbf{g} \cdot \mathbf{r}) \cos(2\pi \mathbf{g}' \cdot \mathbf{r})\}_4 \\
 & + \{8 \sum_{|g|>|g'|} U_g U_{g'} \cos(\theta_g - \theta_{g'} + \chi(g) - \chi(g')) \cos(2\pi \mathbf{g} \cdot \mathbf{r}) \cos(2\pi \mathbf{g}' \cdot \mathbf{r})\}_5
 \end{aligned}$$

The influence of the contrast transfer function of the objective lens is imposed by the phase change  $\chi(g)$ , restricting the summations to only the reflections within the objective lens aperture. Here  $k$ , the wave vector, is replaced by  $g$ , which expresses the Bragg scattered wave (Hirsch et al., 1965). The first term of the expression determines the background intensity of the image while the rest of the terms describe the cosine fringes of various periodicities and amplitudes which constructively and destructively interfere to produce the local intensity modulation in the image.

The above formalisms define the behavior of the beam-sample interactions and the influence of the microscope parameters on the final image. In order to understand the intensities of the images, simulations from a postulated structure using dynamic beam-sample interactions is needed. Theoretical developments by several researchers have given methods to

calculate these interactions based on Schrodinger's time independent equations (ignoring backscattering events). The most widely used of these approaches is the Multislice algorithm developed by Cowley and Moodie in 1957 which requires the least amount of computer memory and time to calculate (Glaisher et al., 1992).

The multislice approach envisions the sample divided into a number of thin slices perpendicular to the beam direction so that the slices act as two-dimensional phase objects (Figure 6.2). The sample potential in each slice is projected to a plane in the center of the slice and used to calculate the phase change imposed on the incident wave. The wave is propagated from one slice to the next by Fresnel diffraction in a vacuum. In the limit of infinite slices of the sample, it has been shown that this method is an exact representation of the dynamical scattering process (Spence, 1988). A slice thickness of one unit cell is sufficiently accurate to simulate experimental results for small unit cell materials less than 0.6 nm (Spence, 1988).

The procedure often used to interpret HREM images in the past has been to simulate a series of images using the above approaches based on a model structure of the material and compare them to the experimental images in an iterative way until a good match is found (Glaisher et al., 1992). This procedure is difficult because of the large number of instrument and sample parameters such as beam tilt, crystal tilt, sample thickness, and defocus which can drastically change the image, especially in small unit cell materials. Attempts to limit the amount of simulation iterations have been to focus on particular sample and microscope conditions which lead to fewer ambiguities (Spence, et al., 1977, Glaisher and Spargo, 1985, and Desseaux, et al., 1977). The conditions used are a wedge shaped sample with a nearly constant thickness variation, a "tuned" voltage, and a restricted number of beams for imaging.

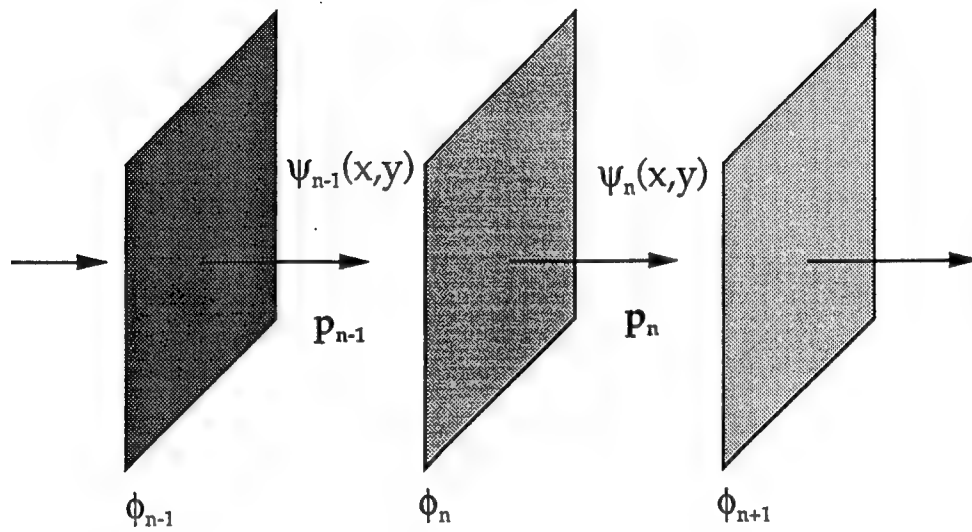


Figure 6.2: The multislice process.

These three conditions lead to the Pendellosung effect where, due to the strong reinforcement of scattering into the Bragg beams, a series of unique images appear that are independent of defocus (Spence, 1988).

The effect of this reinforced scattering is to oscillate the amplitudes of the transmitted and diffracted beams alternately to maximums and a minimum value close to zero. When these oscillations are sinusoidal they allow a dynamical extinction distance (thickness),  $\xi_g$ , to be determined where the amplitude of the scattered beam is zero and so the image intensity becomes a uniform background (Spence, 1988). Two other thicknesses can be defined, one at  $\xi_g/4$  where the amplitudes of the scattered and (000) beams are equal providing the highest intensity of the scattered frequency, and  $\xi_g/2$  where the (000) beam amplitude is zero giving rise to half spacing fringes. Because they are independent of the contrast transfer function, these thicknesses should provide an unambiguous thickness measurement for that portion of the crystal which in turn would give the slope of the wedge and a means to calibrate the rest of the images in between. Having such a means to calibrate the thickness in a region near a dislocation core would significantly reduce the amount of simulations required for a detailed defect model refinement.

Because the interactions of the beam and sample are voltage dependent, it follows that the magnitude of this effect in the image will also be voltage dependent. Glaisher and Spargo (1985) detailed a series of computer simulations which showed that for every sample orientation there may be a specific "tuned" voltage for the Pendellosung effect. The requirement is that the amplitude of the beams oscillate in some manner and the minimum is reduced close to zero. They showed for diamond (111) and silicon (111) that tuned voltages were possible at 825 kV and 88 kV

respectively, whereas for germanium (111) it wasn't apparent. As is evident, in order for this process to be used in practice, it is necessary that the material exhibits this effect within the range of achievable voltages in conventional electron microscopes (~50 kV - 1 MeV). Most of the work to date has been performed on diamond-cubic structures.

Although Glaisher and Spargo predicted that the Pendellosüing effect would be absent in germanium in the [011] orientation, previous studies by Spence, et al. (1977) and Desseaux, et al. (1977) both show experimental and simulated five beam images where extinctions and half-spacing fringes are apparent. At the operating voltage of 100 kV the (000) beam amplitude is calculated to decrease by as much as 80% from its maximum transmitted value. From the experimental evidence, it appears that only a significant decrease in the (000) amplitude is necessary to produce a recognizable half period image. The phase differences between the scattered and transmitted beam also need to be taken into account for extinction of the fringes and may contribute to seeing the Pendellosüing extinction in germanium.

The existence of a "tuned" voltage which maximizes the Pendellosüing effect is a strong argument for modifying the "standard" operating voltage of a microscope. Most microscopes are built for optimum performance at a specified voltage. By plotting the contrast of an image versus operating voltage using the multislice technique, parameters to operate a microscope to obtain optimal images of a material could be determined. This could be especially useful for imaging polymer materials, where contrast is low to begin with because of the low atomic weight of the atoms.

An excellent example of a silicon wedge is shown in Spence (1988) taken at 100 kV which is close to its tuned voltage of 88 kV. As the thickness of the wedge increases the five beam image varies as predicted by the

simulated Pendellosung plot. Two deficiencies of the aforementioned studies are apparent, one is to quantify the contrast in the images. The other is to use an independent method to calibrate the thickness of the samples and thus validate the predictions of the Pendellosung method. At the time many of these studies were undertaken the state of the art did not include techniques now available such as scanning probe microscopy (SPM) and digital image analysis. Thickness measurements were possible by convergent beam electron microscopy but specimens thicker than the wedges are needed to perform it accurately. Here, we examine the nature of HREM images near the edges of DCHD polydiacetylene droplets on surfaces. This study measures the contrast of the experimental images, relates it to the simulated images, and uses scanning probe microscopy to quantify the thickness of experimental samples for an independent thickness calibration.

## **Experimental**

### **Sample Preparation**

DCHD diacetylene droplets were formed from chloroform solution, as discussed previously (Wilson and Martin, 1992), on carbon coated mica for preparation as HREM samples and SPM samples. SPM samples were left on the mica substrate, while HREM samples were floated on deionized water for collection with copper grids.

### **TEM Operation and Calibration**

HREM images of droplet edges were obtained on a JEOL 4000 EX at 400 kV using low dose imaging conditions (Wilson and Martin, 1992). The



procedure was to focus on the amorphous carbon at the edge of a droplet and underfocus to Gaussian focus (-11 nm).

The spherical aberration constant of our microscope was determined using the procedures described in Spence (1988). The method was to take a series of double exposed micrographs in bright field and electron diffraction with the beam both aligned down the optic axis and tilted. A holey carbon film with gold evaporated onto the surface was used to determine the beam tilt and in-focus displacement of the image. The spherical aberration constant,  $C_s$ , can be determined from the image displacement as:

$$C_s = d / M \Theta^3$$

where  $d$  is the displacement of the image,  $M$  is the magnification and  $\Theta$  is the tilt of the beam determined from the double exposed diffraction patterns via:

$$\Theta = \frac{r}{r_o} \frac{\lambda}{a_o} (h^2 + k^2 + l^2)^{1/2}$$

where  $a_o$  is the unit-cell constant (0.408 nm for gold),  $r_o$  is the measured distance between the central beam and the diffraction indices (h k l), and  $r$  is the measured distance between the two central beams on the micrograph. The (313) diffraction ring was used to tilt the beam off the optic axis, which resulted in a measured spherical aberration constant of  $0.82 \pm 0.2$  mm.

### SPM Operation

The height profiles of poly(DCHD) droplets were measured using a Digital Nanoscope III. A J head was used in tapping mode. Droplets from 1.5  $\mu\text{m}$  to 3.5  $\mu\text{m}$  in diameter were recorded. The height as a function of distance from the edge was determined from cross-sections of the image profile. The data was then normalized to the radius of a reference sphere determined by the diameter and angle of contact of the droplets. This plot was used to calculate the height profile of the droplets from HREM images.

### Digital Image Analysis

HREM images near the edge of droplets were digitally analyzed by measuring the amplitude of the relevant frequencies in the fast Fourier transform of the images. The procedure was to digitize the necessary area of the negative using a SCION Frame grabber and capturing the image using NIH IMAGE 1.35 FFT. The image was then analyzed using ImagNSpect (Davilla and Kopf, 1993). A slit was constructed 16 pixels wide and 256 pixels high to select areas for Fourier transforming. The slit was moved along the image starting from the area just preceding the edge of the droplet and continuing along into the droplet center.

The chains were oriented perpendicular to the edge of the droplet with the (010) plane in the plane of the substrate. The imaging conditions produced 1.2 nm fringes parallel to the chain axis which corresponded to the (010) planes. A FFT was calculated at every slit step and the amplitudes of the background, 1.2 nm, and 0.6 nm frequencies in the image were recorded as a function of depth into the droplet.

HREM fringes were calibrated with HREM images of catalyze crystals (8.75 and 6.85 nm spacings) at the same magnification by taking the FFT of both digitized images using NIH IMAGE 1.35 FFT.

### Simulation of HREM Images

Multislice calculations were performed using the high resolution microscopy module of CERIU<sup>2</sup> (Molecular Simulations Inc., 1994) and the X-ray determined structure of poly(DCHD) (Apgar and Yee, 1978). The unit cell is monoclinic, space group  $P2_1/c$  with parameters  $a=1.739$  nm,  $b=1.289$  nm,  $c=0.490$  nm, and  $\gamma=108.3^\circ$ . In order to simulate the 1.2 nm (010) fringes, the beam was aligned down the [100] zone axis. The minimum number of beams, defined by the condenser aperture size, in the multislice calculation to predict the Pendellosüing plot was  $0.25 \text{ \AA}^{-1}$ . Dividing the unit cell into five slices of approximate thickness 0.35 nm for the calculation of the projected potential was found to be the minimum needed for an accurate simulation. Pendellosüing plots were calculated for the transmitted beam and the (010) beam at a series of voltages from 100 kV to 800 kV to determine the "tuned" voltage needed to maximize the two beam imaging case. All images and Pendellosüing plots were calculated from zero to 250 nm in thickness. The microscope parameters used to simulate images are listed in Table 6.1.

The minimum, maximum, and average image intensities as calculated by CERIU<sup>2</sup> were recorded at Gaussian focus (-11.0 nm) as a function of thickness. The image was calculated every two unit cells in thickness. Detection of the periodicities in the image and evident contrast mechanism (tunnel vs. column) was aided by displaying the unit cell image three times in each direction perpendicular to the beam.

Table 6.1

Microscope parameters used for multislice calculations

Voltage	400 kV
$C_s$	0.82 mm
Aperture Radius	$0.083 \text{ \AA}^{-1}$
Defocus	-11.0 nm

The sensitivity of the image to microscope parameters was also explored, most notably the sensitivity to  $C_s$ . Images were calculated from  $C_s = 0.7$  to 2.5 mm in 0.1 mm steps. The image periodicity and image intensities remained constant within 10%.

## Results and Discussion

The "tuned" voltage for the Pendellosüing effect was found to be approximately 400 kV for (000) and (010) beams of DCHD in the [100] zone axis orientation. Figure 6.3 shows Pendellosüing plots of the amplitude calculated in the range of available microscopes, 100 - 800 kV. A full sized plot at 400 kV is shown in Figure 6.4. The oscillations of the Pendellosüing plot are not sinusoidal as seen in some small unit cell materials (Glaisher, et al. 1985) and so the dynamical extinction distance definition,  $\xi_g$ , (Spence, 1988) and resulting periodicity of thickness images,  $\xi_g/4$ ,  $\xi_g/2$ , etc., are over simplifications in this case. What is apparent is a minimum in amplitude of the (000) beam at thicknesses of 100 and 175 nm and of the (010) beam at 45 and 225 nm. Two crossovers of the amplitudes of the (000) and (010) are found at 75 and 200 nm.

Explanations of what is expected in the image at these thicknesses can be found by looking at the equations for image intensity (Glaisher, et al. 1992) as a function of position on the negative. The equation for image intensity,  $I(r)$ , shown in the introduction of HREM theory can be applied to the imaging conditions used here. For the imaging of 1.2 nm fringes only the (010) and (000) beam are needed, giving a two-beam imaging condition. This eliminates the terms four and five from the equation of image intensity resulting in:

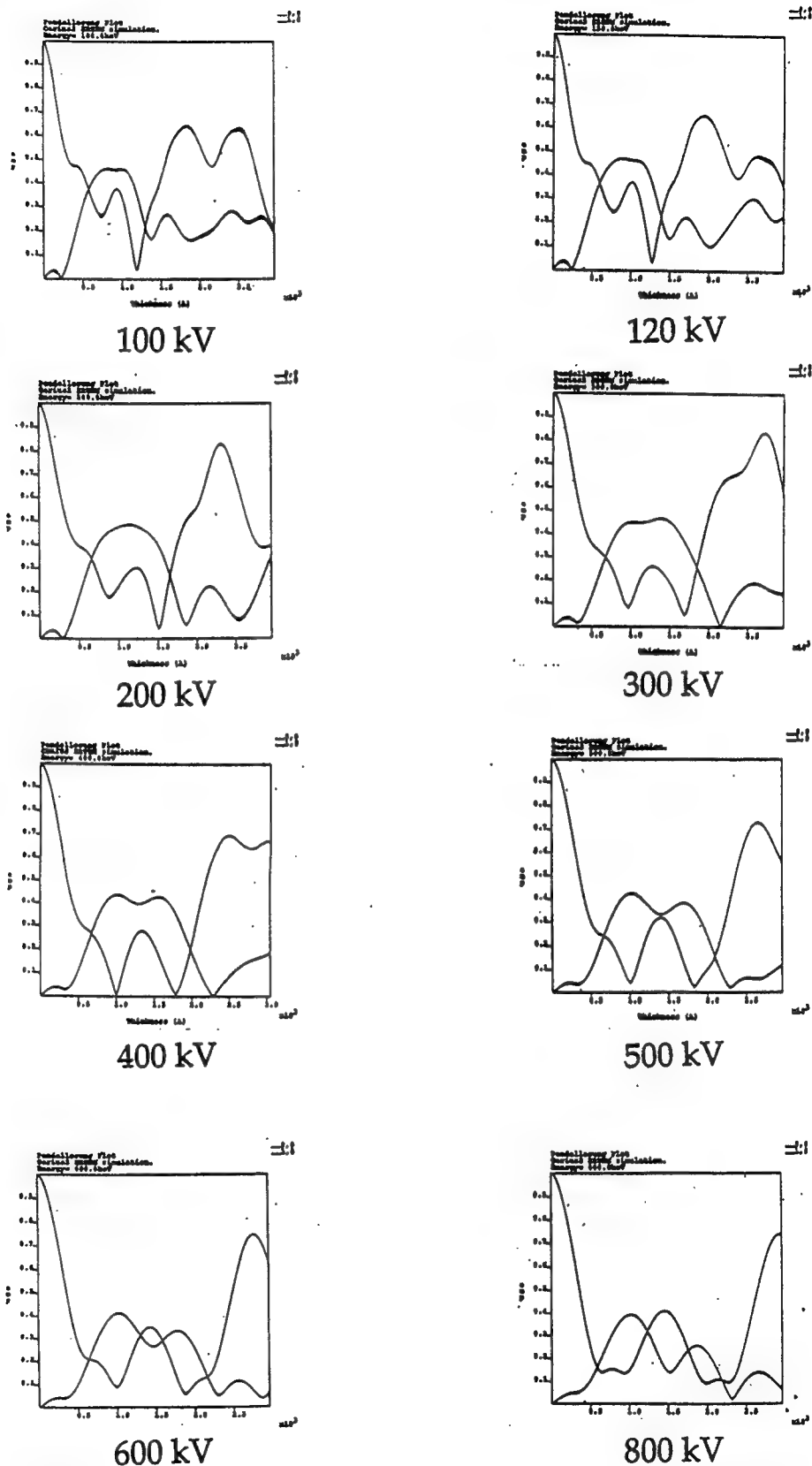
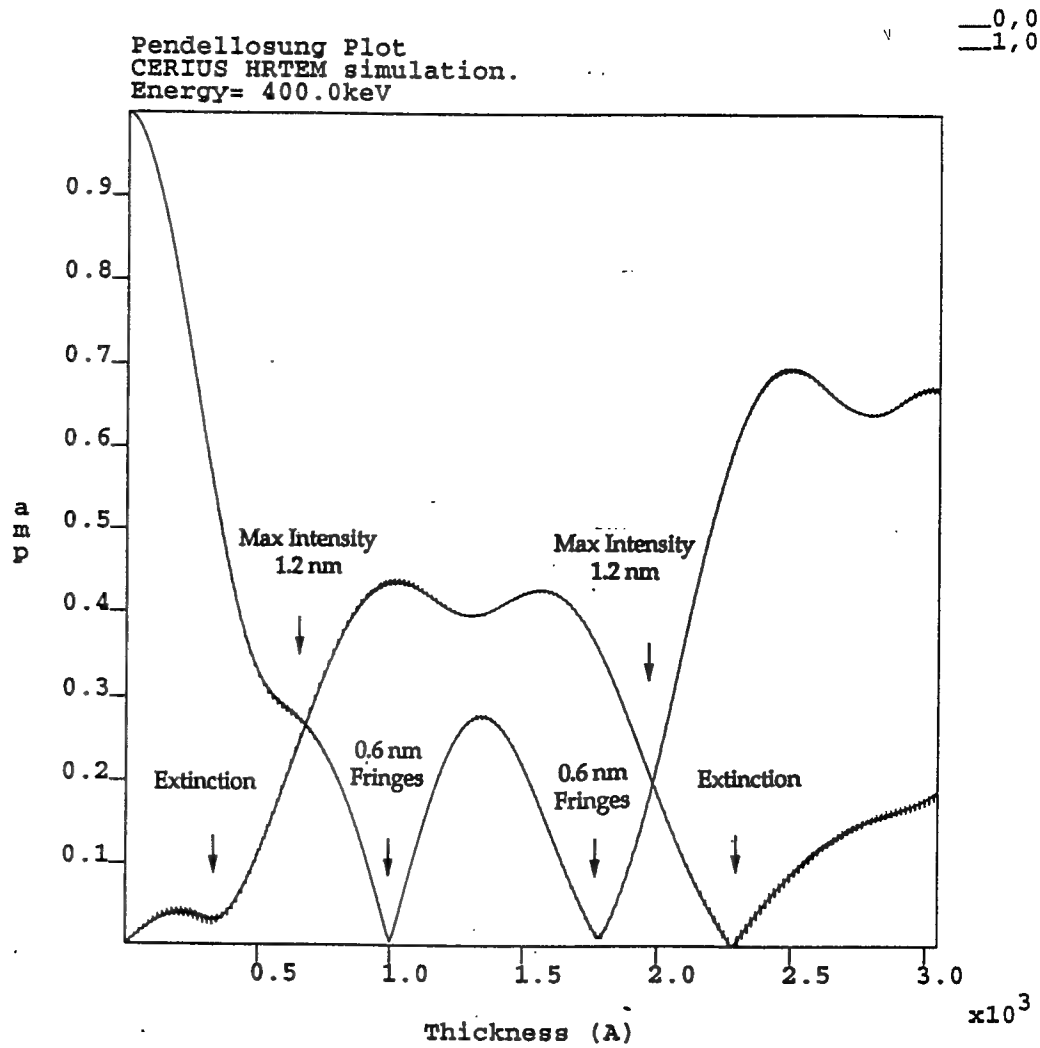


Figure 6.3: Pendellosing plots for 100-800 kV for the (000) and (010) beams. The Pendellosing effect is maximum at  $400 \pm 10$  kV.



HRM Pendellosung v1

Figure 6.4: Pendellosung plot for 400 kV. Several distinct thicknesses are noted where images independent of microscope parameters are located.

$$I(r) = \{U_0^2 + 2 \sum_{g>0} U_g^2\}_1 + \{4 \sum_{g>0} U_g U_0 \cos(\theta_g - \theta_0 + \chi(g)) \cos(2\pi g \cdot r)\}_2 \\ + \{2 \sum_{g>0} U_g^2 \cos(4\pi g \cdot r)\}_3$$

We are interested in two regions of the unit cell (see Figure 6.5), A and B, where A is the region where there is no electron potential and B is the region of high electron potential (the polymer chain). By summation over the diffracted beams used this reduces the equation to:

$$I\left(\begin{smallmatrix} a \\ b \end{smallmatrix}\right) = \{U_0^2 + 2U_{010}^2\} + \{4U_{010}U_0 \cos(\theta_{010} - \theta_0 + \chi_{010})\} + \{2U_{010}^2\}$$

Where  $U_0$ ,  $U_{010}$  are the amplitudes and  $\theta_0$  and  $\theta_{010}$  are the phases of the (000) and (010) beams.  $\chi_{010}$  is the phase change imposed by the objective lens. Two limiting cases exist. When  $U_{010}$  is zero then the intensity is:

$$I\left(\begin{smallmatrix} a \\ b \end{smallmatrix}\right) = U_0^2$$

and the A and B sites acquire an intensity level similar to the background which results in an image of uniform low contrast detail, an extinction of fringes. The second case is when  $U_0$  approaches zero, then both A and B sites have the same intensity:

$$I\left(\begin{smallmatrix} a \\ b \end{smallmatrix}\right) = 4U_{010}^2$$

resulting in the appearance of fringes with half the spacing of the (010) beam, or 0.6 nm. This results from the interaction of the (010) and the  $(0\bar{1}0)$



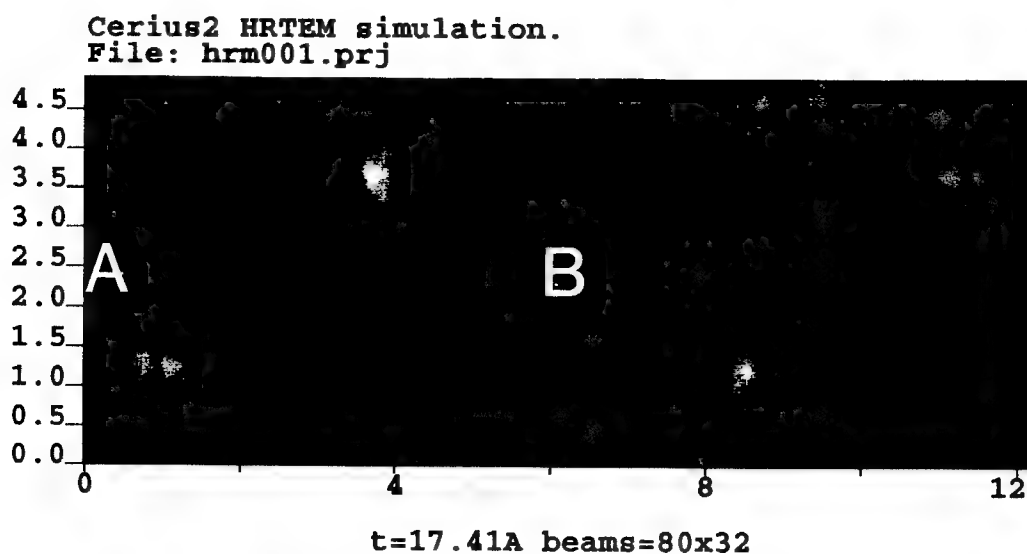


Figure 6.5: Projected potential of poly(DCHD) looking down the [100] zone axis. Light regions are areas of high electron potential (the atoms) denoted by B, while A represents an area of no electron potential. When the intensity is equal at both A and B, half spacing fringes (0.6 nm) appear.

beams. When  $U_0$  is equal to  $U_{010}$  then the intensity of the fringes is a maximum. Figure 6.6 is a schematic of a wedge illustrating these different scattering events as a function of thickness. Table 6.2 summarizes the unique thicknesses and their image appearances.

Simulated images using the imaging parameters that were used to obtain our experimental results can be monitored for the image periodicities and characteristics predicted from the Pendellosüing plot. Table 6.3 summarizes the results and includes the type of fringe contrast seen, tunnel or column. Column contrast shows black at regions of high electron potential (atoms) and conversely white in electron poor regions. In tunnel contrast this situation is reversed. The image calculation at each thickness also provides the maximum, minimum and mean intensities, in arbitrary units, of the entire image. Figure 6.7 is a plot of contrast in the simulated image as a function of thickness. Contrast is defined as (Spence et al., 1977):

$$\text{Image Contrast} = \frac{(\text{Maximum image intensity} - \text{Minimum image intensity})}{\text{Mean image intensity}}$$

Ideally it should be possible to obtain both HREM and SPM images of a droplet edge, but experimentally this proved to be difficult. HREM of organic samples is limited by the radiation damage susceptibility of the spacing of interest. Also in order to image the (010) fringes, the crystal has to be in the correct zone axis orientation. As shown in Wilson and Martin (1992) DCHD droplets are crystallographically textured which limits the fraction of the droplet in the correct orientation for imaging. Several images showing the Pendellosüing effect of contrast reversal, half-spacing fringes, and extinction

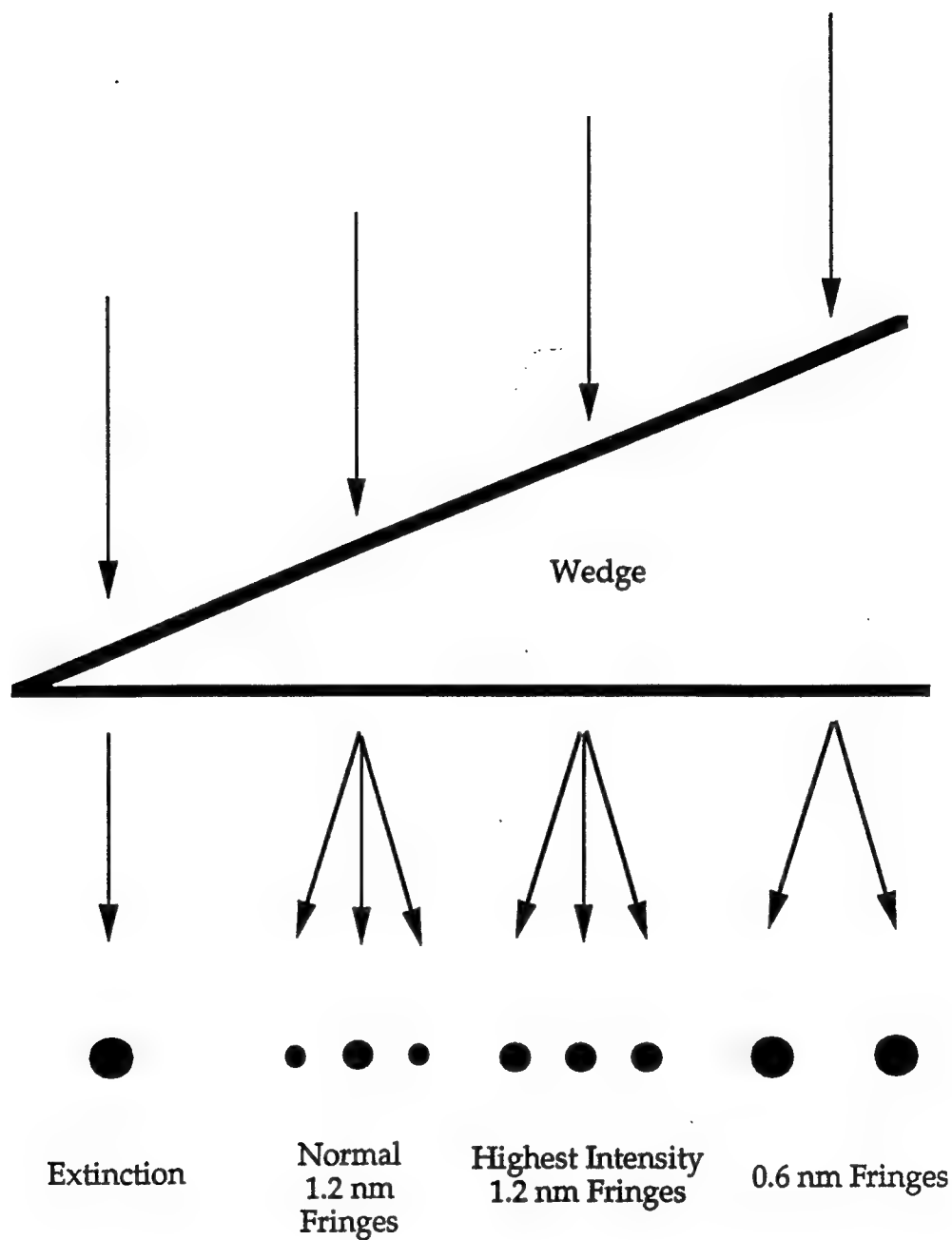


Figure 6.6: Schematic of the scattered electron beams as a function of thickness. When the transmitted beam and two diffracted beams are present, 1.2 nm fringes are produced. If the transmitted beam is not present, the interaction of the two diffracted beams produce half spacing fringes.

Table 6.2

Unique image thicknesses predicted from Pendellosüing plot

<u>Thickness (nm)</u>	<u>Image Appearance</u>
45	Extinction
75	Max Intensity (1.2 nm)
100	0.6 nm fringes
175	0.6 nm fringes
200	Max Intensity (1.2 nm)
225	Extinction

Table 6.3

**Contrast type as a function of thickness from computer simulated images**

<u>Thickness (nm)</u>	<u>Contrast</u>
0-3.5	column
7.0-41.7	tunnel
45.3-94.0	column
97.5-104.5	half spacing
107.9-170.6	tunnel
174.1-181.0	half spacing
184.5-226.3	column
229.7-247.2	tunnel

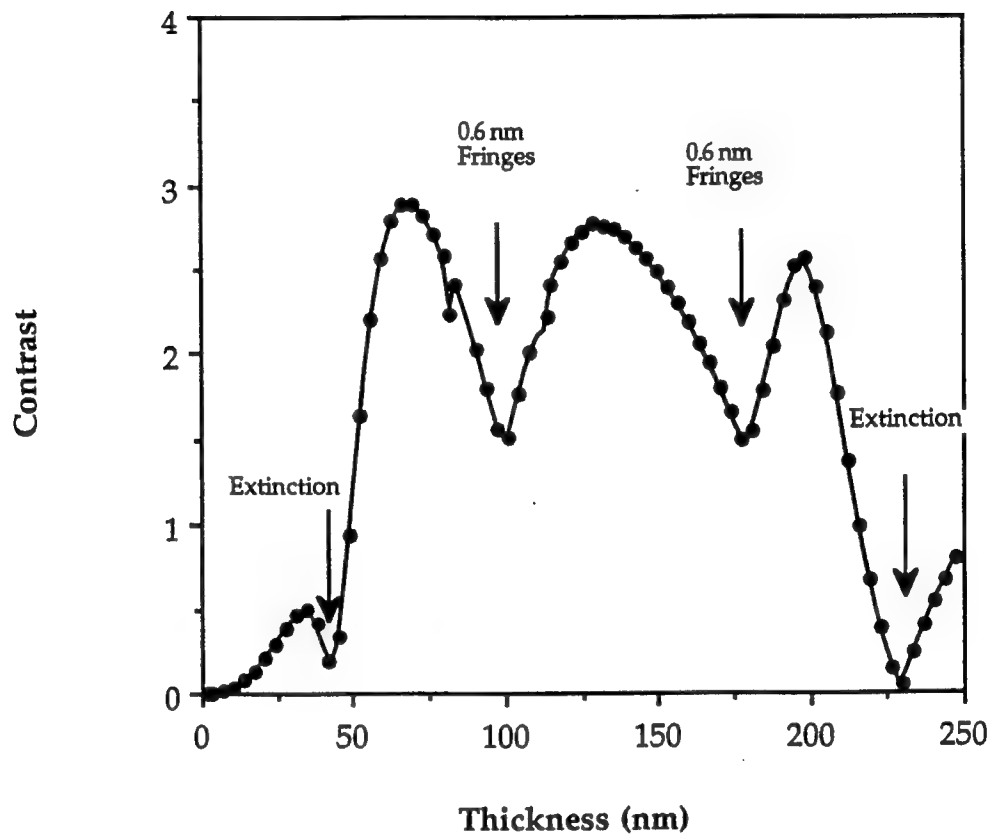


Figure 6.7: Contrast in the multislice simulated images as a function of thickness for Gaussian focus. Unique thickness images are indicated.

were found. An example is shown in Figure 6.8. Images where the fringes are seen to begin at the edge of the droplet and continue into the bulk provide a calibration of zero thickness at the edge. Not all images of droplets showed fringes near the edge due to disorder inherent in polymer samples or a tilt of the crystal out of the zone axis orientation. Furthermore, as the thickness of the droplet increased the same reasons would cause loss of fringe contrast.

Figure 6.8 shows an edge of a  $2.2 \pm 0.5 \mu\text{m}$  diameter droplet with 1.2 nm fringes corresponding to the (010) planes perpendicular to the edge. Digitizing the image and performing local fast Fourier transforms as a function of depth into the droplet allowed the contrast of the image to be quantified. The amplitudes in the FFT of the image periodicities were monitored. A plot of the amplitude of the transmitted beam, 1.2 nm, and 0.6 nm image periodicities as a function of distance is shown in figure 6.9. The location of special images are also pointed out in the graph. Table 6.4 lists the appearances of the image as a function of depth. Two reversals of contrast of the (010) fringes are seen in the image, but we can not positively assess whether the contrast is of tunnel or column type independent of image simulations. Based on these simulations, the contrast in the wedge before the first extinction should be of tunnel type. Also listed is the thickness for each image predicted from examination of the Pendellosüing plot and theoretical image contrast calculated using the multislice method.

The first extinction seen at a distance from the edge of 46.6 nm is not correctly predicted by kinematic theory where the extinction distance is:

$$\xi_{\text{ek}} = \frac{\pi V_c \cos \theta}{\lambda F_s}$$

**Figure 6.8: HREM image of a poly(DCHD) droplet edge where the 1.2 nm fringes correspond to the (010) chain axis. The thickness of the droplet increases from top to bottom. An extinction of the fringes and 0.6 nm periodicity is seen in the micrograph. Between these images the contrast of the fringes reverses.**



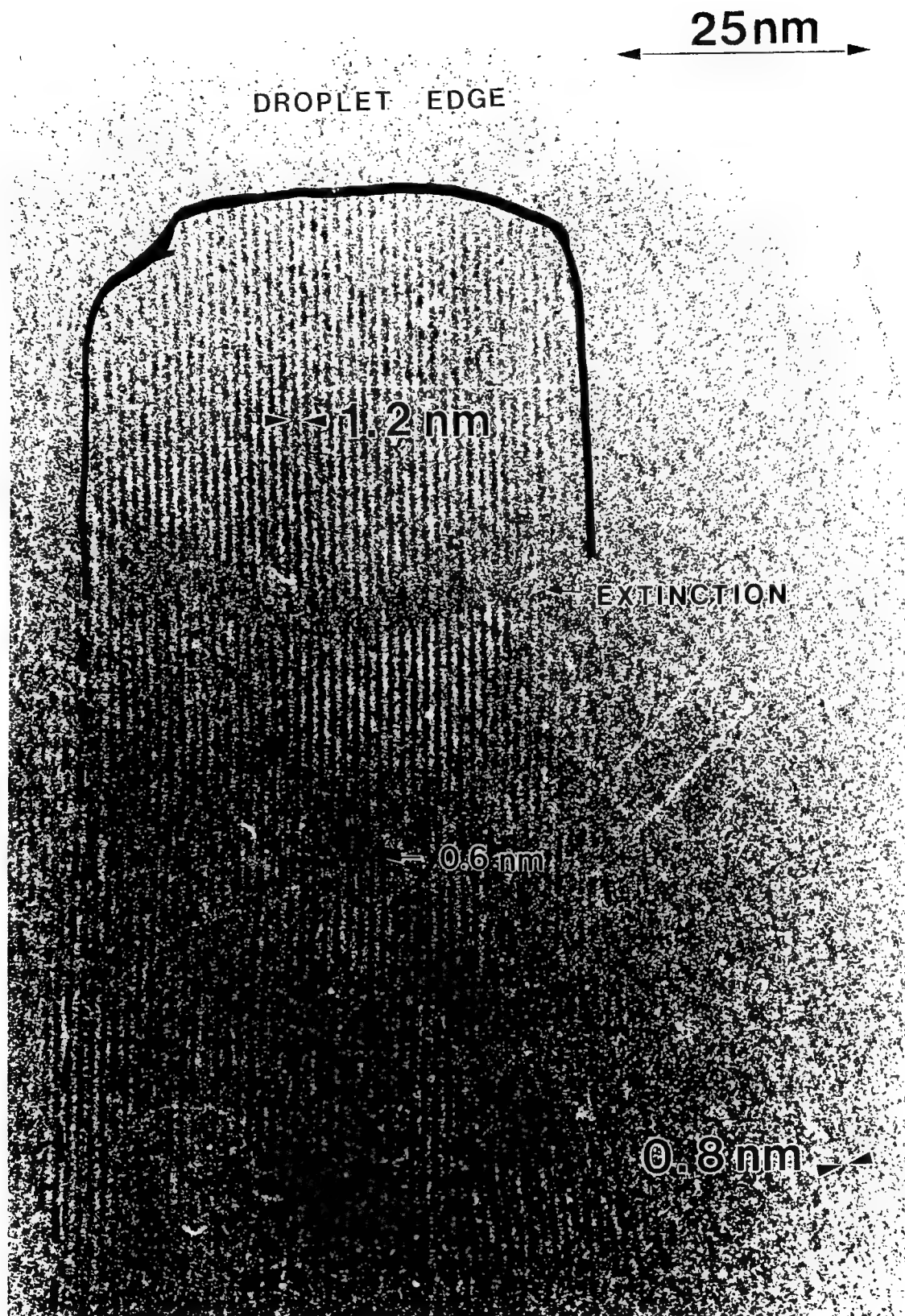


Figure 6.8

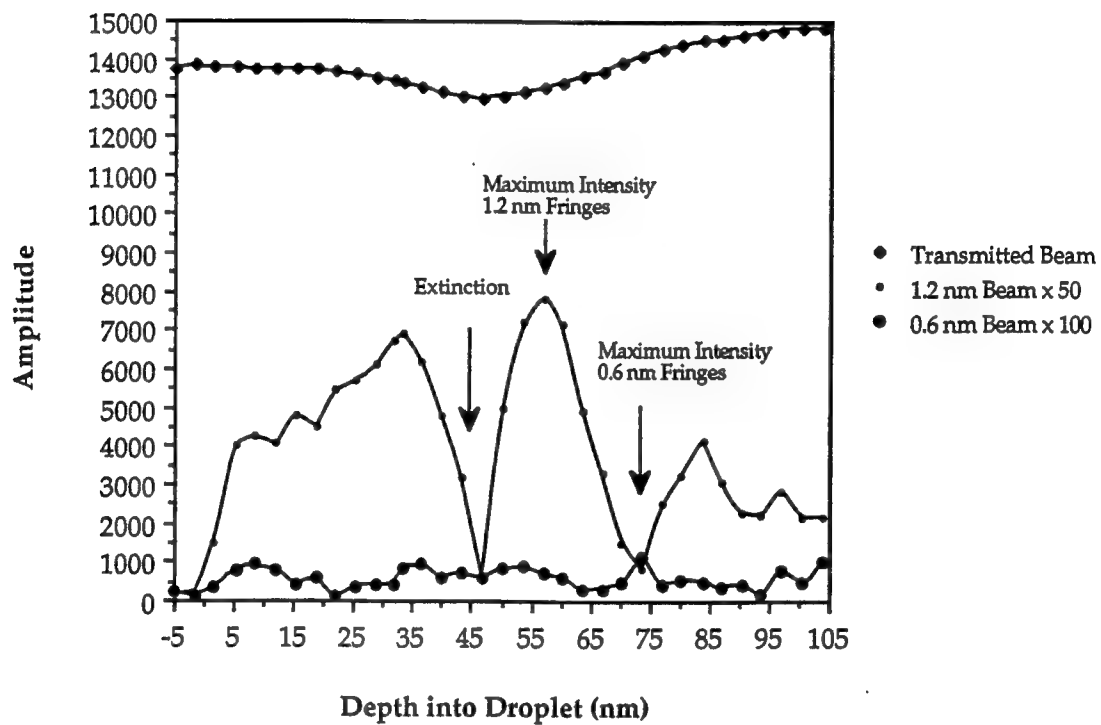


Figure 6.9: A plot of the amplitude of the periodicities in the HREM image as determined by FFT as a function of distance along the wedge. Unique images are indicated.

Table 6.4

**Experimental contrast type as a function of depth into the droplet. Multislice heights are based on Pendellosung plot and theoretical image contrast calculations.**

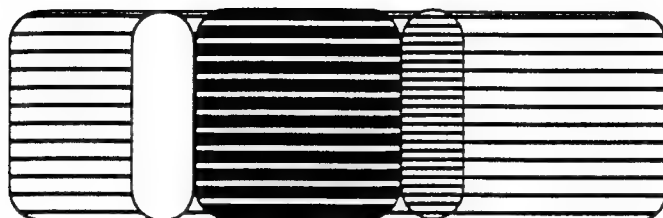
<u>Depth (nm)</u>	<u>Contrast Type</u>	<u>Multislice Height (nm)</u>
0 - 46.6	Starting pattern	
33.2	Local max of 1.2 nm	34.8
46.6	Extinction	45.0
46.6 - 73.5	Reversal of fringes	
57.3	Max Intensity of 1.2 nm	75.0
73.5	Half spacing	100.0
73.5 - 105.0	Reversal of Fringes	
83.8	Local max of 1.2 nm	128.8
105.0	Loss of fringe contrast	

where  $V_c$  is the volume of the unit cell,  $F_g$  is the structure factor,  $\lambda$  is the wavelength used, and  $\theta$  is the angle of the Bragg beam. Kinematic theory gives an extinction distance of 1,135 nm which is obviously an unrealistic thickness for a shallow droplet, as will be seen from the SPM results.

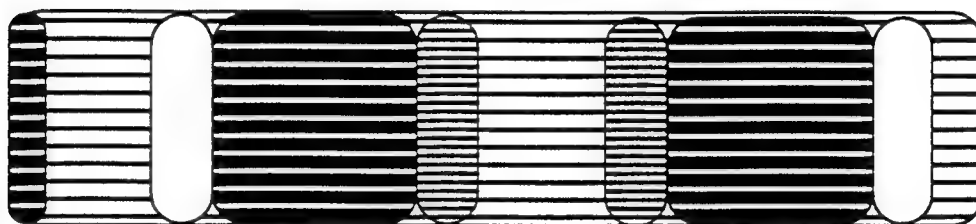
Figure 6.10 diagrams the wedge appearance of the experimental image, the prediction by the multislice calculation from poly(DCHD) at 400 kV, and also the typical behavior seen in small unit cell materials. Small unit cell materials, such as silicon and germanium, exhibit the sinusoidal periodicity of Pendellosung thickness images described using two beam dynamical theory by Spence (1988). The order of images seen in the experimental wedge qualitatively matches a section of the multislice prediction. The first reversal of contrast in the multislice prediction which occurs between 3.5 and 7.0 nm in thickness that is not seen in the experimental image. This corresponds to a thickness of two to four units cells. The step at the edge of the droplet could very well be nominally of this height and would obscure this image appearance if it existed.

SPM was used for an independent thickness measurement for the DCHD polymer wedges. Several droplets were imaged using tapping mode and their height profiles were recorded. The diameter of the measured droplets varied from 1.6 to 3.5  $\mu\text{m}$ . The raw data is presented in Figure 6.11. A representative SPM image is shown in Figure 6.12. In order to predict the height profile of the droplet in the HREM image which had a diameter of  $2.2 \pm 0.5 \mu\text{m}$ , the SPM profiles were normalized with respect to their diameters and angle of contact. The assumption was that the droplets were all cross sections of spheres. The relationship between the angle of contact to the surface,  $\theta$ , and diameter of the droplet,  $D$ , to the reference sphere radius,  $R$ , was:

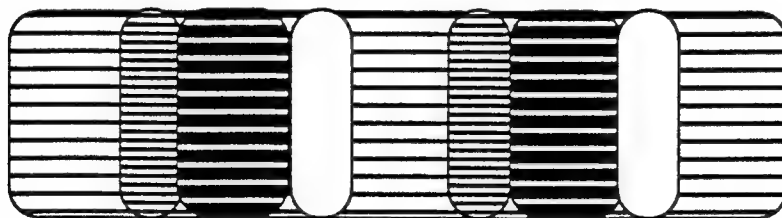
## Fringe Appearance for Wedge Profiles



Experimental Observation



Predicted By Multi-Slice Calculation



Predicted From Two-Beam Theory for Small Unit Cells

Figure 6.10: A schematic comparing the appearance of the experimental image, the multislice prediction, and the case for a sinusoidal variation of Pendellosung images for small unit cell materials.

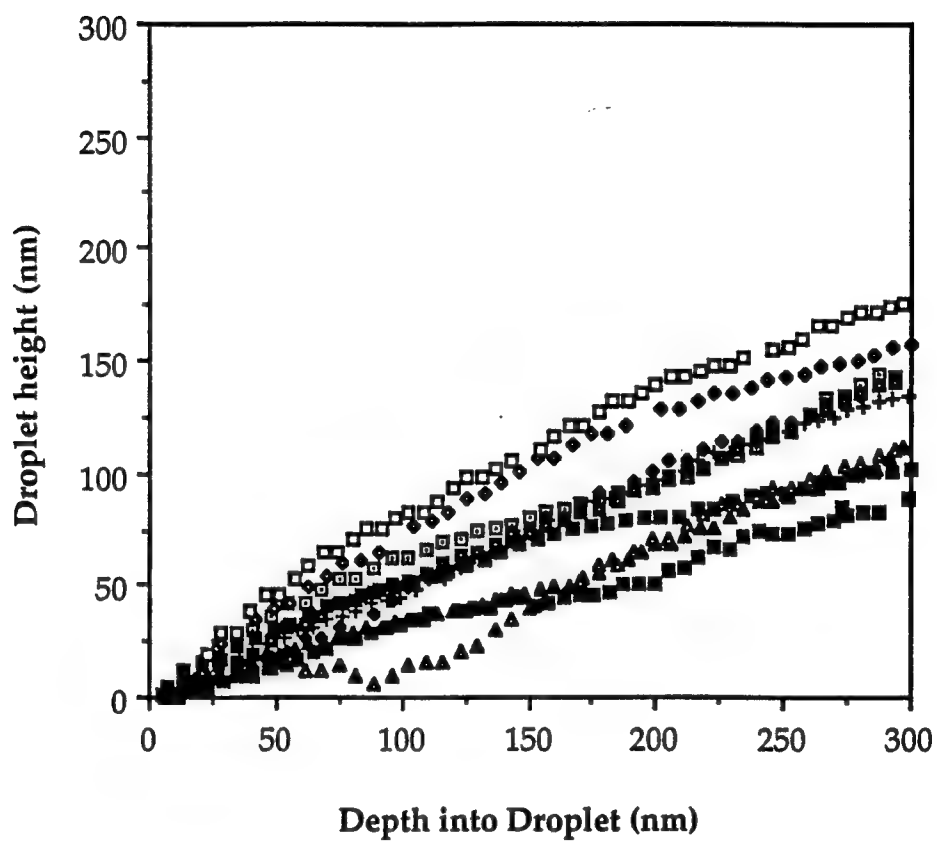


Figure 6.11: Height profiles for DCHD droplets examined with SPM.

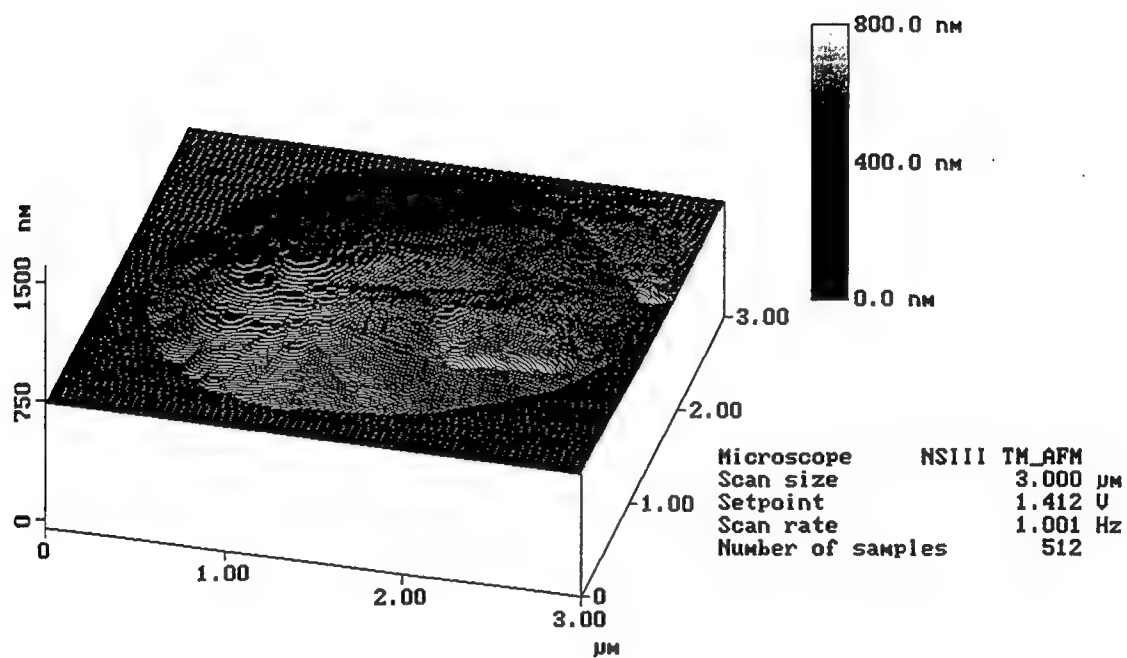


Figure 6.12: A representative SPM image of a poly(DCHD) droplet on a amorphous carbon coated mica substrate imaged using tapping mode.

$$R = \frac{D}{2\sin\theta}$$

Figure 6.13 illustrates this geometry. Normalizing the depth of the height profiles to the sphere radii produced Figure 6.14. The normalized profiles lie closely together even though their original angles of contact varied from 18.8° to 30°. The average normalized profile is shown in Figure 6.15. It can be modeled as a quadratic function. This relationship was used to calculate the experimental profile for the 2.2  $\mu\text{m}$  droplet that was imaged by HREM, using an average angle of contact (24.4°) determined from the SPM data.

The experimental profile based on the SPM data overlapped with the thicknesses predicted from the multislice calculations (Table 6.4) is shown in Figure 6.15. There is a good correlation between the two predictions at small distances into the droplet, but after 46.6 nm, the theoretical curve from the HREM analysis deviates to higher thicknesses. The theoretical curve predicts an initial angle of contact of 42° while experimental SPM data averaged  $24.4 \pm 5.5^\circ$ . Some SPM images showed a small step in the droplet profile similar to the theoretical curve, but not at the high angle of 60° which it predicts.

## Conclusions

Quantitative information about the intensity of fringes in HREM images has been used along with thickness measurements from AFM to investigate the validity of two-beam dynamical imaging theory in polymers. Multislice calculations were used to determine the voltage,  $400 \pm 10$  kV, which maximized the Pendellosung effect for (010) fringes. The Pendellosung



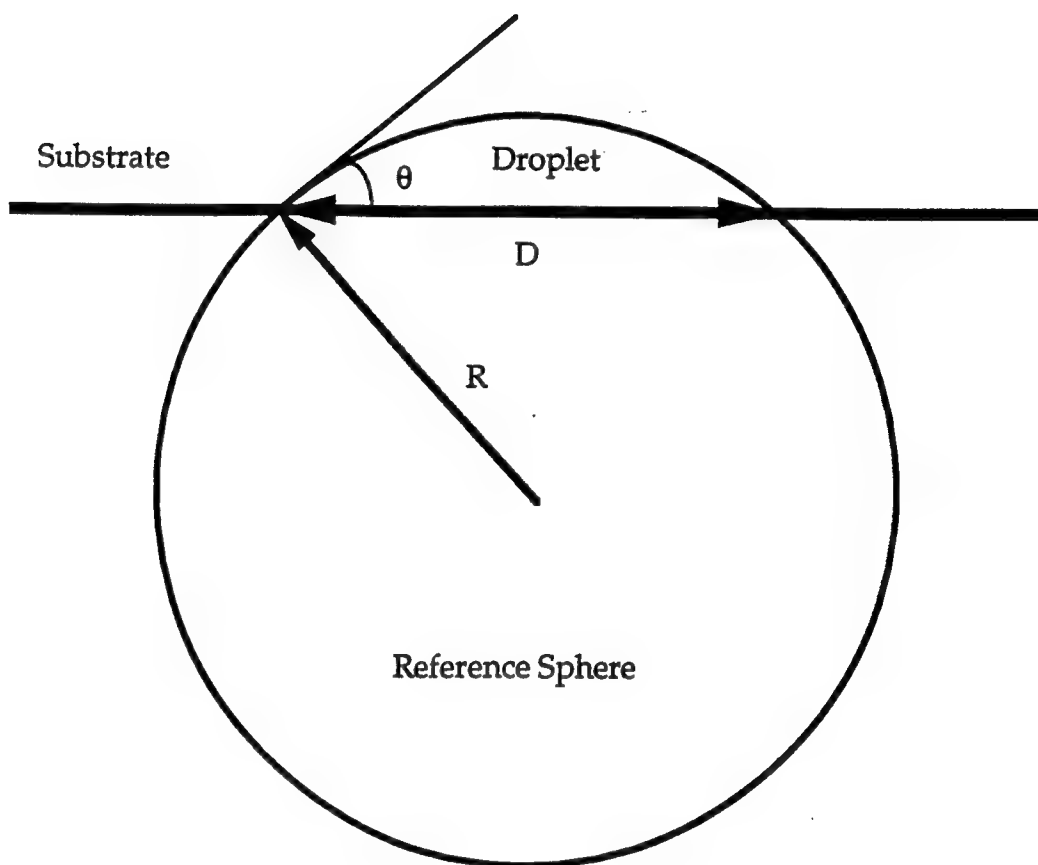


Figure 6.13: A diagram illustrating the geometry used to derive the relation between the radius of the sphere, the diameter of the droplet, and the angle of contact.

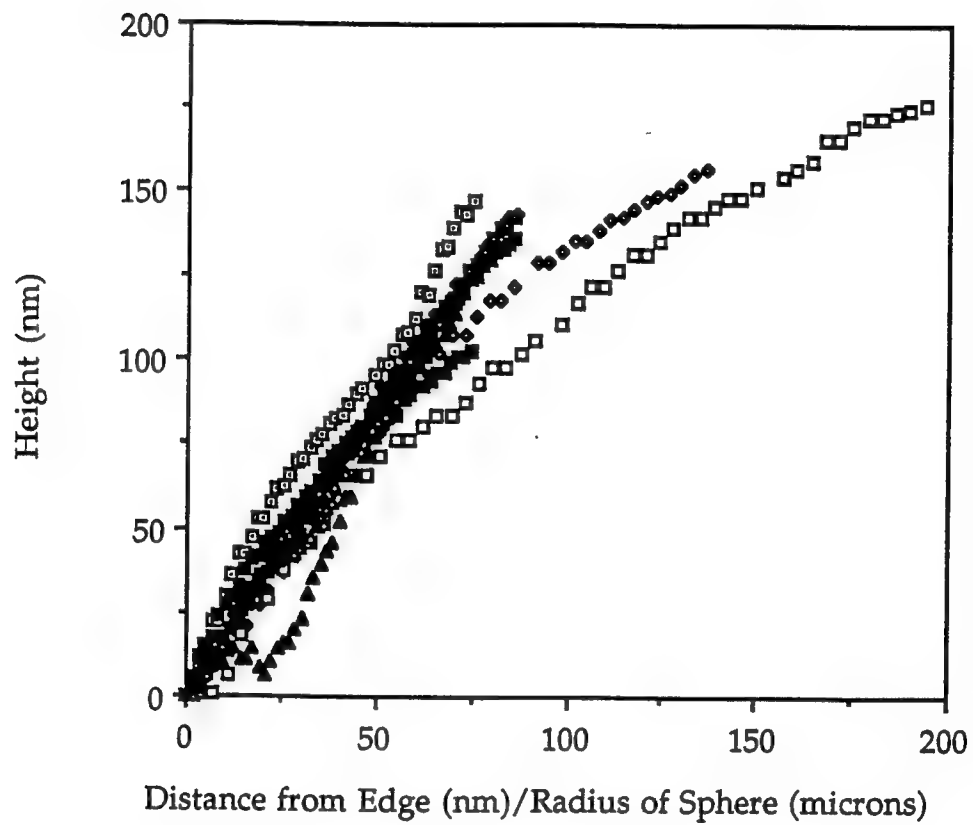


Figure 6.14: Height profile data measured by SPM for ten droplets. The depth was normalized by the radius of the reference sphere for each droplet.

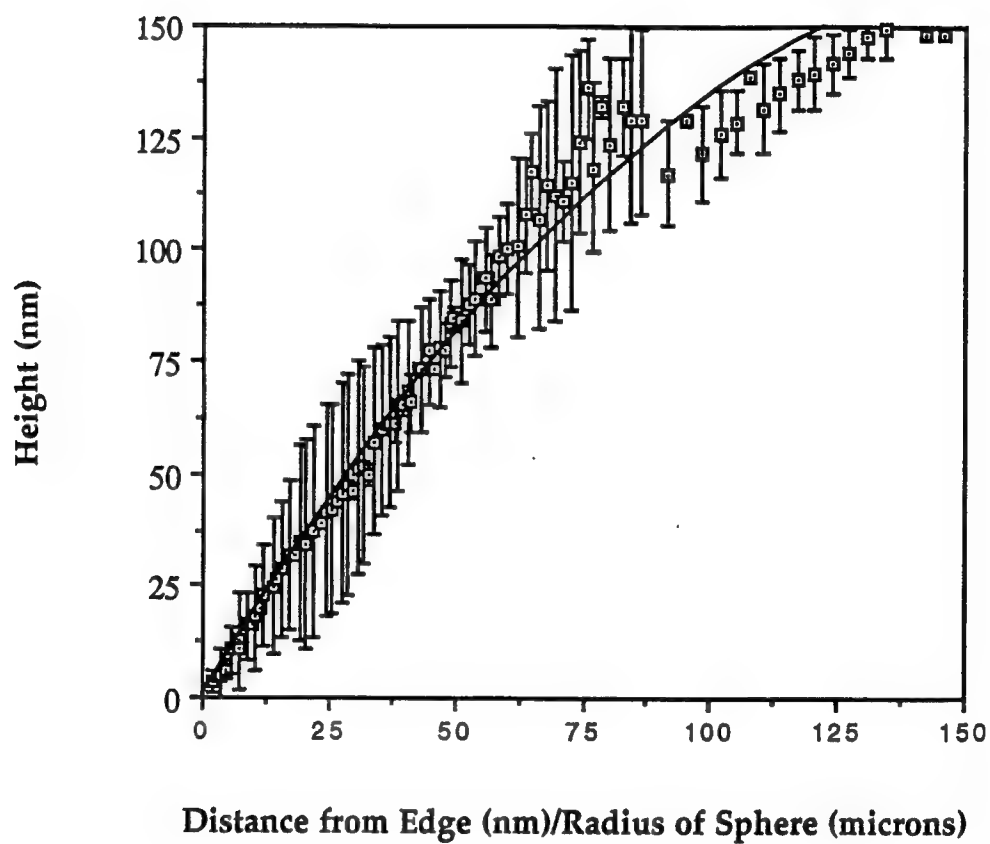


Figure 6.15: The average normalized height profile used to determine the profile of the droplets imaged by HREM.

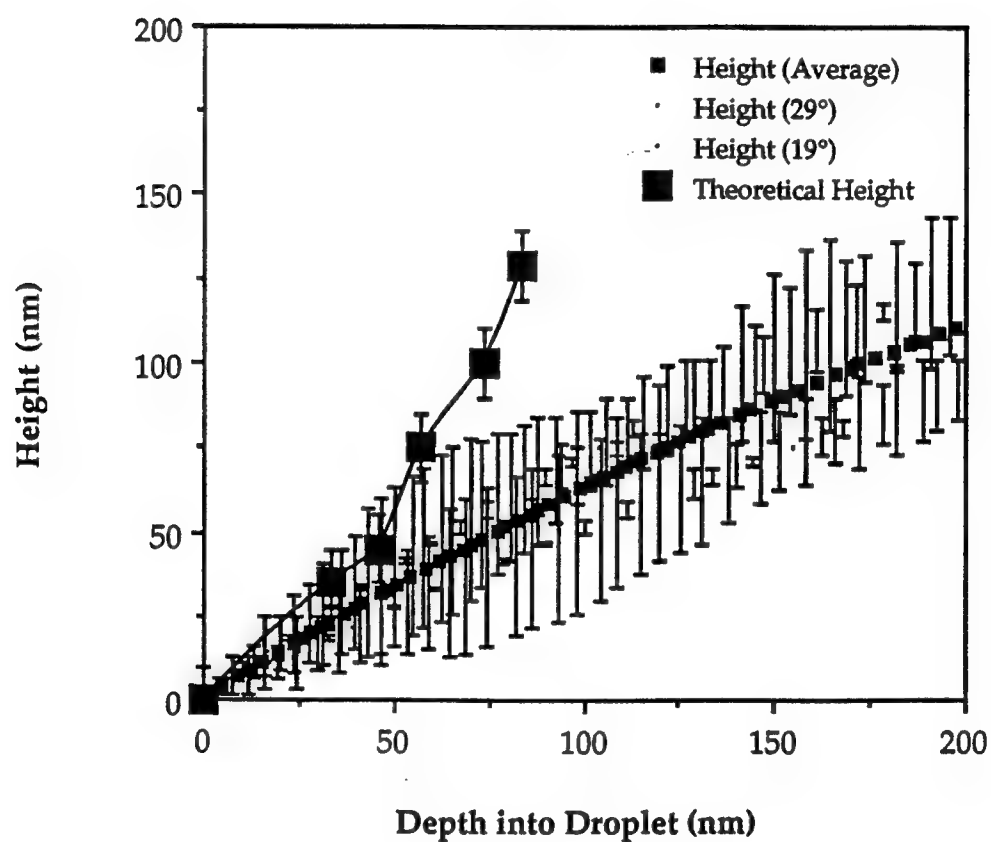


Figure 6.16: A plot of the SPM predicted droplet profiles overlaid by the prediction from dynamical theory.

effect for (010) fringes was not sinusoidal as shown for other materials of lower molar mass. The appearance of thickness images in both the experimental and calculated images were in the same qualitative order of appearance. Dynamical scattering theory, manifest in multislice calculations, predicted the measured droplet profiles from SPM at small distances into the droplets but deviated to higher thicknesses at longer distances. This underscores the need for independent thickness measurements to be used to quantify contrast in HREM images.

## CHAPTER VII

### CONCLUSIONS AND FUTURE WORK

Here the major conclusions of each chapter are summarized. Some suggestions for future work which could expand on the research presented in this thesis are also presented.

#### Chapter II: Droplets on Surfaces

The evaporation of DCHD monomer in chloroform solution on amorphous carbon substrates produced droplets that predominately have a uniform orientation of the eventual chain axis parallel to the substrate. The droplets are crystallographically fiber textured which produce lateral chain invariant (Martin and Thomas, 1991) grain boundaries. At droplet edges that are parallel to the chain axis, the polymer molecules exhibit a local curvature toward the center of the droplet. This curvature is thought to be the result of the monomer lattice conforming to the curvature of the droplet surface. To incorporate the bending strain, dislocations with a Burger's vector parallel to the chain axis are needed. HREM micrographs of the curving chains exhibit low angle tilt boundaries from the aggregation of dislocations.

Etching polymerized droplets showed rectangular surface pits ranging in size from 6-36 nm, with a slight elongation in the chain direction. The etch pits appeared in lines perpendicular to the surface of the droplet, perhaps showing the position of low angle grain boundaries. Etching results suggest that dislocations retard the polymerization in the region of the dislocation

core. This had been hypothesized for poly(toluene sulphonate) diacetylene by Young and Peterman (1981) on the basis that the distances would be too large between monomer units on the tensile side of the dislocation for reaction to take place. Further support for this idea is found in the detailed analysis of crystallographic structures of reactive and unreactive diacetylenes by Baughman (1974). He described a range of relative positional parameters, outside of which diacetylenes may be unreactive. Gerasimov (1990) found that hydrostatic compressive pressure retarded the polymerization reaction in DCHD. His experiment used pressures on the order of 4 kbar which correspond to values expected outside the core region in DCHD monomer using isotropic elasticity theory.

### Chapter III: Spheres

The formation of spheres from solution allowed several types of defects to be placed into the material. Lateral chain invariant grain boundaries and dislocations to incorporate bending were formed during crystallization. Spheres of DCHD were formed from saturated chloroform solution using Henkee's method (1988). The spheres which formed were thin shells, many with two opposing holes in the shell. HREM examinations showed that the polymer chains run parallel to the surface and curve with the same radius of curvature as the sphere. From SAED patterns, the spheres appear to be crystallographically textured, with a general orientation of the chain axis from hole to hole.

Further possibilities could include an investigation of the sphere morphology as a function of processing conditions. Variables include the evaporation rate, changed by the introduction of a gas flow or temperature

changes, concentration, and solvent type. Similarly, the density of defects as a function of processing condition could be investigated systematically.

#### Chapter IV: Dislocations

The introduction of covalent bonds in the chain direction increases the anisotropy of the elastic modulus. This anisotropy was shown to suppress the effect of shear between the chains due to weakening of correlations between chains. As the anisotropy increased, the elastic behavior of the shear strain approached that seen in columnar liquid crystals where correlations along the column do not exist.

The distortion around a chain end dislocation in a polymer crystal has been quantified from HREM images. The tilt of the polymer chains around a chain end edge dislocation in DCHD from HREM micrographs was modeled by both anisotropic crystal elasticity and liquid crystal theory. A polymer anisotropy parameter of  $W=3.5$  was necessary to model the magnitude and shape of the tilt using anisotropic crystalline elasticity. A value of 0.8 nm, one interchain spacing, for  $\lambda$  was needed to match columnar liquid crystal theory to the experimental data. Varying the parameter  $W$  showed that as the anisotropy due to covalent bonding in the  $c$  direction increased, the appearance of the tilt tended toward the behavior of the columnar liquid crystal solution. The character of the distortion in the experimental data closely matched that predicted by the anisotropic linear elastic solution for the polymer when  $W=3.5$ . This suggests that there are substantial relaxations which occur during polymerization around the dislocation. The distortion was localized near the core of the dislocation. This enabled the linear elastic solution to be used to predict behavior over most of the local area of the defect. Dislocation energies ( $\sim 10^{-7}$  J/m) were higher than those for metals



( $\sim 10^{-9}$  J/m) because of the introduction of a energy penalty for distortions of the covalent bonds.

These results can be used to generalize what is expected for dislocations with different Burger's vectors and line directions. Strain fields for dislocations with a Burger's vector parallel and line direction perpendicular to the chain are expected to resemble isotropic results. Slip in the Burger's vector direction is allowed as chains only have to move along one another. Dislocations of this type would be glissile in glide, but sessile for climb. When looking down the chain, the Burger's vector would be perpendicular to the chain, but the line direction is parallel to the chain. For high anisotropies, the strain would tend towards the solution for columnar liquid crystals when looking down the column, because of the lack of correlations between chains. Dislocations of this type would be expected to be glissile. The particular dislocation analyzed has both the Burger's vector and the line direction perpendicular to the chain. It will be sessile for both glide and climb.

The molecular mechanics simulations overestimate the polymer chain modulus and underestimate the transverse moduli as compared to experimental values in the literature. Future work would refine the ability to predict the dislocation structure by using experimentally derived compliance matrices. Brillouin scattering (Kumar, et al, 1994) might also be used to determine the full stiffness matrix from a single sample.

## Chapter V: Grain Boundaries

The use of O-lattice theory (Bollman, 1970) to model the geometry of DCHD monomer bicrystal interface resulted in a generalized transformation to describe twist boundaries in monoclinic materials. The resulting geometrical construct for axial chain invariant (Martin and Thomas, 1991)

polymer bicrystals was used to predict the density of screw dislocations at the interface and conversely the amount of interfacial area that was relaxed for a given bicrystal misorientation. The relaxed fraction,  $f$ , is proportional to the amount of material which can polymerize through the interface, which in turn is proportional to any material property dependent on chain connectivity. This geometrical theory was found to capture the essential character of the relationship between properties such as photoconductivity, mechanical strength, and critical current density for superconductivity (Dimos et al., 1990) as a function of misorientation angle. Fitting the theory to experimental data provided by Liao (1994) resulted in a prediction that the relaxation at the boundary which affected the photoconductivity was half of a Burger's vector for each set of screw dislocations. The shape of the experimental curve suggested a transition in conduction mechanism with increasing angle of misorientation. At low angles where the dislocations are discrete, the response is due mainly to conduction along the chains as they pass through the interface. At high angles when the cores of the dislocations begin to overlap, there are few chains through the interface and an interchain hopping mechanism dominates the magnitude of the response. This transition occurs between  $3^\circ$  and  $5^\circ$  of bicrystal misorientation, emphasizing that the photoconductive response is extremely sensitive to defect density. The O-lattice development was found to be only applicable to predict the response at low angles from the available data.

Further refinement of the geometrical theory could take into account the polymerization constrained by the boundary and the breakup of the global misorientation into smaller units. Liao and Martin (1993) have determined the transformation matrix between monomer and polymer crystals for the polymerization reaction from electron diffraction results. The

transformation matrix,  $T_{ij}^{mp}$ , describes the crystalline intermediates in terms of reciprocal lattice vectors referenced to an orthogonal axis system.

The general transformation combining both the polymerization reaction and O-lattice description of grain boundary geometry would be:

$$X^{oP} = (I - S^{-1}A^{-1}S)^{-1}Q^{-1}T_{ij}^{mp}Qb_L^m$$

Where  $X^{oP}$  is the O-lattice vectors in the polymer,  $Q$  is a matrix governing the transformation from the axis system used by Liao (1994) to the axis system used in Chapter VI, and the  $b_L^m$  are the unit cell vectors for the monomer. This is based on the realization that:

$$b_L^p = Q^{-1}T_{ij}^{mp}Qb_L^m$$

For the twist solution,  $T_{ij}^{mp}$  is in the appropriate form based on the geometry. Difficulties arise in defining where the polymerization reaction begins. Two special cases can be defined, one where the polymerization reaction is nucleated at the interface and the second where the polymerization occurs homogeneously. If the polymerization reaction starts at the interface, the dislocation structure at the interface may be preserved, resulting in the angle of the grain boundary changing to accommodate the polymer structure, then  $X^{oP} = X^{oM}$ . If the polymerization is homogeneous, possibly the angle of misorientation is constrained, resulting in the O-lattice (dislocation structure) changing (King, 1994). Careful measurement of bicrystal angles using optical goniometry before and after polymerization could clarify this problem.

The solution for tilt boundaries is complex because all three axes contribute to the solution and the determinant  $|\mathbf{I-S}^{-1}\mathbf{A}^{-1}\mathbf{S}|^{-1}$  is zero. Every geometrical situation has to be solved as a set of three independent equations for the solution. To better explain the experimental data from Liao (1994), the tilt solution for the constructed tilt bicrystals needs to be derived. There are two possible ACR tilt boundaries as constructed by Liao (1994). A rotation of the crystal around [010] will produce an array of [100] edge dislocations whereas a rotations around [100] will produce an array of [010] edge dislocations. Figure 7.1 illustrates the types of tilt boundaries Liao has produced.

## Chapter VI: HREM of Polymers

Comparisons between HREM images and SPM thickness measurements were performed on wedge-shaped polydiacetylene crystals. These measurements questioned the use of HREM "thickness images" as independent means of measuring the thickness of a sample. Kinematic and dynamic extinction distances were also shown to be not valid for the experimental situation. Pendellosüing plot calculations showed that the two beam imaging effect was strongest at  $400 \pm 10$  kV for the (000) and (010) beams from poly(DCHD). Experimental HREM wedge images were analyzed to determine the intensity of the periodicities in the image as a function of depth into the droplet. An extinction of the 1.2 nm (010) periodicity was found at a depth of 46.6 nm while a change to half spacing fringes (0.6 nm) was found at a depth of 73.5 nm. Calculations of the expected image intensity from dynamical two beam theory illustrated the imaging mechanics governing the extinction and

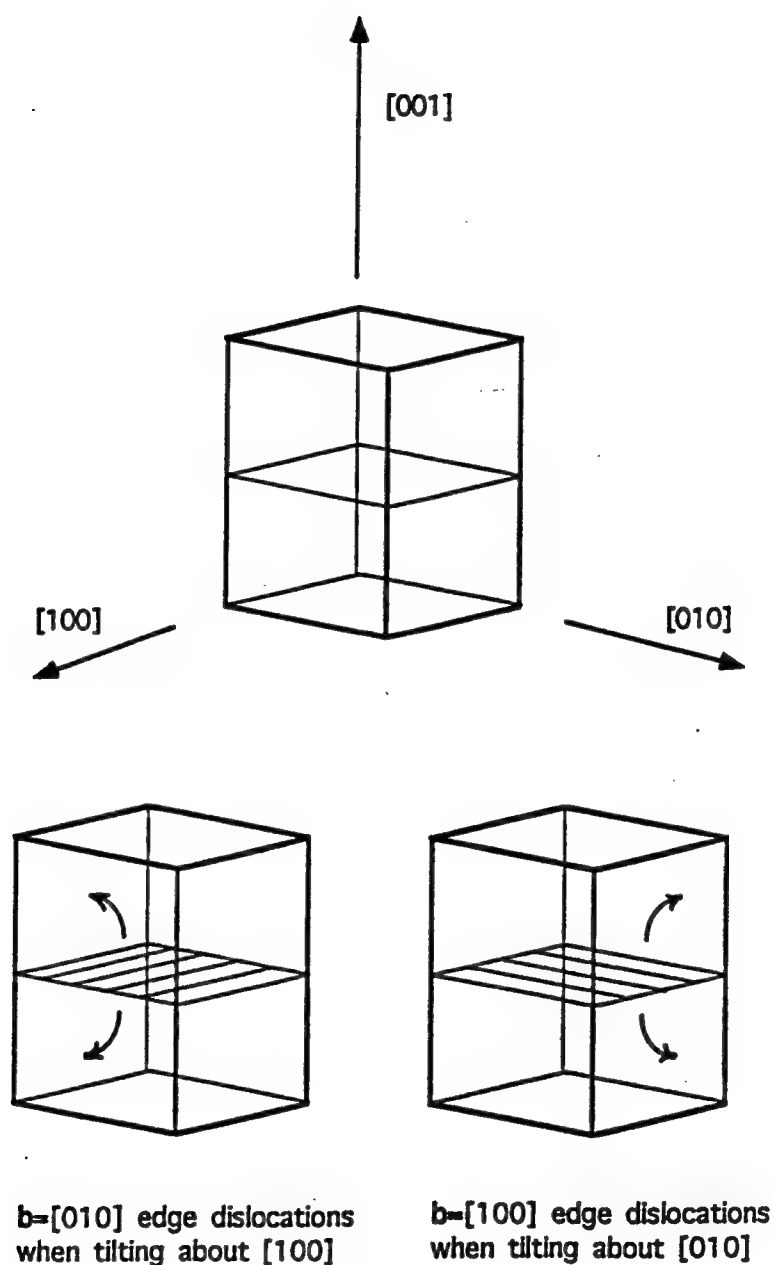


Figure 7.1: Schematic diagram of a polymer bicrystal to create ACR boundaries. It is possible to create an array of  $[010]$  edge dislocations at the interface by tilting about the  $[100]$  direction. Likewise, tilting about  $[010]$  generates  $[100]$  edge dislocations. The spacing between the dislocations decreases as the angle between the grains increases.

half spacing contrast. Pendellosing plots calculated using the multislice technique accurately predicted that these images would appear as a function of increasing thickness.

Height profiles of several droplets were obtained using atomic force microscopy. When the profiles were normalized assuming they were part of a larger sphere, they collapsed onto a single profile. The normalized profile was then used to predict the experimental profile of the HREM image to compare to the multislice predicted thicknesses for the extinction and half spacing image.

The data showed the need for HREM and SPM to be performed on the same droplet for comparison with theoretical predictions. Droplets could be formed on finder grids and used for both techniques through careful operation and recording of the surrounding region in the TEM for identification purposes.

More quantitative calculations of the contrast could be undertaken. Currently CERUS<sup>2</sup> (Molecular Simulations, Inc., 1994) calculates the amplitudes of the beams from the multislice technique but normalizes the values in the process. The software could be modified to gain access to the unscaled data in order to calculate intensities in the image plane. Careful recording of the electron flux versus optical density for a series of micrographs of amorphous carbon could be used to quantify the contrast in the HREM images. The goal is to reach the point where contrast in the image can be directly related to the amount of electron potential at a point.

## BIBLIOGRAPHY

- Aime, J.P., Lefebvre, J., Bertault, M., Schott, M., and Williams, J.O., "Studies of a Polymerizable Crystal: I-Structure of Monomer pTS (bis-p-toluenesulphonate of 2,4-hexadiyne 1,6-diol) by Neutron Diffraction at 120 and 221 K", *J. Physique* **43**, 307, (1982)
- Allain, M. and Kleman, M., "Thermodynamic Defects, Instabilities and Mobility Processes in the Lamellar Phase of a Non-Ionic Surfactant", *J. Physique* **48**, 1799, (1987)
- Allen, S., "Materials with a Bent for Light", *New Scientist* **1**, 59, (1989)
- Apgar, P.A. and Yee, K.C., "Poly[1,6-di(N-carbazolyl)-2,4-hexadiyne]", *Acta Crystallogr.* **B34**, 957, (1978)
- Barry, J.C. "Solving Defect Structures by HRTEM: Expectations and Limitations", in R. Sinclair, D. Smith, and U. Dahman, eds., *Materials Research Society Proceedings Volume 183*, Materials Research Society, Pittsburgh, PA, 243 (1990)
- Batchelder, D.N. and Bloor, D., "Strain Dependence of the Vibrational Modes of a Diacetylene Crystal", *J. Polym. Sci. Polym. Phys. Ed.* **17**, 569, (1979)
- Baughman, R.H., "Solid-State Synthesis of Large Polymer Single Crystals", *J. Polym. Sci. Polym. Phys. Ed.* **12**, 1511, (1974)
- Baughman, R.H., "Solid-State Reaction Kinetics in Single-Phase Polymerizations", *J. Chem. Phys.* **68**(7), 3110, (1978)
- Bellare, J.R. and Thomas, E.L., "Apparatus for 'on-the-fly' Sample Preparation of Aerosol-Grown Block Copolymer Microdroplets", in G.W. Bailey, ed., *Proceedings of the 47th Annual Meeting of the Electron Microscopy of America*, San Francisco Press, Inc., San Francisco, CA, 354, (1989)
- Bennion, I., "Applications of Nonlinear and Electro-Optic Materials", *Inst. Phys. Conf. Ser.* No 103, 1, (1989)
- BioDesign, Inc., *BioSym Discover manual*, (1993)
- Berrehar, J., Lapersonne-Meyer, C., Schott, M., and Villain, J., "Formation of Periodic Crack Structures in Polydiacetylene Single Crystal Thin Films", *J. Phys. France* **50**, 923, (1989)

- Bloor, D., Koski, L., and Stevens, G.C., "Solid State Polymerization of bis-(p-toluene sulphonate) of 2,4-hexadiyne-1,6-diol", *J. of Mat. Sci.* **10**, 1689, (1975)
- Bloor, D., Koski, L., Stevens, G.C., Preston, F.H., and Ando, D.J., "Solid State Polymerization of bis-(p-toluene sulphonate) of 2,4-hexadiyne-1,6-diol", *J. of Mat. Sci.* **10**, 1678, (1975)
- Bloor, D., "The Morphology of poly bis(p-toluene sulphonate) Diacetylene Crystals", *J. of Mat. Sci.* **14**, 248, (1979)
- Bloor, D., Chalmers, I.F., Kennedy, R.J., and Motevalli, M., "Phase Transition Boundaries in 1,6-di(carbazolyl)-2,4-hexadiyne", *Mol. Cryst. Liq. Cryst.* **93**, 215, (1983)
- Bloor, D., "Diacetylene Polymerization Kinetics", in D. Bloor and R.R. Chance, ed., *Polydiacetylenes, Synthesis, Structure and Electronic Properties*, Martinus Nijhoff Publishers, Dordrecht, (1985)
- Bollmann, W., *Crystal Defects and Crystalline Interfaces*, (Springer-Verlag, New York, 1970)
- Bursill, L.A. and Barry, J.C., "Electron Optical Imaging of Diamond", *Optik*, **65**(4), 271, (1983)
- Buseck, P., Cowley, J., Eyring, L., *High-Resolution Transmission Electron Microscopy and Associated Techniques*, (Oxford University Press, New York, 1988)
- Chance, R.R., Baughman, R.H., Reucroft, P.J., and Takahashi, K., "Transient Photoconductivity of a Polydiacetylene Single Crystal", *Chemical Physics* **13**, 181, (1976)
- Chance, R.R. and Patel, G.N., "Solid-State Polymerization of a Diacetylene Crystal: Thermal, Ultraviolet, and  $\gamma$ -Ray Polymerization of 2,4-Hexadiyne-1,6-Diol Bis-(p-Toluene Sulfonate)", *J. Polym. Sci., Polym. Phys. Ed.* **16**, 859, (1978)
- Chiang, J. and Prud'Homme, R.K., "Production of Monodisperse 5- to 40- $\mu$ m Polystyrene Spheres", *J. of Colloid and Interface Science*, **122**(1), 283, (1988)
- Choi, H.C., Schwartzman, A.F., and Kim, K.S., "Experimental Deformation Mechanics of Materials from their Near-Atomic-Resolution Defect Images", *Mat. Res. Soc. Symp. Proc.* **239**, 419 (1991)
- Collings, P.J., *Liquid Crystals*, (Princeton University Press, Princeton, 1990)



- Courtney, T.H., *Mechanical Behavior of Materials*, (McGraw-Hill Publishing Company, New York, 1990)
- DeGennes, P.G and Prost, J., *The Physics of Liquid Crystals, 2nd Ed.*, (Clarendon Press, Oxford, 1993)
- Desseaux, J., Renault, A., and Bourret, A., "Multi-Beam Lattice Images from Germanium Oriented in (011)", *Phil. Mag.* 35(2), 357, (1977)
- Dudley, M., Sherwood, J.N., Ando, D.J., and Bloor, D., "SRS Radiation Induced Polymerization of 2,4-Hexadiynediol-bis-(p-toluenesulphonate) (PTS)", *Mol. Cryst. Liq. Cryst.* 93, 223, (1983)
- Dudley, M., Sherwood, J.N., Ando, D.J., and Bloor, D., "X-Ray Topographic Studies of the Solid-State Polymerization of PTS (2,4-Hedadiyne diol bis(p-toluene sulphonate))", D. Bloor and R.R. Chance, eds., *Polydiacetylenes, Synthesis, Structure and Electronic Properties*, Martinus Nijhoff Publishers, Dordrecht, (1985)
- Enkelmann, V., Schleier, G., Wegner, G., Eichele, H., and Schwoerer, M., "Structure, Luminescence and Polymerization of a Diacetylene Crystal: 1,6-di-(N-carbazolyl)-2,4 hexadine (DCH)", *Chem. Phys. Lett.* 52(2), 314 (1977)
- Enkelmann, V., Leyrer, R.J., and Wegner, G., "Investigation of the Topochemical Solid-State Polymerization of a Diacetylene by X-ray Methods and Brillouin-Spectroscopy", *Makromol. Chem.* 180, 1787, (1979)
- Enkelmann, V., Leyrer, R.J., Schleier, G., and Wegner, G., "Macroscopic Single Crystals of Polymers by Solid-State Polymerization: a Study of the Monomer to Polymer Phase Transformation 1,6-dicarbazolyl hexadiyne", *J. of Mat. Sci.* 15, 168, (1980)
- Flory, P.J., *Principles of Polymer Chemistry*, (Cornell University Press, Ithaca, 1953)
- Fitzgerald, J.F. and Corrigan, O.I., "Mechanisms Governing Drug Release from Poly- $\alpha$ -Hydroxy Aliphatic Esters. Diltiazem Base Release from Poly-Lactide-co-Glycolide Delivery Systems", in M.A. El-Nokaly, D.M. Piatt, and B.A. Charpentier, Eds., *Polymeric Delivery Systems. Properties and Applications.*, (American Chemical Society, Washington, D.C., 1993)

- Galiotis, C. and Young, R.J., "The Solid-State Polymerization and Physical Properties of Bis(ethyl urethane) of 2,4-hexadiyne-1,6-diol: 3. Mechanical Properties", *Polymer* **24**, 1023, (1983)
- Galiotis, C., Young, R.J., and Batchelder, D.N., "The Solid-State Polymerization and Physical Properties of Bis(ethyl Urethane) of 2,4-hexadiyne-1,6-diol. II. Resonance Raman Spectroscopy", *J. Polym. Sci. Polym. Phys. Ed.* **21**, 2483, (1983)
- Galiotis, C., Read, R.T., Yeung, P.H.J., Young, R.J., Chalmers, I.F., and Bloor, D., "High-Modulus Polydiacetylene Single-Crystal Fibers", *J. Polym. Sci. Polym. Phys. Ed.* **22**, 1589, (1984)
- Gerasimov, G.N., "Reactivity of Strained Configurations in Solid-State Polymerization Reactions", *Mol. Cryst. Liq. Cryst.* **187**, 215, (1990)
- Gjonnes, J. and Moodie, A.F., "Extinction Conditions in the Dynamic Theory of Electron Diffraction", *Acta Cryst.* **19**, 65, (1965)
- Glaisher, R.W. and Spargo, A.E.C., "Aspects of HREM of Tetrahedral Semiconductors", *Ultramicroscopy*, **18**, 323, (1985)
- Glaisher, R., Rez, P., and Gajdardziska, M., "Imaging Theory II", Notes from ASU Facility for HREM Winter School (1992)
- Graun, H-G and Wegner, G., "New Experiments Concerning the Mechanism of Solid-State Photopolymerization of 2,5-Distyrylpyrazine", *Makromol. Chem.* **184**, 1103, (1983)
- Green, L., Phan, L.X., Schmitt, E.E., and Mohr, J.M., "Side-Chain Crystallizable Polymers for Temperature-Activated Controlled Release." in M.A. El-Nokaly, D.M. Piatt, and B.A. Charpentier, Eds., *Polymeric Delivery Systems. Properties and Applications*, American Chemical Society, Washington, D.C., (1993)
- Hankin, S.H. and Sandman, D.J., "Raman Spectroscopic Evidence for a Surface Phase on As-Polymerized Single Crystals of the Polydiacetylene from THD", *Macromolecules* **24**, 4983 (1991)
- Henkee, C.S., Thomas, E.L., Fetters, L.J., "The Effect of Surface Constraints on the Ordering of Block Copolymer Domains", *J. of Mat. Sci.* **23**, 1685, (1988)
- Hetherington, C.J.D., "HREM of Defects in Silicon at Twin Intersections", *Mat. Res. Soc. Symp. Proc.* **183**, 123, (1990)

- Hirsh, P., Howie, A., Nicholson, R.B., Pashley, D.W., and Whelan, M.J., *Electron Microscopy of Thin Crystals*, (Robert E. Krieger Publishing Company, Malabar, 1965)
- Hirshfeld, F.L. and Schmidt, G.M.J., *J. Polymer Sci., Part A* **2**, 2181, (1964)
- Hirth, J.P. and Lothe, J., *Theory of Dislocations, 2nd Ed.*, (John Wiley and Sons, New York, 1982)
- Hone, D. and Singh, C., "Strong Disorder and the Nonlinear Susceptibility of Conjugated Polymers", Personal Communication (1992)
- Hone, D. and Singh, C., *Bull. Am. Phys. Soc.* **37** (1), 355 (1992)
- Hudson, S.D. and Thomas, E.L., "Disclination Interaction in an Applied Field: Stabilization of the Lehmann Cluster", *Physical Review A* **44**(12), 8128, (1991)
- Hudson, S.D., Fleming, J.W., and Thomas, E.L., "Disclination Core Structure in Rigid and Semi-Flexible Main Chain Polymer Nematic Liquid Crystals", Personal Communication (1992)
- Hudson, S.D., Fleming, J.W., Gholz, E., and Thomas, E.L., "Disclination Core Structure in Rigid and Semiflexible Main-Chain Polymer Nematic Liquid Crystals", *Macromolecules* **26**, 1270, (1993)
- Hull, D. and Bacon, D.J., *Introduction to Dislocations, 3rd Ed.*, (Pergamon Press, Oxford, 1984)
- Jap, G.K. and Glaeser, R.M., "The Scattering of High-Energy Electrons. II. Quantitative Validity Domains of the Single-Scattering Approximations for Organic Crystals", *Acta Cryst.* **A36**, 57, (1980)
- Jones, M-C.G., Jiang, T., and Martin, D.C., "Microstructural Characterization of Crosslinkable PPTA-co-XTA Copolymer Fibers", *Macromolecules*, in print, (1994)
- Kim, Y-W, Lin, H-M, and Kelly, T. F., "Solidification Structures in Submicron Spheres of Iron-Nickel: Experimental Observations", *Acta Metall.*, **36**(9), 2525, (1988)
- King, A.H. and Zhu, Y., "Twin-corner disclinations in  $\text{YBa}_2\text{Cu}_3\text{O}_{7-d}$ ", *Phil. Mag. A* **67**(4), 1037, (1993)
- King, A.H. and Singh, A., "Generalizing the Coincidence Site Lattice Model to Non-Cubic Materials", Personal Communication (1994)

- Kléman, M. and Oswald, P., "Columnar discotic mesophases: Elasticity, Dislocations, Instabilities", *J. Physique*, **43**, 655, (1982)
- Kléman, M., *Points and Lines and Walls: in Liquid Crystals, Magnetic Systems, and Various Ordered Media*, (John Wiley and Sons, New York, 1983)
- Klein, C. and Hurlbut, Jr., C.S., *Manual of Mineralogy 20th Edition*, (John Wiley and Sons, New York, 1977)
- Kobayashi, T. and Isoda, S., "Lattice Images and Molecular Images of Organic Materials", *J. Mater. Chem.* **3**(1), 1, (1993)
- Kobelt, V.D. and Paulus, E.F., "Poly-[1,2-bis-(p-tolylsulfonyloxymethylen)-1-buten-3-inylen]", *Acta Crystl.* **B30**, 232, (1974)
- Kollmar, C. and Sixl, H., "Reaction Kinetics of the Solid State Polymerization in Diacetylene Crystals", *J. Chem. Phys.* **87**(9), 5541, (1987)
- Kosevich, A. M. and Boiko, V.S., "Dislocation Theory of the Elastic Twinning of Crystals", *Soviet Physics Uspekhi* **14**(3), 286, (1971)
- Krimm, S., Personal Communication, (1994)
- Kumar, S. and Adams, W.W., "Electron Beam Damage in High Temperature Polymers", *Polymer* **31**, 15, (1990)
- Kumar, R.S., Renusch, D.P., and Gimsditch, M., "Elastic Properties of Polyimide Films", Poster presentation at the 35th IUPAC International Symposium on Macromolecules in Akron, Ohio, July 11-15, 1994
- LeMoigne, J., Thierry, A., Chollet, P.A., Kajzar, F., and Messier, J., "Morphology, Linear and Nonlinear Optical Studies of poly[1,6-di(N-carbazolyl)-2,4 hexadiyne] Thin Films (pDCH)", *J. Chem. Phys.* **88**, 6647, (1988)
- LeMoigne, J., Kajzar, F., and Thierry, A., "Single Orientation in Poly(diacetylene) Films for Nonlinear Optics. Molecular Epitaxy of 1,6-Bis(9-carboxyl)-2,4-hexadiyne on Organic Crystals", *Macromolecules* **24**, 2622 (1991)
- Liao, J. and Martin, D.C., "Direct Imaging of the Diacetylene Solid-State Monomer-Polymer Phase Transformation", *Science* **260**, 1489 (1993)
- Liao, J., Stewart, J., and Martin, D.C., Personal Communication, (1994)

- Lin, H-M., Kim, Y-W., and Kelly, T. F., "Solidification Structures in Submicron Spheres of Iron-Nickel: Experimental Observation", *Acta Metall.*, **36**(9), 2537, (1988)
- Loretto, M.H., *Electron Beam Analysis of Materials*, (Chapman and Hall, New York, 1984)
- Martin, D.C., Ph.D. Dissertation, University of Massachusetts (1990)
- Martin, D.C. and Thomas, E.L., "Grain Boundaries in Extended-Chain Polymers: Theory and Experiment", *Phil. Mag. A* **64**(4), 903, (1991)
- Martin, D.C. and Thomas, E.L., "Micromechanisms of Kinking in Rigid-Rod Polymer Fibers", *J. of Mat. Sci.* **26**, 5171, (1991)
- Martin, D.C., Berger, L.L., Gardner, K.H., "Structural Evolution of a Model Poly(imide): Organization near Surfaces", *Macromolecules* **24**, 3921, (1991)
- Martin, D.C., "Intermolecular Twist Defects in Extended-Chain Polymers", *Macromolecules* **25**, 5171, (1992)
- Martin, D.C., "Defects in Polymer Solids", *Trends in Polymer Science* **1**(6), 178, (1993)
- Masters, K., *Spray Drying Handbook, Fifth edition*, (John Wiley and Sons Inc., New York, 1991)
- Mayo, S.L., Olafson, B.D., and Goddard, W.A., "Dreiding: A Generic Force Field for Molecular Simulations", *J. of Phys. Chem.* **94**, 8897, (1990)
- Menter, J.W., "The Electron Microscopy of Crystal Lattices", *Advances in Physics* **7**(27), 300, (1958)
- Molecular Simulations, Inc. Professional Polygraf Manual, Version 3.2 (1992)
- Nabarro, F.R.N., *Theory of Crystal Dislocations*, (Oxford University Press, Oxford, 1967)
- Nye, J.F., "Some Geometrical Relations in Dislocated Crystals", *Acta Metallurgica*, **1**, 153, (1953)
- Nye, J.F., *Physical Properties of Crystals*, (Clarendon Press, Oxford, 1957)
- Pertsev, N.A., Romanov, A.E., and Vladimirov, V.I., "Disclination-Dislocation Model for the Kink Bands in Polymers and Fibre Composites", *J. of Mat. Sci.* **16**, 2084, (1981)

- Pertsev, N.A. and Vladimirov, V.I., "Elastic Anisotropy and Kink Band Formation in Oriented Polymers", *J. of Mat. Sci. Letters* **1**, 153, (1982)
- Pertsev, N.A. and Romanov, A.E., "Instability of Front Profiles of Kink Bands in Oriented Polymers", *Mekhanika Kompozitnykh Materialov* **5**, 781, (1983)
- Pertsev, N.A., Marikhin, V.A., Myasnikova, L.P., and Pelzbauer, Z., "Incomplete Kink Bands in Fully Oriented High-Density Polyethylene", *Polym. Sci. U.S.S.R.* **27**(7), 1611, (1985)
- Prasad, P.N. and Williams, D.J., *Introduction to Nonlinear Optical Effects in Molecules and Polymers*, (John Wiley and Sons, New York, 1991)
- Read, R.T. and Young, R.J., "Extended-Chain Polydiacetylene Crystals", *J. of Mat. Sci.* **14**, 1968, (1979)
- Read, R.T. and Young, R.J., "The Deformation of Polydiacetylene Single Crystals", *Phil. Mag. A* **42**(5), 629, (1980)
- Read, R.T. and Young, R.J., "Direct Lattice Resolution in Polydiacetylene Single Crystals", *J. of Mat. Sci.* **16**, 2922, (1981)
- Read, R.T. and Young, R.J., "Radiation Damage and High Resolution Electron Microscopy of Polydiacetylene Crystals", *J. of Mat. Sci.* **19**, 327, (1984)
- Reneker, D.H. and Mazur, J., "Dispirations, Disclinations, Dislocations, and Chain Twist in Polyethylene Crystals", *Polymer* **24**, 1387, (1983)
- Reneker, D.H. and Mazur, J., "Small Defects in Crystalline Polyethylene", *Polymer* **29**, 3, (1988)
- Sangwal, K., *Etching of Crystals*, (North-Holland, Amsterdam, 1987)
- Sawyer, L.C. and Grubb, D.T., *Polymer Microscopy*, (Chapman and Hall, London, 1987)
- Schermann, W., Wegner, G., Williams, J., and Thomas, J., "The Role of Dislocations in the Solid-State Polymerization of Monomers Having Conjugated Triple Bonds: A Study of 2,4-Hexadiyne-1,6-diol Bis(p-toluene sulfonate)", *J. Polym. Sci.* **13**, 753 (1975)
- Shadrake, L.G. and Guiu, F., "Dislocations in Polyethylene Crystals: Line Energies and Deformation Modes", *Phil. Mag.*, **34**(4), 565, (1976)
- Shin, K. and King, A.H., "Observation of Grain Boundary Structure in Zinc", *Phil. Mag. A* **63**(5), 1023, (1991)

- Schultz, J., *Polymer Materials Science*, (Prentice-Hall, Inc., Englewood Cliffs, New Jersey, 1974)
- Singh, A. and King, A.H., "Tables of Coincidence Orientations for Ordered tetragonal  $L1_0$  Alloys for a Range of Axial Ratios", *Acta Cryst.* **B49**, 266, (1993)
- Sinko, P. and Kohn, J., "Polymeric Drug Delivery Systems. An Overview", in M.A. El-Nokaly, D.M. Piatt, and B.A. Charpentier, Eds., *Polymeric Delivery Systems. Properties and Applications.*, (American Chemical Society, Washington, D.C., 1993)
- Smith, D.A., "Experimental Techniques for the Study of Grain Boundary Structure", *Canadian Metallurgical Quarterly* **13**(1), 65, (1974)
- Spence, J.C.H., O'Keefe, M.A., and Kolar, H., "High Resolution Image Interpretation in Crystalline Germanium", *Optik*, **49**(3), 307, (1977)
- Spence, J.C.H., *Experimental High-Resolution Electron Microscopy*, 2nd Ed., (Oxford University Press, New York, 1988)
- Srolovitz, D.J., Safran, S.A., and Tenne, R., "Morphology of Nested Fullerenes", Personal Communication, (1994)
- Srolovitz, D.J., Safran, S.A., and Tenne, R., "Elastic Equilibrium of Curved Thin Films", Personal Communication, (1994)
- Steeds, J.W., *Introduction to Anisotropic Elasticity Theory of Dislocations*, (Clarendon Press, Oxford, 1973)
- Sumpter, B.G., Noid, D.W., and Wunderlich, B., "Computer Simulation and Modeling of Polymeric Crystals", *Trends in Polymer Science* **1**(6), 160, (1993)
- Sutton, A.P., "Grain-boundary Structure", *International Metals Reviews* **29**(5), 377, (1984)
- Sutton, A.P. and Balluffi, R.W., "On Geometrical Criteria for Low Interfacial Energy", *Acta Metall.*, **35**(9), 2177, (1987)
- Tefft, J. and Friend, D.R., "Controlled Release Herbicide Formulations Based on Polymeric Microspheres", *J. Controlled Release* **27**(1), 27 (1993)
- Teodosiu, C., *Elastic Models of Crystal Defects*, (Springer-Verlag, New York, 1982)

- Tsai, K.H., Schwartzman, A.F., Gallego, R., Ortiz, M., O'Keefe, M.A., and Kim, K.S., "Determination of the Strain Field from an HREM Image of a Si Lomer Dislocation", *Proc. 50th Annual Meeting of the Electron Microscopy Society of America*, 144, (1992)
- Van Tomme, E., Van Daele, P.P., Bates, R.G., and Lagasse, P.E., "Integrated Optic Devices Based on Nonlinear Optical Polymers", *IEEE Journal of Quantum Electronics* 27(3), 778, (1991)
- Vinogradov, G.A., "The Mechanism and Kinetics of the Polymerization of Conjugated Diacetylenes. The Physical Properties of Polydiacetylenes", *Russian Chemical Reviews* 53(1), 77, (1984)
- Voigt-Martin, I.G., Garbella, R.W., and Schumacher, M., "Structure and Defects in Discotic Crystals and Liquid Crystals as Revealed by Electron Diffraction and High-Resolution Electron Microscopy", *Macromolecules*, 25, 961, (1992)
- Vladimirov, V.I., Zembil'gotov, A.G., and Pertsev, N.A., "Dislocation Theory of Kink Boundaries in Oriented Polymers", *Sov. Phys. Solid State* 31(5), 852, (1989)
- Weertman, J. and Weertman, J.R., *Elementary Dislocation Theory*, (Oxford University Press, New York, 1992)
- Wegner, G., *Z. Naturforsch.* 24b, 824, (1969)
- Weidner, D.J., Wang, Y., and Vaughan, M.T., "Strength of Diamond", *Science*, 266, 419, (1994)
- Wilson, P.M. and Martin, D.C., "Dislocation Mediated Lattice Bending in 1,6-di(N-carbazolyl)-2,4 hexadiyne (DCHD) polydiacetylene droplets", *J. Mater. Res.*, 7 (11), 3150, (1992)
- Wolf, D. and Yip, S., *Materials Interfaces*, (Chapman and Hall, London, 1992)
- Wolf, D., "Structure-Energy Correlation for Grain Boundaries in F.C.C. Metals-I. Boundaries on the (111) and (100) Planes", *Acta Metall.* 37(7), 1983, (1989)
- Wright, J.D., *Molecular Crystals*, (Cambridge University Press, Cambridge, 1987)
- Yamashita, T., Ponce, F.A., Pirouz, P., and Sinclair, R., "High-Resolution Lattice Imaging of Cadmium Telluride", *Phil. Mag. A*, 45(4), 693, (1982)



- Yee, K.C. and Chance, R.R., "Synthesis and Properties of a New Polydiacetylene: poly[1,6-di(N-carbazolyl)-2,4-hexadiyne]", *J. Polym. Sci. Polym. Phys. Ed.* **16**, 431, (1978)
- Yeung, P.H. and Young, R.J., "Direct Imaging of Molecules in Polydiacetylene Single Crystals", *Polymer* **27**, 202, (1986)
- Young, R.J., Reed, R.T., Bloor, D., and Ando, D., "Structure and Morphology of Polydiacetylene Single Crystals", *Discuss. Faraday Soc.* **68**, 509 (1979)
- Young, R.J. and Petermann, J., "Structure and Mechanical Properties of Polydiacetylene Single Crystals", *Makromol. Chem.* **182**, 621, (1981)
- Young, R.J. and Petermann, J., "Defects in Polydiacetylene Single Crystals. II. Dislocations in pTS", *J. of Polym. Sci. Polym. Phys. Ed.* **20**, 961, (1982)
- Young, R.J., "Mechanical and Structural Properties of Polydiacetylenes", in D. Bloor and R.R. Chance, Eds. *Polydiacetylenes, Synthesis, Structure and Electronic Properties*, Martinus Nijhoff Publishers, Dordrecht, (1985)